OUKA
The University of Osaka
Institutional Knowledge Archive

Title	Numerical Modelling for Laser Welding Pool Thermal-Dynamics and Material Mixing of Cast-Iron, Carbon-steel and Ni-Alloy
Author(s)	Zhang, Renzhi
Citation	大阪大学, 2026, 博士論文
Version Type	VoR
URL	https://doi.org/10.18910/105485
rights	
Note	

The University of Osaka Institutional Knowledge Archive : OUKA

https://ir.library.osaka-u.ac.jp/

The University of Osaka

Doctoral Dissertation

Numerical Modelling for Laser Welding Pool Thermal-Dynamics and Material Mixing of Cast-Iron, Carbon-steel and Ni-Alloy

(鋳鉄・炭素鋼・Ni 合金のレーザ溶接溶融池における熱流体と材料混合の数値解析モデリング)

ZHANG RENZHI

December 2025

Division of Global Architecture,
Graduate School of Engineering
The University of Osaka

Table of Content

Table of Content i

List of Abbreviations and Symbols iv

List of Figures vi

List of Tables x

Chapter 1. Introduction 1

1.1. Research background and Motivation 1

1.1.1. Overview of laser welding 1

1.1.2. Current status of laser welding 2

1.2. Dissimilar material welding 3

1.2.1. Industrial application 5

1.2.2. Challenges and research trends 6

1.3. Numerical simulation in laser welding 9

1.4. Molten pool dynamics and joining performance 11

1.5. Purpose and objectives of this study 14

Chapter 2. Numerical Modelling of Laser Welding Pool Thermal-Dynamics and two Dissimilar Materials Mixing without Filler Wire 18

2.1. Introduction 18

2.2. Overview of the welding configuration 19

2.3. Numerical modelling 20

2.3.1. Geometry and meshing 20

2.3.2. Governing equations 21

2.3.3. Laser heat source model 23

2.3.4. Recoil pressure model 24

2.3.5. Surface tension model 24

2.3.6. Volume of fluid model 25

2.3.7. Initial conditions 25

2.3.8. Temperature-dependent material properties 26

2.4. Results and discussions 28
2.4.1. Molten shape and validation with experiment 28
2.4.2. Temperature distribution 29
2.4.3. Dynamic keyhole behaviors 31
2.4.4. Velocity field in molten pool 36
2.4.5. Materials volume fraction 41
2.5. Summary 47
Chapter 3. Numerical Modelling of Laser Welding Pool Thermal-Dynamics and three Dissimilar Material Mixing with Nickel Alloy Filler Wire 49
3.1. Introduction 49
3.2. Welding configuration with filler wire 50
3.3. Numerical modeling 53
3.3.1. Molten droplets model 53
3.3.2. Initial conditions 54
3.3.3. Temperature-dependent material properties 55
3.4. Results and discussions 56
3.4.1. Molten shape and validation with experiment 56
3.4.2. Temperature distribution and validation with experiment 57
3.4.3. Dynamic keyhole behaviors 59
3.4.4. Molten droplet transfer and mixing behavior 62
3.4.5. Velocity field in molten pool 65
3.4.6. Materials volume fraction 66
3.5. Summary 69
Chapter 4. Finite Element Modelling for Asymmetric Molten Shape in Laser Welding Dissimilar Materials 71
4.1. Introduction 71
4.2. Materials and offset positions of filler wire 71
4.3. Efficient numerical modeling 72
4.3.1. Geometry and meshing 72

4.3.2. Equivalent laser heat source model 73
4.3.3. Modelling for thermal boundaries 73
4.4. Results and discussions 80
4.4.1. Temperature history and validation with experiment 80
4.4.2. Temperature distribution of molten zone and heat affected zone 81
4.4.3. Molten zone shape and its size 86
4.4.4. Influence of welding wire position on molten shape 90
4.5. Summary 94
Chapter 5. Conclusions 95
References 98
Achievements 115
Publications related to doctor thesis 115
Other publications 116
Acknowledgements 117

List of Abbreviations and Symbols

Nd:YAG: Neodymium-doped Yttrium Aluminum Garnet

EV: Electric Vehicle

CFD: Computational Fluid Dynamics

FEM: Finite Element Method

AI: Artificial Intelligence

HAZ: Heat Affected Zone

VOF: Volume of Fluid

MIG: Metal Inert Gas

CSF: Continuum Surface Force

ρ: Fluid density

$\vec{u}$: Mean velocity vector

t: Elapsed time

S_m: Source term of mass

∇: Nabla operator

P: Pressure

μ: Dynamic viscosity

g: Gravitational acceleration

Fs: Source term of volume forces

h: Enthalpy

T: Local temperature

T_S: Solidus temperature

T_L: Liquidus temperature

T_v: Evaporation temperature

k: Thermal conductivity

S_q: Source term of heat

c_p: Specific heat

L_m: Latent heat of melting

f_L: Liquid fraction

v_0: Welding velocity

H: Depth of heat source

Q: Laser power input

η: Laser absorption efficiency

R_0: Heat source radius at upper surface

P_r: Recoil pressure

P_0: Reference pressure

C: Material-dependent coefficient

τ: Shear stress

γ: Surface tension

$\nabla_S T$: Surface gradient of temperature

F: Volume fraction

r_d: Molten droplet radius

D_n: The number of dripping droplets in a second

DC: Droplets dripping threshold

q_c: Power density distributions of cylinder heat source

q_f: Power density distributions of front ellipsoids in Goldak heat source

q_r Power density distributions of rear ellipsoids in Goldak heat source

a_f: Length of the front ellipsoid

a_r: Length of the rear ellipsoid

b: Maximum width of the total ellipsoid

F_f: Heat fraction at front ellipsoid

F_r: Heat fraction at rear ellipsoid

e: Wire offset position

es: Heat source offset position

List of Figures

Fig. 2.1. Instruction schematic of welding process and geometry model built. 20
Fig. 2.2. Meshing of calculation model. 21
Fig. 2.3. The equivalent heat source model. 23
Fig. 2.4. Initial configuration of the base metal domain. 25
Fig. 2.5. Schematic of the heat source configuration. 26
Fig. 2.6. Temperature-dependent thermophysical properties of carbon steel, cast-iron, and nickel-alloy (a) Density, (b) Dynamic viscosity. 27
Fig. 2.7. Molten zone morphology comparison between experiment and simulation result (a) Experimental result, (b) Simulated result. 28
Fig. 2.8. Comparison of experimental and simulated curves on surface heat dissipation (a) Temperature field map in experiment, (b) Temperature field map in simulation, (c) Comparation of cooling temperature curve. 31
Fig. 2.9. Transient evolution of keyhole dynamics and molten pool flow of middle-section (a-1) to (f-1) Longitudinal section view, (a-2) to (f-2) Top view. 34
Fig. 2.10. Transient keyhole dynamics and its surface flow pattern. 35
Fig. 2.11. Velocity distribution on transverse cross-section of molten pool 37
Fig. 2.12. Velocity distribution on transverse cross-section at keyhole location 39
Fig. 2.13. Velocity distribution on the longitudinal cross-section. 41
Fig. 2.14. Cross-sectional distribution of steel and cast iron at the keyhole location at various welding times. 43
Fig. 2.15. Cross-sectional distribution of steel and cast iron at the keyhole location at different locations after solidification. 45
Fig. 2.16. Three-dimensional visualization of dissimilar-metal mixing along the welding interface. 47

Fig. 3. 1. Cross-sectional macrostructures of dissimilar welding between carbon steel and cast-iron (a) No filler wire, (b) With nickel-alloy filler wire. 49
Fig. 3.2. Actual welding experiment procession (a) Wire position at groove center, (b)Wire position at carbon steel. 52
Fig. 3.3. The instruction schematic of welding procession. 52
Fig. 3.4. Illustration of welding wire feeding (a) Wire feeding in the experiment, (b) Molten droplet dripping model in the simulation. 54
Fig. 3.5. Initial configuration of the base metal domain. 54
Fig. 3.6. Schematic of the initial heat source configuration (a) The heat source acted inside the metal (b), Heat source acted on the metal surface. 55
Fig. 3.7. Temperature-dependent thermophysical properties of carbon steel, cast-iron, and nickel-alloy (a) Density, (b) Dynamic viscosity. 56
Fig. 3.8. Comparison of molten zone morphology between experiment and simulation (a) Experimental result, (b) Simulated result. 57
Fig. 3.9. Experimental and simulated curves comparing surface heat dissipation (a) Temperature field map in experiment, (b) Temperature field map in simulation, (c) Comparation of cooling temperature curve 58
Fig. 3.10. Transient evolution of keyhole dynamics and molten pool flow (a-1) to (f-1) Longitudinal section view, (a-2) to (f-2) Top view. 61
Fig. 3.11. The first molten droplet transfer progress in groove (a-1) to (e-1) Transverse section view, (a-2) to (e-2) Longitudinal section view. 63
Fig. 3.12. Transient process of molten droplet transfer and material mixing. 64
Fig. 3.13. Velocity distribution at keyhole position at transverse cross-section. 66
Fig. 3.14. Evolution of keyhole shape and material distribution at the laser position. 67
Fig. 3.15. Longitudinal distribution of the nickel-alloy at different concentration levels from 5%~100%. 68
Fig. 3.16. Similar distribution of nickel-alloy at different transverse cross sections. . 69

Fig. 4.1. Experiment setup and local geometry of welding groove (a) experiment setup arrangement, (b) cross-section view of laser and wire position. 72
Fig. 4.2. Geometry and meshing of calculation model. 73
Fig. 4.3. The equivalent heat source model (a) Cylinder heat source model, (b) Goldak heat source model. 75
Fig. 4.4. The description of eccentric heat source composition (a) Wire position with no deviation ($es = 0mm$), (b) Wire position deviates to carbon steel ($es = 0.2mm$), (c) Wire position deviates to cast-iron ($es = -0.2mm$). 77
Fig. 4.5. Material properties of three materials (a) Specific heats of three materials, (b) Density of three materials, (c) Thermal conductivity of three materials..... 79
Fig. 4.6. Convection heat transfer coefficient at different surfaces. 79
Fig. 4.7. Experimental and simulated curves comparing surface heat dissipation (a) Comparation of temperature field map, (b) Comparing temperature curves..... 81
Fig. 4.8. Macroscopic overview of temperature distribution. 82
Fig. 4.9. Temperature history curve of molten zone (a) Instruction of evaluation point position, (b) Temperature history curve of molten zone center, (c) Temperature history curve of iron side heat affected zone. 84
Fig. 4.10. Experimental and simulated comparison graph of molten zone shapes (a) Wire position deviates to cast-iron, (b) Wire position in the middle position (seam), (c) Wire position deviates to carbon steel. 85
Fig. 4.11. Temperature field of heat affected zone and molten zone (a) Welding wire on steel side, (b) Welding wire on the iron side. 86
Fig. 4.12. Instructions for cross-sectional measurement position (a) Molten zone dimensions of experimental result, (b) Position instruction of simulation result. 87
Fig. 4.13. Comparation of welding zone width size (a) Section 1, (b)Section 2, (c) Section 3, (d) Welding zone width difference of section 1 and section 2..... 89
Fig. 4.14. Comparison of temperature distribution for different positions of welding wire. 91

Fig. 4.15. Comparison of the width for the molten zone (a) The width of each part of welding zone W1,2 and WH1,2 of section 1, (b) The width of each part of welding zone W1,2 and WH1,2 of section 2.....92
Fig. 4.16. Fusion line boundary of molten zone. 93
Fig. 4.17. Experimental and simulated comparison curves of the distance from the model's pivot center to the iron side welding line.....93

List of Tables

Table 2.1. Equivalent heat source parameters 24
Table 2.2. Temperature dependent material properties for each material 27

Table 3.1. Chemical composition of Chrome-Manganese steel, FCD600 equivalent and MG82 51
Table 3.2. Temperature dependent material properties for base metals and filler wire 56

Chapter 1. Introduction

1.1. Research background and Motivation

1.1.1. Overview of laser welding

Laser welding has evolved into one of the most advanced and versatile technologies in modern manufacturing. It employs a highly concentrated, coherent laser beam to locally melt and fuse materials, providing precise energy control and minimal thermal distortion. Owing to its unique characteristics, such as high energy density, deep penetration, and small heat-affected zones, laser welding enables the production of joints with excellent dimensional accuracy and mechanical performance. The ability to deliver heat in a controlled and localized manner makes it particularly suitable for joining thin sheets, complex geometries, and thermally sensitive materials.

The origin of laser welding can be traced back to 1960, when Theodore Harold Maiman[1] successfully demonstrated the first ruby laser. This achievement marked the beginning of the practical application of laser technology. Initially, lasers were primarily used in scientific and medical fields; however, the discovery of their ability to generate a concentrated and coherent energy beam soon attracted attention from manufacturing engineers. Early investigations explored the feasibility of using lasers for cutting and welding, revealing their potential as a clean and non-contact joining method.

During the 1970s and 1980s, solid-state and CO_2 lasers[2] were introduced into industrial practice, allowing the first applications of laser welding in the electronics and tooling industries. These early systems, though limited in power and efficiency, established the foundation for precision material processing. As laser technology advanced, improvements in optical systems, focusing mechanisms, and power control led to significant increases in beam quality and energy efficiency. The introduction of Nd:YAG lasers[3]in the 1990s enabled flexible beam delivery through optical fibers,

further enhancing the adaptability of laser welding to complex industrial environments.

The development of high-power fiber and disk lasers in the 2000s represented a breakthrough. These new-generation laser sources offered higher energy efficiency, superior beam quality, and more stable performance compared with earlier systems. Consequently, laser welding transitioned from a laboratory-scale process to a widely adopted industrial technology. Its capability for automation, integration with robotic systems, and compatibility with advanced sensors has positioned laser welding as a cornerstone of modern intelligent manufacturing.

1.1.2. Current status of laser welding

At present, laser welding has matured into a key technology for high-quality and high-efficiency fabrication across various industries. Its evolution has been closely linked to the continuous advancement of laser sources and process control systems. Modern fiber lasers can deliver stable, high-power beams with exceptional precision and reliability, allowing for consistent performance even under demanding production conditions. Furthermore, the ability to modulate laser power and focus on real time has expanded its applicability to materials with widely differing thermal and optical properties.

In the automotive industry, laser welding is extensively employed in body assembly, transmission components, and powertrain systems, contributing to the production of lightweight and energy-efficient vehicles. Particularly in electric vehicle manufacturing, laser welding plays an essential role in the joining of battery modules and drive unit components, where high integrity and low distortion are required. In the aerospace sector, laser welding is applied to fabricate lightweight titanium and aluminum structures that demand superior mechanical strength and minimal residual stress[4]. In the electronics and medical device industries, micro-laser welding is utilized for precision bonding of miniaturized components with tight dimensional tolerances.

From a technological perspective, the current research and development trend in laser welding focuses on improving process stability, weld quality, and real-time monitoring. The integration of sensors, high-speed cameras, and machine learning algorithms allows for adaptive control of defect formation. Moreover, numerical modeling has become an indispensable tool for predicting temperature fields, fluid flow, and metallurgical transformations. These simulations provide valuable insights into the complex phenomena that are otherwise difficult to observe experimentally.

Another growing area of interest is dissimilar metal laser welding, driven by the need for lightweight, high-performance structures in automotive and aerospace applications. The ability of laser welding to concentrate energy within a small area makes it ideal for joining materials with different melting points and thermal conductivities. However, the differences in properties introduce challenges to laser welding processing. Addressing the challenges through advanced modeling, process optimization, and filler metal design has become a central topic in current research.

1.2. Dissimilar material welding

Dissimilar material welding has become increasingly important in recent years as industries seek to combine materials with different mechanical, thermal, and chemical properties to achieve lightweight, cost-efficient, and high-performance components. This approach allows engineers to utilize the advantages of each material while minimizing overall manufacturing costs. For instance, high-strength steels may be combined with lightweight aluminum alloys, corrosion-resistant stainless steels, or heat-resistant nickel alloys to meet specific functional requirements within a single structure.

The demand for reliable dissimilar material joining has grown rapidly in various sectors such as automotive, aerospace, shipbuilding, energy, electronics and medical industries[5]. In these industries, the integration of multiple materials enables enhanced performance under complex loading and environmental conditions[6–10]. However, joining dissimilar metals remains a significant challenge due to the large differences in their thermophysical and metallurgical properties. Variations in melting

point, thermal conductivity, and coefficient of thermal expansion can lead to uneven heat distribution, residual stress, and distortion during welding. Furthermore, chemical incompatibility between base materials often causes the formation of brittle intermetallic compounds at the interface, reducing joint strength and reliability.

A range of welding and joining techniques have been developed to address these challenges, including friction stir welding, diffusion bonding, brazing, and arc-based hybrid methods[11–15]. Among them, laser welding has emerged as one of the most promising processes for dissimilar metal joining due to its high energy density, localized heating, and excellent controllability[16–18]. The concentrated heat input minimizes the size of the heat-affected zone and reduces the thermal stress between dissimilar materials. Moreover, the non-contact nature of the laser process allows for accurate energy delivery and easy integration with robotic systems, making it suitable for high-volume and precision manufacturing[19].

In recent years, continuous improvements in laser power[20], beam quality, and process monitoring[21] have significantly enhanced the feasibility of dissimilar material laser welding[22]. Advanced hybrid welding methods that combine lasers with auxiliary heat sources—such as arc[23] or plasma—are also being developed to improve gap tolerance and joint stability. At the same time, the use of appropriate filler materials, optimization on the groove[24] and substrate shape[25,26] have proven effective in reducing metallurgical incompatibility and improving weldability respectively. The growing interest in computational modeling[27] and in-situ-diagnostics further supports the understanding of thermal and metallurgical behaviors in dissimilar metal welding. The experiment method also provided the joining mechanism in microscope vision. For example, Li. Et al[28,29] investigated the influence on tensile stress by joint shape and the interfacial bonding mechanism in Al/Ti dissimilar friction stir welding, indicating that the Z shape joint interface can increase 19% tensile strength.

Overall, dissimilar material welding represents a crucial technology for next generation manufacturing, enabling the production of complex multi-material

systems that balance weight, strength, and durability. Its continued advancement, particularly through laser-based approaches, will play a vital role in supporting the evolution of lightweight structures, energy-efficient systems, and sustainable industrial production.

1.2.1. Industrial application

The application of dissimilar material welding has expanded rapidly across multiple industrial[30,31] sectors as modern engineering increasingly pursues lightweight, high strength, and multifunctional structures. By combining materials with complementary properties—such as the high strength of steels[32,33], the low density of aluminum[34–36], and the excellent corrosion resistance of nickel or titanium alloys—manufacturers can achieve superior performance and resource efficiency[37–40]. This trend aligns with global efforts toward sustainable development and the reduction of energy consumption in transportation and manufacturing systems.

In the aerospace industry, dissimilar material joining is essential for integrating lightweight alloys and heat-resistant materials[41]. Laser and hybrid welding techniques are widely applied to join titanium[42,43] to nickel-based superalloys or stainless steels for turbine components[44], ensuring both mechanical integrity and reduced structural weight. Similarly, in the energy sector, dissimilar joints[45] are required in pressure vessels, heat exchangers, and pipelines[46,47], where components operate under extreme temperature and corrosion conditions. The ability to weld dissimilar materials extends the service life and reliability of such systems while minimizing material costs.

However, among all applications, the automotive industry has become the most active field for dissimilar metal welding due to its continuous drive toward vehicle lightweighting and energy efficiency[48–50]. Modern automotive structures increasingly integrate high-strength steels, aluminum alloys, and cast-irons to reduce weight without compromising crash safety or rigidity. Laser welding is favored for

these applications because of its concentrated heat input, high processing speed, and compatibility with robotic automation. It allows precise joining of materials with different melting temperatures and thermal conductivities, such as aluminum-to-steel, steel-to-cast-iron, aluminum-to-copper and magnesium to steel combinations[51–53].

Furthermore, laser welding plays a critical role in the production of electric vehicles (EVs), where it is used extensively in the assembly of battery enclosures[54–56], motor case, and transmission components. These joints often require dissimilar materials to balance electrical conductivity, mechanical strength, and thermal management. The high precision and repeatability of laser processes enable reliable production of such complex assemblies.

The increasing adoption of dissimilar material welding in automotive manufacturing demonstrates its potential to enhance both structural performance and production efficiency. As vehicle designs continue to evolve toward multi-material architectures, the ability to predict and control molten pool behavior, element mixing, and residual stress distribution in dissimilar welds will be crucial for ensuring durability, cost-effectiveness, and sustainability in future manufacturing systems.

1.2.2. Challenges and research trends

Although welding technologies have evolved significantly over the past decades, the process still faces fundamental challenges that limit further improvements in reliability, productivity, and adaptability[57–59]. In general, welding involves multiple coupled physical phenomena, including heat transfer, fluid flow, phase transformation, and mechanical stress evolution, all occurring within very short time and spatial scales. The transient nature of these interactions makes it difficult to achieve complete control or to predict the resulting microstructure and mechanical performance accurately. Even under identical process conditions, variations in laser power, beam focus, or shielding gas flow can lead to differences in weld morphology and defect formation[60–62].

A persistent issue across the welding field is the control of process stability and defect prevention. Keyhole instability, porosity, spatter, and solidification cracking are typical problems that reduce weld quality[63]. These defects are strongly affected by process parameters and the dynamic behavior of the molten pool, which in turn are influenced by laser–material interaction, vaporization, and surface tension gradients. Achieving stable and reproducible welding outcomes therefore requires precise energy control and continuous process monitoring—tasks that remain technically challenging, especially for high-speed and high-power operations[64,65].

Another broad challenge lies in the integration of welding processes into intelligent and flexible manufacturing environments. As industries shift toward digitalized production and smart factories, traditional welding systems must evolve from manually tuned operations to adaptive, data-driven processes[66]. This transition demands high-fidelity sensing, predictive modeling, and closed-loop control[67–70]. Although significant progress has been made in laser process monitoring and automation, most existing systems still rely heavily on operator experience or simplified empirical models, which cannot capture the complex multi-physics nature of welding phenomena.

From a research perspective, the accurate numerical modeling of welding processes remains one of the most important but difficult tasks. The strong coupling between heat transfer, fluid flow, vapor pressure, and solidification makes it challenging to construct computational models that are both physically realistic and computationally efficient[71,72]. Moreover, boundary conditions such as surface deformation, phase change, and heat losses are difficult to measure and define accurately in experiments[73,74], further complicating model validation. While computational fluid dynamics (CFD) and finite element method (FEM) have significantly improved understanding of welding mechanisms, the simplifications commonly used to ensure convergence can limit their predictive accuracy.

Building upon these general challenges, dissimilar material welding introduces an additional layer of complexity. When two or more materials with different

thermophysical and metallurgical properties are joined, large mismatches in melting point, thermal conductivity, and thermal expansion coefficient often lead to asymmetric molten pool formation[75], residual stress, and distortion[76]. The unequal distribution of heat and mass transfer can cause incomplete fusion or excessive dilution, resulting in weak bonding regions. Furthermore, at the metallurgical level, dissimilar materials tend to form brittle intermetallic compounds or segregation zones at the fusion interface, which significantly reduce joint strength and ductility[77].

The chemical and mechanical incompatibilities in dissimilar welding make filler material design and process optimization particularly critical. The addition of appropriate filler metals—such as nickel- or copper-based alloys—can improve wettability, act as a diffusion barrier, and form ductile transition layers that mitigate the mismatch between the base materials. Hybrid laser–arc welding processes have also been explored to enhance gap-bridging capability and improve the stability of the molten pool to avoid the large residual stresses[78]. Nevertheless, predicting the interaction among the laser beam, filler droplets[79], and base materials remain a major research challenge due to the transient and non-linear nature of the process.

To address these challenges, recent research trends emphasize multi-physics modeling, in-situ diagnostics, and intelligent process control. High-fidelity numerical simulations based on CFD and phase-field methods provide deeper insight into heat transfer, molten pool dynamics, and element diffusion, enabling virtual experimentation and parameter optimization[80,81]. At the same time, advances in high-speed imaging, X-ray tomography, and spectroscopic diagnostics have made it possible to observe keyhole and molten pool behavior directly during welding, greatly improving model calibration and validation.

Emerging approaches are now combining data-driven methods with physics-based modeling. Machine learning and artificial intelligence (AI) techniques are being applied to analyze large experimental and simulation datasets, predict defect formation, and adaptively control process parameters in real time[82–84]. The

integration of these intelligent systems with digital twins and automation platforms is expected to transform laser welding into a self-optimizing and highly reliable manufacturing process.

1.3. Numerical simulation in laser welding

The complex nature of laser welding, involving simultaneous heat transfer, fluid flow, phase transformation, and mechanical interaction, has made experimental characterization alone insufficient to fully understand the underlying physical phenomena. To complement experimental studies, numerical simulation has become an indispensable tool for analyzing and optimizing welding processes[85–88]. The development of computational models over the past few decades has provided valuable insights into the temperature field[89–91], molten pool behavior, residual stress, and defect formation, enabling the design of more efficient and reliable welding systems[92].

The earliest numerical approaches to welding simulation focused primarily on thermal analysis. In the 1970s and 1980s[93], finite element methods were employed to calculate transient temperature distributions in the weld and surrounding base material[94,95]. These models typically assumed a stationary or moving heat source applied on the surface or within the material, allowing prediction of temperature gradients and cooling rates[96,97]. Early thermal simulations contributed significantly to understanding weld penetration, heat-affected zone (HAZ) dimensions, and solidification behavior. However, they generally treated the molten region as a static domain without considering fluid motion, limiting their ability to reproduce realistic molten pool geometries.

Building upon these early efforts, researchers soon recognized that temperature distribution alone could not fully describe weld morphology or defect formation. This realization led to the inclusion of mechanical and metallurgical modeling in welding simulations. Coupled thermo-elastic–plastic analyses were developed to predict residual stress and deformation after solidification. For example, based on the existing Gaussian distribution heat source model, Chang et al. [98]. proposed and

optimized a heat source model specifically for laser resistance spot welding, aiming to accurately compute the temperature field and melt pool shape in laser resistance spot welding. The equivalent heat source model was also used in simulation to solve complicated laser moving trails. Liang et al. [99] replaced the oscillations of the laser with two sets of conical heat sources as the equivalent heat source to investigate the temperature distribution and residual stress. Such models provide insight into distortion control and cracking behavior, which are critical for maintaining dimensional accuracy and structural integrity. Concurrently, phase transformation and microstructure evolution models were incorporated to link thermal histories with material properties, allowing prediction of hardness and strength distributions across the weld.

While thermal and stress analyses established the foundation of computational welding mechanics, they were not sufficient to capture the dynamic behavior of the molten pool— a key determinant of weld quality. The next major advancement came with the adoption of CFD to simulate heat and mass transfer within the molten metal. The pioneering work by DebRoy[100,101] and co-workers in the 1990s introduced CFD to welding research, demonstrating that convective heat transfer driven by Marangoni forces plays a dominant role in determining welding pool shape and size. Their models solved the governing equations of mass, momentum, and energy conservation, incorporating buoyancy, surface tension, and electromagnetic forces as driving factors. These studies revolutionized the understanding of molten pool behavior and laid the groundwork for the mechanistic interpretation of welding phenomena.

Subsequent developments in CFD modeling enabled the study of multi-phase and free-surface dynamics associated with keyhole formation, vaporization, and droplet transfer. The Volume of Fluid (VOF) method, originally developed for tracking immiscible fluid interfaces, was introduced into welding simulations to describe the evolution of the weld pool surface and keyhole geometry. By treating the molten metal, vapor, and surrounding gas as separate phases, the VOF method can capture

surface deformation, keyhole oscillation, and collapse—phenomena that are otherwise difficult to observe experimentally[102,103]. The CFD and VOF techniques have made it possible to model not only the shape of the molten pool but also the transient flow patterns, such as recirculating vortices, surface waves, and bubble motion.

The development of heat source models has also played a central role in improving the accuracy of welding simulations. Early analytical models, such as the Rosenthal[104] and double-ellipsoid (Goldak) heat sources, were used to represent energy input in arc and laser welding. These models provided simple yet effective ways to approximate heat flux distribution and were widely implemented in finite element thermal analyses. However, as simulation accuracy requirements increased, more physically realistic heat source descriptions were developed. In laser welding, Gaussian, conical, and combined volumetric heat source models have been introduced to represent the spatial and temporal variation of laser energy absorption. These improvements allow for more accurate prediction of temperature gradients, penetration depth, and molten pool morphology under different process conditions.

In parallel, significant progress has been made in modeling vaporization, recoil pressure, and surface tension effects—critical factors that govern keyhole stability. The inclusion of these phenomena has enabled researchers to reproduce keyhole oscillations, spatter formation, and pore entrapment observed in high-speed imaging experiments. Moreover, coupling between thermal, fluid, and phase-change phenomena has become more robust using advanced numerical techniques and increased computational power. High-resolution 3D transient simulations are now capable of predicting complex behaviors such as keyhole collapse, bubble motion, and metal vapor flow, providing deeper insight into defect mechanisms.

1.4. Molten pool dynamics and joining performance

The molten pool constitutes the central region of physical transformation during laser welding, where heat transfer, fluid flow, vaporization, and solidification occur simultaneously within a highly confined space. The morphology and evolution of the

molten pool directly determine weld geometry, microstructural development, and ultimately the mechanical performance of the joint. Therefore, understanding molten pool dynamics is fundamental for achieving stable, defect-free laser welds and provides a critical link between welding physics and joint quality.

Due to the highly concentrated energy input of the laser beam, the molten pool exhibits strongly transient behavior. Once melting initiates, fluid flow inside the pool is driven by multiple competing forces, including recoil pressure generated by metal vaporization, buoyancy induced by temperature-dependent density variation, and surface-tension gradients known as the Marangoni effect. Recoil pressure plays a dominant role in keyhole-mode laser welding, driving molten metal downward and enabling deep penetration. Meanwhile, Marangoni convection redistributes heat and molten material along the pool surface, influencing both pool shape and mixing behavior. The balance among these driving forces governs the stability of the keyhole and the overall molten pool morphology.

The geometry of the molten pool, characterized by its width, depth, and aspect ratio, is a key indicator of process stability. A stable molten pool typically results in uniform penetration and smooth weld beads, whereas irregular or asymmetric pools may cause defects such as underfill, humping, incomplete fusion, or porosity. Asymmetric heat absorption or flow instability around the keyhole can lead to non-uniform solidification, increasing the susceptibility to crack formation and microstructural inhomogeneity. Consequently, molten pool dynamics exert a strong influence on the heat-affected zone, solidification microstructure, and residual stress distribution.

In dissimilar material welding, molten pool behavior becomes even more complex due to mismatches in thermophysical properties between the base metals. Differences in melting temperature, thermal conductivity, viscosity, and surface tension generate asymmetric temperature fields and flow patterns within the molten pool. Such asymmetry affects element transport and mixing, potentially leading to compositional gradients, segregation, or the formation of brittle phases. Therefore, controlling

molten pool flow is essential for achieving homogeneous mixing and stable metallurgical bonding in dissimilar joints.

Molten pool dynamics are also closely linked to keyhole behavior and defect formation. The keyhole serves as the primary channel for laser energy absorption but is inherently unstable due to fluctuations in vaporization pressure and molten metal support. Periodic keyhole oscillation or collapse may trap vapor and form porosity. These behaviors are strongly dependent on process parameters such as laser power, focal position, and welding speed. Understanding the interaction between molten pool flow and keyhole stability is therefore critical for predicting and suppressing welding defects. Given its central role, molten pool dynamics have become a focal point of laser welding research. Advances in high-speed diagnostics and CFD modeling have provided powerful tools for investigating these transient, multi-physics phenomena. A detailed understanding of molten pool behavior enables more accurate prediction of weld quality and supports the development of optimized and adaptive welding strategies for industrial applications.

Recent years the researchers did lots of efforts on the molten pool dynamics investigation. For instance, Lin, Wang, and Lu[105] developed a transient multiphase model to study keyhole dynamics and porosity formation, providing insights into the relationship between recoil pressure, surface tension, and keyhole stability. Similarly, Huang and Xu [106] simulated bubble evolution and entrapment during solidification, emphasizing the role of eddy flow. To enhance the reliability of such models, high-speed imaging and synchrotron-based diagnostics have been increasingly combined with CFD for validation[107]. These techniques make it possible to directly capture the evolution of the weld pool during welding, thereby providing valuable data for validating numerical simulations.

The growing demand for lightweight design in electric vehicles has further increased the importance of advanced joining technologies. Welding is now frequently employed to replace bolted connections, reducing component count and overall vehicle weight. The use of high-strength materials has also expanded research

on dissimilar-metal joining, such as aluminum–copper and magnesium–steel combinations[108]. In numerical investigations, Huang and Wang[109] examined how mismatches in thermal properties between base metals lead to asymmetric molten pools and uneven mixing. Similarly, Ai and Dong[110] constructed a three-dimensional multiphase flow model to analyze asymmetry between Q235 low-carbon steel and 316L stainless steel under keyhole laser welding, that demonstrated keyhole-induced molten pool dynamics enlarge the molten pool. M. Shehryar Khan et al.[111] investigated the effects of full focusing and defocusing of the laser beam on keyhole behavior and molten pool morphology. Wu, Ishida et al.[112] developed a paraxial hybrid plasma–MIG welding process for medium-thick high-strength steel plates with a butting gap. Their study showed that molten pool flow promoted downward Ni transport, leading to an inhomogeneous distribution with higher Ni concentration at the pool bottom.

1.5. Purpose and objectives of this study

Laser welding enables high precision joining with minimal thermal distortion and is increasingly used for dissimilar materials. However, thermophysical differential between metals can cause asymmetric molten pools, unstable keyholes, and uneven mixing. To clarify these phenomena, experimental observation and a three-dimensional CFD simulation were conducted to study laser welding of carbon steel and cast-iron with a nickel-based filler wire. The model incorporated temperature-dependent properties, surface tension, recoil pressure, and droplet transfer to reproduce transient molten pool behavior. This work quantitatively elucidates heat transfer, fluid flow, and dissimilar metal interactions in molten pool. Based on this CFD results, a more efficient temperature-field model was developed, which enables quick and reliable prediction of molten pool shape for practical engineering applications. This study provides quantitative insight into molten-pool thermodynamics and element transport in dissimilar keyhole laser welding, offering guidance for optimizing filler position and process parameters in multi-material manufacturing.

Chapter 1 outlined the fundamentals and status of laser welding, with emphasis on its application to dissimilar materials and related challenges. The progress of numerical simulation in analyzing molten pool dynamics was reviewed, and the influence of thermal–fluid behavior on joint performance was discussed. Additionally, the research purpose and objectives on this dissimilar material laser welding were introduced. Furthermore, this chapter emphasized the significance of understanding the coupling mechanisms. The limitations of conventional approaches were identified, highlighting the need for improved modeling accuracy and experimental validation. Finally, the chapter established the overall framework of the present study, clarifying how the proposed methodology aims to bridge the gap between simulation prediction and real welding phenomena, thereby providing a scientific basis for optimizing process parameters and improving joint reliability.

Chapter 2 described the numerical model and computational methodology used in this study. The chapter outlined the geometric configuration, material properties, and governing equations applied in the CFD analysis. The boundary conditions, mesh design, and heat source model were introduced to reproduce the transient keyhole dynamics molten pool behavior and the material mixing in two dissimilar materials of the base metals. Finally, the model validation was presented by comparing simulated temperature distribution and molten pool shape with experimental results, confirming the reliability of the developed numerical approach.

Chapter 3 discussed the simulation and experimental results of three dissimilar materials laser welding between carbon steel and cast-iron using a nickel-based filler wire. The transient evolution of keyhole dynamics, molten pool flow, and temperature distribution were analyzed in detail. The effects of droplet transfer and Marangoni convection on element mixing and pool stability were clarified. Finally, the simulated results were compared with experimental observations to verify the model's accuracy and reveal the mechanisms governing dissimilar metal laser welding.

Chapter 4 presented the relationship between the wire feeding position and molten zone shape. Based on the CFD-based mechanism study, an efficient and accurate

temperature-field model was developed for practical engineering applications. A hybrid heat source model was established to analyze the molten zone morphology in dissimilar laser welding. The numerical results accurately reproduced the asymmetric molten pool shape observed in experiments and clarified the influence of wire feeding position on molten zone geometry. The model effectively predicted the temperature distribution and morphological variation caused by wire offset.

Chapter 5 summarized the main conclusions and presented the extended future research issues. Based on comprehensive numerical, the main findings were systematically discussed to clarify the fundamental mechanisms governing molten pool behavior and the influence of process parameters. In addition, this chapter outlined possible future research directions, such as improving the modeling accuracy of multiphase flow and surface tension effects, extending the methodology to other material systems, and integrating real-time sensing with numerical prediction for better process control.

Chapter 1.
Introduction

Chapter 2.
This chapter develops a numerical model to investigate thermal–fluid behavior and material mixing in laser welding between cast-iron and carbon-steel.
▪ Development of CFD model for cast-iron–carbon-steel welding
▪ Implementation of laser heat source, recoil pressure, and surface tension models
▪ Application of VOF method and temperature-dependent material properties
▪ Validation through comparison with experimental results

Chapter 3.
This chapter extends the previous model by incorporating filler wire addition (Ni-based alloy) to analyze three-material interactions.
▪ Extension of the model with Ni-based filler wire addition
▪ Establishment of molten droplet and material mixing models
▪ Analysis of temperature field, velocity distribution, and solidification

Chapter 4.
This chapter explores the effect of wire position and boundary conditions on molten pool asymmetry and process stability.
▪ Development of an efficient model for asymmetric molten zone prediction
▪ Construction of equivalent heat source and thermal boundary models
▪ Evaluation of wire position effect on molten pool morphology
▪ Validation through temperature history and cross-sectional comparison

Chapter 5.
This chapter summarizes the main conclusions and outlines directions for future research.
▪ Summary of modeling approaches and key findings
▪ Insights into molten pool dynamics and inter-material mixing mechanisms

Chapter 2. Numerical Modelling of Laser Welding Pool Thermal-Dynamics and two Dissimilar Materials Mixing without Filler Wire

2.1. Introduction

The mechanism of the thermal–fluid behavior and dissimilar-material mixing during keyhole laser welding is essential for improving the integrity and reliability of joints between carbon steel and cast-iron. In this study, a three-dimensional computational fluid dynamics model was developed to capture the transient evolution of the keyholes, the mix of two dissimilar base metals, coupled with traditional models of heat transfer, surface tension and recoil pressure. The model incorporates free surface deformation through a VOF based multiphase formulation to investigate the evaluation of transient keyholes morphology. The prediction of molten pool geometry and surface temperature histories show good agreement with experimental measurement results obtained from infrared thermal imaging, confirming the validity of the equivalent volumetric heat-source model. The numerical results reveal that the differences in thermal conductivity, viscosity, and surface-tension gradients between carbon steel and cast-iron lead to asymmetric keyhole stability and metal flow.in molten pool. The buoyancy induced flow, and the recoil pressure driven downward flow establish a persistent circulation structure, producing stronger mixing in the upper molten pool while maintaining a sharper interface at the lower region. Analysis of solidified cross-sections and 3D material distributions shows that the mixing zone remains thin and highly fluctuates near the keyhole but becomes spatially non-uniform along the welding direction due to transient keyhole oscillations and convection-driven mixing behavior. This study provides quantitative insight into the mechanisms governing dissimilar metal mixing in keyhole laser welding and offers a foundation for optimizing process stability and joint performance.

2.2. Overview of the welding configuration

A differential unit was designed for a kind of electric vehicle, in which the ring gear (carbon steel, Cr–Mn steel) and the differential case (cast-iron FCD600 equivalent) were joined. The detailed chemical compositions of the materials are listed in Table 1. The welding configuration adopted in this study followed a circular path with a radius of 56 mm., and the base metal height was 3.5 mm.

A YAG laser oscillator was employed as the heat source. The laser beam was directed perpendicularly onto the workpiece with an output power of 2510 W and a focal spot diameter of 0.4 mm. The focal point was positioned precisely at the bottom surface of the base metal. Laser welding was performed along the circular groove at a welding speed of 1.5 m/min.

The description above corresponds to the configuration without the use of filler wire and provides the baseline conditions for understanding the thermal–mechanical interactions at the joint.

Table 1 Chemical composition of Chrome-Manganese steel (carbon steel), FCD600 equivalent.

Chrome-Manganese steel		FCD600 equivalent	
C	0.27	C	3.7
Mn	1.27	Mn	0.51
Ni	0.07	Ni	-
Cr	1.27	Cr	-
Cu	0.12	Cu	0.56
Si	0.27	Si	2.36
S	0.03	S	~0.02
P	0.015	P	~0.05
Ti	<0.01	Sn	~0.05
Al	<0.03	Mo	-

2.3. Numerical modelling

2.3.1. Geometry and meshing

In this study, a three-dimension CFD model was developed using ANSYS Fluent to simulate the dissimilar metal laser welding process. The dissimilar material welding involved highly complex thermophysical phenomena, including heat conduction, convection, radiation, metal evaporation, and the influence of molten droplet transfer. To improve computational efficiency and ensure numerical convergence, certain simplifications were made by neglecting minor effects that have little impact on overall calculation. Accordingly, the following assumptions were made in the present model.

(1) The molten pool metal was assumed as a laminar, incompressible Newtonian fluid.

(2) All material properties in the simulation were assumed to be solely temperature-dependent, with no chemical reactions occurring among different materials.

(3) The reflection of the laser beam within the keyhole was neglected. All forms of energy input, such as thermal radiation and multiple reflections, were incorporated into the model through an equivalent heat source.

(4) The total welding length in the experiment was 351mm, while a 16mm segment in the stable welding region was selected as the computational domain for the simulation.

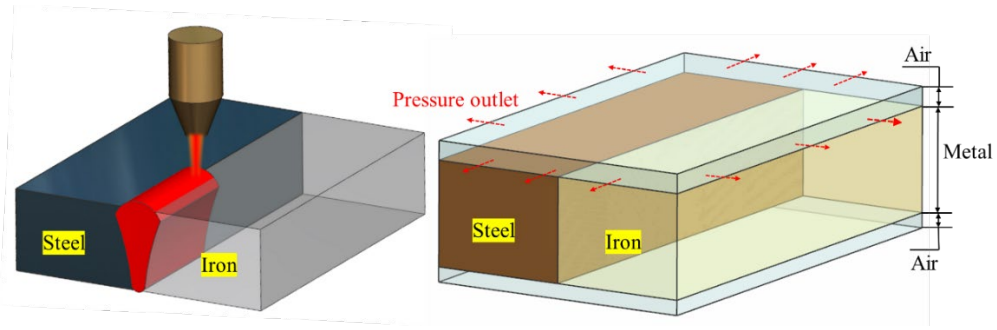


Fig. 2.1. Instruction schematic of welding process and geometry model built.

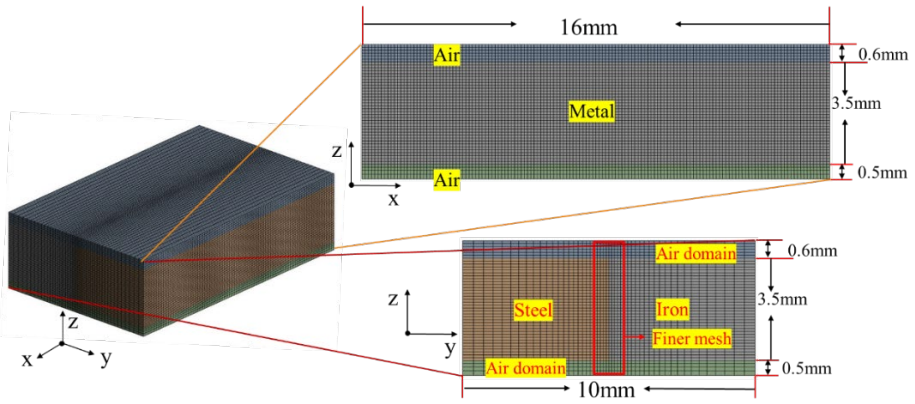


Fig. 2.2. Meshing of calculation model.

Based on the assumption, a three-dimensional geometry model was built. The computational domain was constructed with an overall dimension of 16 mm (length) × 10 mm (width) × 4.6 mm (height), as illustrated in Fig. 2.1. The domain consisted of two main regions: the metallic fluid domain and the surrounding air domain. The metallic region, representing the welding zone and dissimilar base metal material, had a vertical height of 3.5 mm. The air region was divided into two layers: a 0.6 mm-thick top layer and a 0.5 mm-thick bottom layer, located above and below the metallic region, respectively.

Fig. 2.2 introduced the meshing model of the simulation. The entire computational domain was discretized with hexahedral elements. The average mesh size was approximately 0.1 mm. To enhance resolution near the weld pool and along the wire feeding path, local mesh refinement was applied in these regions. Conversely, mesh coarsening was implemented in areas distant from the melting zone, particularly near the domain boundaries to improve efficiency without significantly compromising accuracy. The final mesh consisted of approximately 324,000 elements.

2.3.2. Governing equations

The calculation was governed by the conservation equations of mass, momentum, and energy. These equations collectively described the evolution of fluid flow and temperature field in the welding process.

Mass conservation equation:

$$\frac{\partial(\rho\vec{u})}{\partial t} + \nabla(\rho\vec{u}) = S_m \quad \text{Eq.2.1}$$

where ρ is the fluid density, u is the mean velocity in x, y, z direction, and S_m represents the source term, which is from the molten droplet material.

Momentum conservation equation:

$$\frac{\partial(\rho\vec{u})}{\partial t} + \rho(\vec{u}\cdot\nabla)\vec{u} = -\nabla P + \mu\cdot\nabla^2\vec{u}\cdot + \rho g + Fs \quad \text{Eq.2.2}$$

where P is the pressure, μ is the dynamic viscosity, and g is the gravitational acceleration. The source term Fs includes additional volume forces relevant to laser welding, contain recoil pressure at the keyhole wall and surface tension forces at the liquid–gas interface.

Energy conservation equation:

$$\frac{\partial(\rho h)}{\partial t} + \nabla(\rho\vec{u}h) = \nabla(k\nabla T) + S_q \quad \text{Eq.2.3}$$

where h is the enthalpy, T is the temperature, and k is the thermal conductivity. The source term S_q accounts for the laser heat input, molten droplet heat and latent heat associated with melting and solidification. To capture phase change, the enthalpy–porosity method is adopted:

$$h = \int c_p(T)dT + f_L\Delta L_m \quad \text{Eq.2.4}$$

where c_p is the specific heat, L_m is the latent heat of melting and f_L represents the liquid fraction, which governs the mushy zone resistance, allowing the proper transition between solid and liquid phases. f_L complied to be liner with temperature.

$$f_L = \begin{cases} 0; & T \le T_S \\ \frac{T-T_S}{T_L-T_S}; & T_S \le T \le T_L \\ 1; & T \ge T_L \end{cases} \quad \text{Eq.2.5}$$

where T is the present temperature, T_S and T_L is the solidus, liquidus temperature respectively.

2.3.3. Laser heat source model

In the present study, the heat input to the workpiece was assumed to originate solely from the laser energy. The laser beam was incident normal to the surface and directly irradiated the material, resulting in highly localized energy deposition within the welding zone. To accurately describe the spatial distribution of energy, a rotating Gaussian volumetric heat source model [113] was employed as shown in Fig. 2.3, the equation is given as follows:

$$q(x,y,z,t) = q_l \mathrm{e}^{-6\left[\frac{(x-v_0 t)^2+(y)^2}{r(z)^2}\right]} \quad \text{Eq.2.6}$$

$$q_l = \frac{9Q*\eta}{\pi {R_0}^2 H} \quad \text{Eq.2.7}$$

where v_0 is the welding velocity, t is the practical welding time, H is the depth of heat source, R_0 is the radius on the upper surface of the heat source, Q is the laser power input value and η is the laser absorption efficiency as shown in Table 2.1. Since the position of laser focal was at the bottom of the base metal, the laser spot diameter increased with the defocusing distance. Accordingly, the laser spot diameter distribution at depth direction can be expressed as:

$$r(z) = R_0\sqrt{ln\left(\frac{H}{z}\right)} \quad \text{Eq.2.8}$$

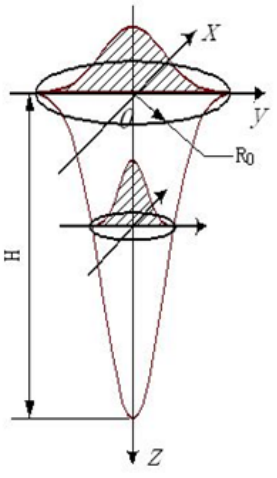


Fig. 2.3. The equivalent heat source model.

Table 2.1. Equivalent heat source parameters.

Property	Symbol	Value	Units
Laser input power	Q	2510	W
Weld velocity	v_0	25	mm/s
Welding time	t	-	s
Heat source depth	H	4.4	mm
Heat source radius at upper surface	R_0	0.6	mm
Laser absorption efficiency	η	0.95	-

2.3.4. Recoil pressure model

During laser keyhole welding, the evaporation of metal at the surface generates a recoil pressure that acts normal to the liquid–gas interface. In this study, the recoil pressure was expressed in an exponential form derived from the Clausius–Clapeyron[114] equation:

$$P_r = P_0 e^{(C\cdot\left(1-\frac{T_v}{T}\right))} \quad \text{Eq.2.9}$$

where P_r is the recoil pressure, P_0 is the reference pressure constant, C is a material-dependent coefficient related to the latent heat of vaporization and the gas constant, T_v is the evaporation temperature of the material, and T is the local surface temperature.

2.3.5. Surface tension model

Surface tension is the interfacial force acting between the deposited metal and the surrounding air, and it plays a significant role in driving molten metal flow[115]. In this study, the Continuum Surface Force (CSF) model [116] was applied to simulate fluid flow induced by surface tension variations with temperature. Under this

framework, the Marangoni force at the free surface can be described following the formulation proposed by Fan et al.[117].

$$\tau = \frac{d\gamma}{dT}\nabla_S T \qquad \text{Eq.2.10}$$

where τ represents the shear stress, γ is the temperature dependent surface tension, $\nabla_S T$ refer to the surface gradient of temperature.

2.3.6. Volume of fluid model

The free surface of the keyhole and molten wire droplets (if exist) were captured using Volume of fluid (VOF) method, which is expressed as follows:

$$\frac{\partial F}{\partial t} + F\nabla\vec{u} = 0 \qquad \text{Eq.2.11}$$

where F is the volume fraction, which is between 0 and 1.

2.3.7. Initial conditions

In the numerical setup, the initial regions of the metals and groove were defined through initialization. The width of the groove was 0.35mm and with a depth of 2.5mm. Blow this 2.5mm height, the two base metals were assumed to be in direct contact without a gap. The geometric instruction was as Fig. 2.4.

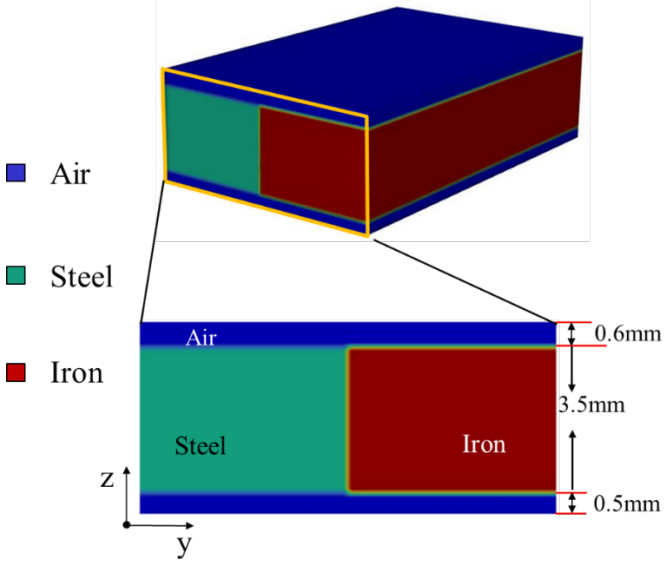


Fig. 2.4. Initial configuration of the base metal domain.

The initial temperature equals 300K, which is the same as environmental temperature. Because the groove width was smaller than the laser spot diameter, the incident laser energy was primarily distributed within the groove. In the model, the laser beam was therefore interacted only with outer surfaces of the base metals, the groove sidewalls and the base metal blow the groove. This allowed the equivalent Gaussian volumetric heat source to be applied only to the base metal, not the air if the keyhole formed, as illustrated in Fig. 2.5. The calculated welding time was 0.5s, which was 12.5mm in length. After the welding calculation, a 0.2s period naturally cooling procedure was also calculated.

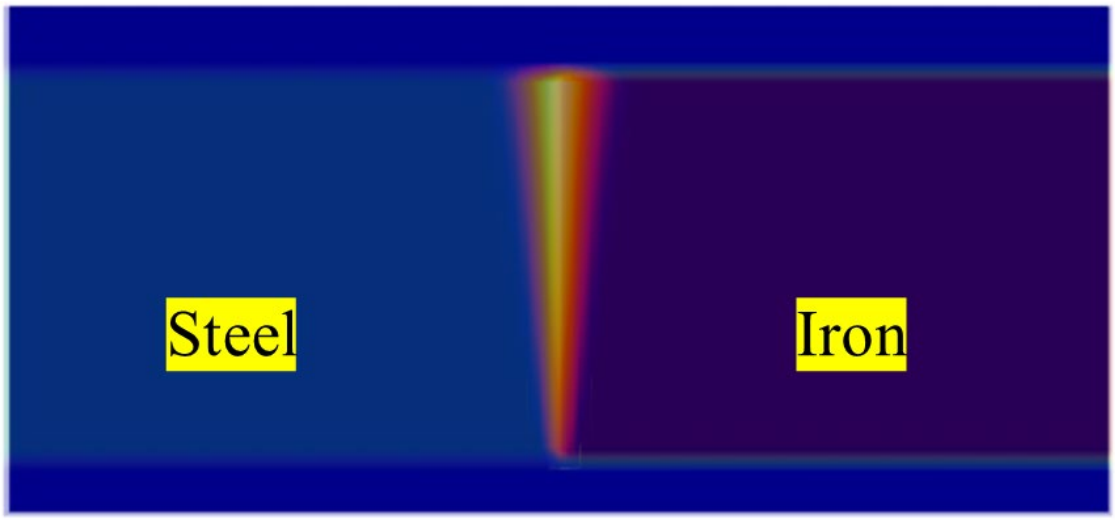


Fig. 2.5. Schematic of the heat source configuration.

2.3.8. Temperature-dependent material properties

To enhance the reliability of the numerical model, key thermophysical properties of the two metals, namely density, viscosity, and surface tension, were obtained through experimental measurements. These properties were characterized as functions of temperature within the range encountered during laser welding and directly incorporated into the CFD framework. Accurate representation of these parameters is critical for resolving melt flow behavior and surface deformation driven by Marangoni convection and recoil pressure. The experimentally measured

temperature-dependent density and viscosity curves are presented in Fig. 2.6(a) and (b). The results show an approximately linear decrease in density with increasing temperature, whereas viscosity decreases nonlinearly, indicating a significant increase in melting mobility at elevated temperatures. The remaining material properties adopted in the simulation are listed in Table 2.2

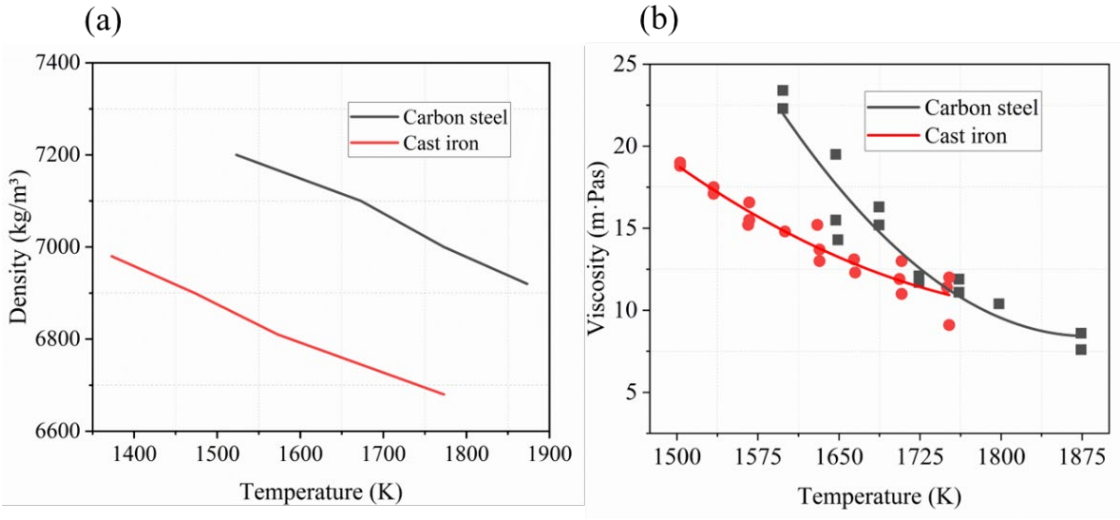


Fig. 2.6. Temperature-dependent thermophysical properties of carbon steel, cast-iron, and nickel-alloy (a) Density, (b) Dynamic viscosity.

Table 2.2. Temperature dependent material properties for each material

Property	Chrome-Manganese steel	FCD600 equivalent	Units
Specific heat	455~1100	500~950	$J \cdot kg^{-1} \cdot K^{-1}$
Thermal conductivity	30~40	18~45	$W \cdot m^{-1} \cdot K^{-1}$
Solidus temperature	1580	1434	K
Liquidus temperature	1623	1473	K
Latent heat of melting	272000	240000	$J \cdot kg^{-1}$
Surface tension	1.74~1.8	1.42~1.6	$N \cdot m^{-1}$

2.4. Results and discussions

2.4.1. Molten shape and validation with experiment

Fig. 2.7 presented a comparison between the experimentally observed cross-section and the numerically simulated molten pool profile. The experimental result showed a deeply, fully penetrated fusion zone and an asymmetric solidification boundary between the steel and cast-iron sides. The corresponding numerical result reproduced the overall pool shape, and the height and width of the molten pool are consistent with the experimental observation. The width of the upper surface of molten pool is 2.02mm, while the simulation result showed a 2.00mm width at upper surface, which indicated that the applied equivalent heat source accurately represented the laser energy distribution and absorption behavior during welding procession. This consistency demonstrated the applicability and reliability of the developed heat source model for predicting molten pool formation and thermal behavior in current study.

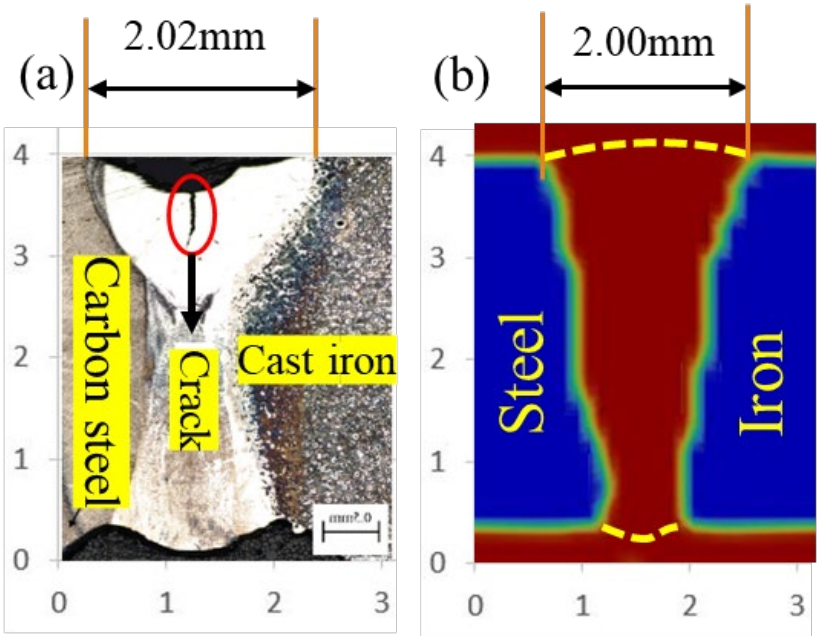


Fig. 2.7. Molten zone morphology comparison between experiment and simulation result (a) Experimental result, (b) Simulated result.

2.4.2. Temperature distribution

Fig. 2.8 shows the temperature evolution along the welding direction obtained from infrared thermal imaging and the numerical simulation result shown in Fig. 2.8 (a), (b). Three equally spaced locations (A, B, and C) were measured, and the moment when the laser beam passed directly over each point is defined as t = 0 s to establish a consistent temporal reference between the experiment and simulation. The same spatial positions were extracted from the numerical model to ensure direct comparability between the measured and predicted temperature histories. Such a point-wise comparison allows the validity of the equivalent heat source to be evaluated not only qualitatively through the temperature field morphology, but also quantitatively through the transient thermal response at representative locations along the weld path.

In the experimental measurement, the surface temperature at the molten pool region reached peak values of approximately 1500~1700 K after laser irradiation. This temperature range is consistent with typical peak temperatures observed in high-power laser welding where the molten pool surface is partially influenced by heat loss to the surroundings. The temperature decreased gradually to around 1000 K within approximately 0.5 s. This cooling trend reflects the combined effects of heat conduction into the material and convective and radiative losses at the surface. The gradual decline also captures the characteristic thermal relaxation of the molten pool as it transitions to the solidification stage.

The numerical simulation reproduced the same overall cooling tendency; however, the predicted temperatures are consistently higher, with peak values in the range of 1900~2100 K and temperatures of around 1200 K at t = 0.5 s. Compared with the experiment, these values are approximately 200~400 K higher throughout the thermal cycle, as shown in Fig. 2.8 (c). This temperature offset appears systematically at all three measured points, indicating that the discrepancy is not due to local numerical instability but rather arises from inherent differences between the physical experiment and the simplified numerical model.

In the experimental process, the molten pool surface was continuously exposed to a flowing shielding gas, which enhances convective heat extraction and lowers the measured surface temperature. This cooling mechanism is not included in the numerical model, where surface heat loss is limited to radiation and conduction, resulting in higher simulated temperatures. The influence of shielding gas convection is particularly significant for laser welding because the gas jet not only protects the molten pool but also continuously removes heat through forced convection. Near the peak-temperature region, the cooling effect is intensified by the large temperature gradient between the molten pool and the surrounding gas, leading to experimentally measured values that are systematically lower than those predicted numerically.

Moreover, the experiment involved filler wire feeding during the welding process. Part of the laser energy was absorbed by the welding wire before reaching the substrate, effectively reducing the heat input into the molten pool. The wire interacts with the laser beam while being introduced into the melt and undergoes melting itself, which consumes energy through latent heat. In contrast, the simulation does not include the wire-feeding process, and the entire laser power is deposited onto the workpiece surface according to the defined heat source model. Consequently, the simulated peak temperature is inherently higher because no energy is diverted into wire melting or lost due to beam shielding by the wire. These combined effects naturally lead to the experimentally measured temperature being lower than the simulated prediction.

Even with this temperature offset, the evolution of thermal histories particularly the cooling rates and the relative differences among the three measured locations shows agreement between experiment and simulation. The consistency in temperature decline slopes indicates that the model accurately captures the dominant heat transfer behavior after laser irradiation. The fact that all three points exhibit similar simulated-to-experimental offsets further supports that the difference is systematic rather than random and therefore can be physically explained by the omitted cooling mechanisms and wire absorption effects rather than errors in the computational framework.

This consistency confirms that the equivalent heat source model accurately represents the actual thermal behavior of the molten pool. It also demonstrates that the numerical model provides reliable boundary conditions for subsequent analysis of molten pool dynamics and keyhole behavior. Although the simplified model yields higher absolute temperatures, the good agreement in thermal trends verifies its suitability for analyzing transient molten-pool evolution, including flow patterns, keyhole oscillation, and temperature-dependent material interactions. Overall, the comparison validates the model's capability to simulate the thermal response in dissimilar-metal laser welding with sufficient fidelity for mechanistic investigation.

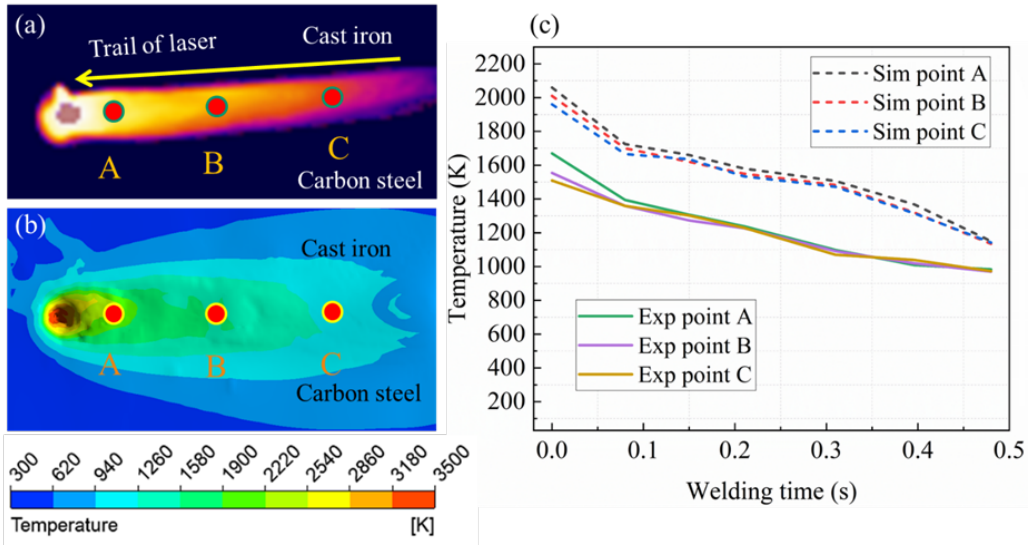


Fig. 2.8. Comparison of experimental and simulated curves on surface heat dissipation (a) Temperature field map in experiment, (b) Temperature field map in simulation, (c) Comparation of cooling temperature curve.

2.4.3. Dynamic keyhole behaviors

Fig. 2.9 illustrates the transient evolution of the keyhole and molten pool under laser irradiation on dissimilar carbon steel and cast-iron. The upper images (a-1 to f-1) present the instantaneous temperature and velocity fields in the longitudinal cross-section, while the lower images (a-2 to f-2) display the corresponding top-view thermal distribution. With the quantitative temperature scale (300~3500 K) and velocity magnitude (0~0.8 m/s), the spatiotemporal coupling of heat transfer, recoil-

pressure-induced melt flow, and interfacial deformation can be evaluated in detail. The laser beam induced high-energy density region develops at the beam center, producing rapid surface vaporization and the formation of keyholes. Recoil pressure reaches its peak near the front keyhole wall, where temperatures exceed 3000 K, and accelerates molten metal downward along the keyhole axis, forming a 0.32~0.48 mm/s melt jet that establishes the initial columnar keyhole shape. Although the applied laser heat input is symmetric, slight thermal asymmetry already appears in the top due to intrinsic differences in thermal conductivity and latent heat between carbon steel and cast-iron.

As irradiation continues, the recoil pressure becomes stronger, deepening the keyhole and increasing the downward jet velocity to approximately 0.72~0.8 m/s. The temperature-dependent surface tension gradient (Marangoni effect) induces tangential shear along the molten surface, generating lateral inflow toward regions of lower surface tension, particularly on the hotter cast-iron side. The combined influence of recoil pressure, Marangoni shear, and conduction into the surrounding solid broadens the isotherms, forming a wider molten region in the top view. With further energy input, the balance between recoil pressure, hydrostatic pressure, and Marangoni convection undergoes local fluctuation, resulting in the necking of the keyhole mid-section. This corresponds to a temporary decrease in temperature to around 2400~2600 K and a reduction in downward jet velocity. Melt flow reorganizes into two counter-rotating vortices with velocities of 0.32~0.48 mm/s, redistributing thermal energy toward both sides of the molten pool and further stretching the temperature contours along the welding direction.

After this transitional stage, the temperature near the front-wall region rises again above 3000 K, reinstating dominant recoil pressure. The downward jet flow establishes itself again, and the keyhole transitions from a constricted shape to a more stable funnel-like geometry. The vertical jet conveys molten material toward the trailing pool, while secondary vortices weaken. In the top view, the molten region develops a streamlined, lens-shaped footprint that extends along the beam path, with

the peak temperature consistently located near the keyhole front. Toward the quasi-steady stage, the keyhole adopts its characteristic elongated shape slightly flared at the top and tapered at the bottom while sustaining melt velocities in the range of 0.48~0.56 mm/s. Although minor oscillations persist, they do not induce collapse. Throughout this process, the molten pool exhibits persistent asymmetry between the steel and cast-iron sides. This originates from their thermophysical mismatch: carbon steel's higher thermal conductivity promotes rapid lateral dissipation, reducing peak temperatures and limiting molten-pool expansion on that side; cast-iron's lower conductivity and broader mushy-zone behavior concentrate heat near the surface, leading to more pronounced melting and more intense Marangoni driven outward flow. Additionally, cast-iron's lower viscosity enhances fluid mobility, while the steeper negative surface-tension gradient on its side strengthens the thermocapillary flow, causing extended recirculation zones and larger molten pool spreading.

The combined evidence from the temperature field, keyhole morphology, and flow distribution demonstrates that the dynamic behavior of the keyhole is governed by the interplay of recoil pressure, Marangoni convection, hydrostatic resistance, and inertia of the molten metal. Material-property differences between steel and cast-iron further modulate the flow asymmetry and thermal distribution, ultimately shaping the molten-pool morphology. From initial penetration through transient instability to quasi-steady elongation, the keyhole evolution reflects a complex spatiotemporal balance of laser absorption, vapor-induced pressure, thermocapillary forces, and asymmetric heat conduction inherent to dissimilar metal welding.

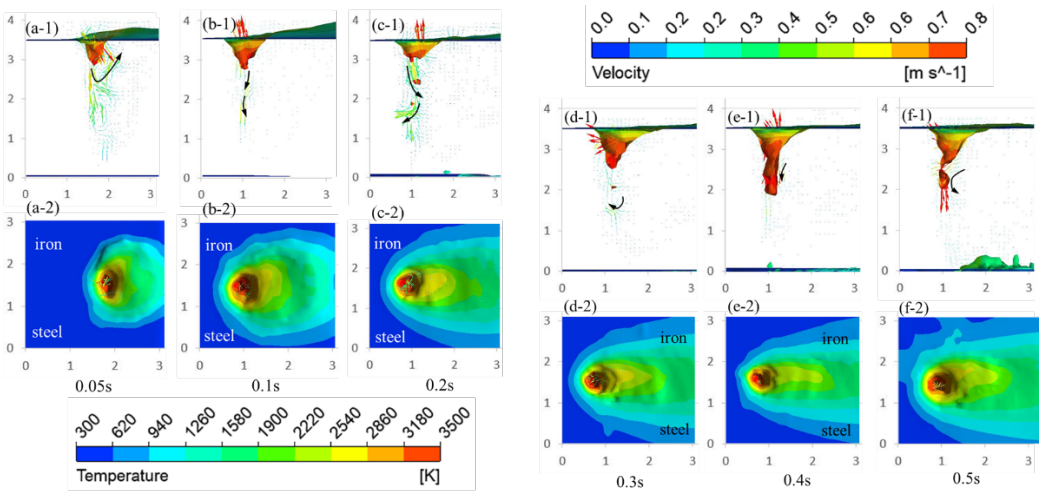


Fig. 2.9. Transient evolution of keyhole dynamics and molten pool flow of middle-section (a-1) to (f-1) Longitudinal section view, (a-2) to (f-2) Top view.

To further elucidate the mechanisms underlying the transient keyhole evolution described previously, Fig. 2.10 presents an interface-resolved visualization of the temperature distribution and surface-normal flow vectors along the keyhole wall. Compared with the macroscopic thermal–fluid fields, this representation captures the local force balance acting directly on the vapor–liquid interface, which ultimately governs keyhole shape, oscillation, and stability.

At the onset of laser irradiation, temperatures on the front wall exceed 3000 K, generating a sharply localized recoil-pressure thrust. The interface vectors indicate that this recoil force is concentrated in a narrow region where absorbed laser intensity peaks, producing the initial downward jet identified earlier. This confirms that the jet originates from a confined vapor-driven impulse rather than a uniform pressure field.

Along the inclined sidewalls, steep temperature gradients induce Marangoni shear stress. These tangential shear forces interact with the downward jet, creating lateral or upward interfacial flows depending on the local surface-tension gradient. Owing to the thermophysical contrast between carbon steel and cast-iron, these shear-driven flows become asymmetric, weakening the jet momentum in certain regions and promoting mid-section deformation consistent with the temporary keyhole necking previously observed.

As welding progresses toward a quasi-steady regime, the interfacial fields show that recoil pressure, conduction, and Marangoni stresses gradually re-establish a repeating balance. The magnitude of lateral shear decreases, and the downward jet becomes coherent again, stabilizing the keyhole into a funnel-like shape. Nevertheless, small oscillations remain along the interface, highlighting that microscale vapor-surface interactions continuously perturb the keyhole even when the macroscopic molten pool appears stable.

In summary, the interface-focused analysis deepens the mechanistic understanding of keyhole dynamics by revealing how recoil pressure and surface-tension-driven shear locally compete or cooperate along the keyhole wall. metasomatized interactions, strongly influenced by the asymmetric thermal properties of the two base metals, play a decisive role in initiating transient deformation and guiding the pathway toward a stable keyhole morphology.

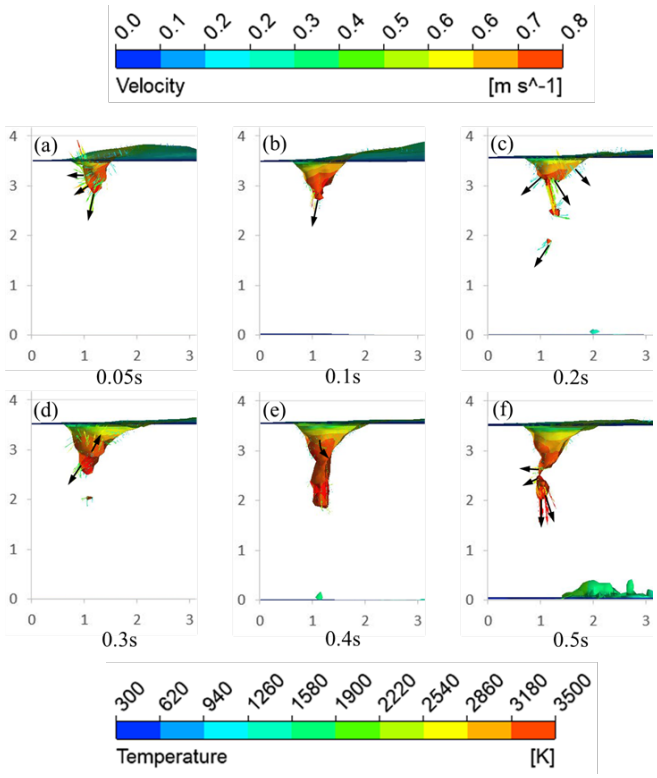


Fig. 2.10. Transient keyhole dynamics and its surface flow pattern.

2.4.4. Velocity field in molten pool

The early-stage flow evolution shown in Fig. 2.11 represents the transitional regime that precedes the onset of keyhole-mode laser welding. During the initial 0.002~0.006 s shown in Fig. 2.11 (a) to (c), the molten pool dynamics are governed primarily by buoyancy-driven natural convection and Marangoni stresses at the free surface. The upward motion along the beam axis and subsequent lateral spreading produce a relatively stable, single-loop circulation pattern with low characteristic velocities. This regime reflects a thermally driven melt flow typical of conduction-mode welding, where the absorbed laser energy is insufficient to induce localized vapor recoil.

As the process proceeds toward 0.008~0.012 s shown in Fig. 2.11 (d) to (f), the temperature near the beam center rises rapidly and approaches the evaporation threshold. This temperature escalation fundamentally alters the balance of forces acting within the molten pool. The flow field becomes increasingly unstable, the velocity magnitude nearly quadruples, and multi-vortex structures develop inside the molten region. These vortical motions are strong indicators that Marangoni convection is intensifying and that the first instances of vapor-driven pressure are emerging at the free surface. The formation of an upward melt jet, accompanied by sharper thermal gradients and concentrated surface shear stress, marks the system's progression toward the critical condition required for keyhole initiation.

This transitional behavior is essential for understanding the subsequent keyhole dynamics. Once the recoil pressure surpasses the combined effects of hydrostatic pressure and surface tension, the molten surface locally depresses, giving rise to the initial keyhole cavity. From this point forward, the dominant driving mechanism shifts from natural convection to recoil-pressure-controlled downward melt flow, significantly amplifying the axial jet and altering the entire flow topology. Therefore, the early-stage evolution captured in Figure 2.11 not only reveals the mechanisms responsible for destabilizing the molten pool but also provides the physical basis for interpreting the fully developed keyhole behavior presented in the following sections.

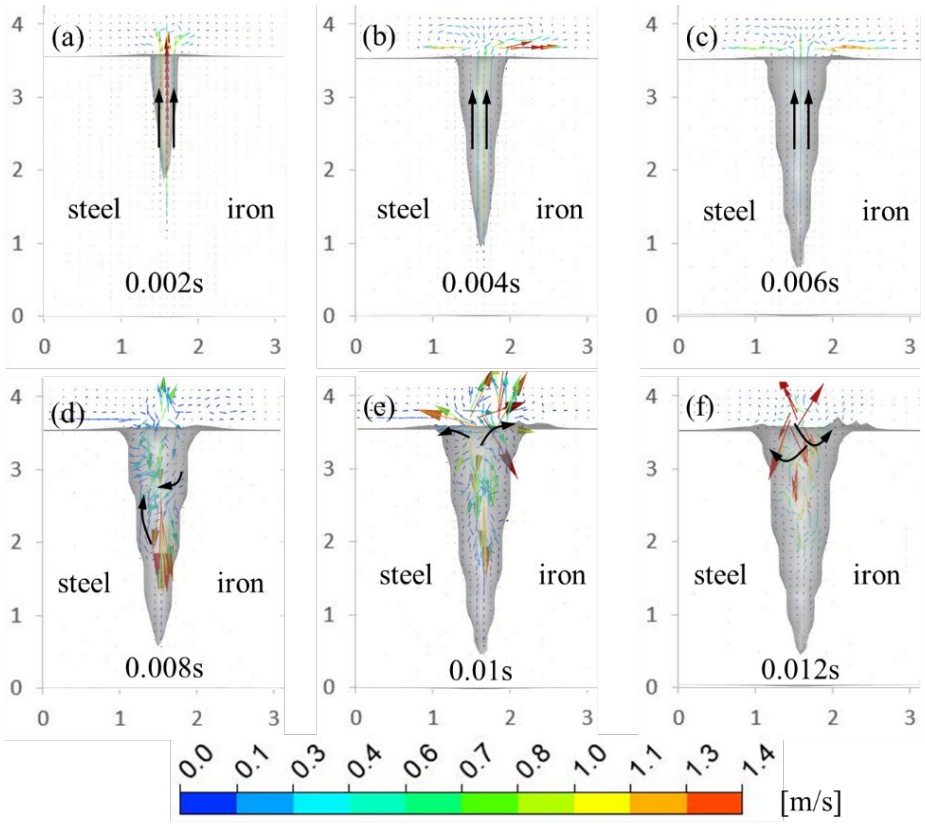


Fig. 2.11. Velocity distribution on transverse cross-section of molten pool.

Fig. 2.12 shows the flow field inside the molten pool in transverse cross-section between 0.20 and 0.25 s, corresponding to the quasi-steady stage of heat input. The semi-transparent gray region outlines the molten pool boundary. Currently, the temperature at the laser beam is maintained above the evaporation temperature, so a keyhole is continuously sustained. The dominant driving force of the flow is the coupling of recoil-pressure–induced flow inside the keyhole and surface-tension-driven convection at the free surface, while buoyancy and the thermophysical differential between steel and cast-iron modulate the overall asymmetry. In all frames shown in Fig. 2.12, a strong downward flow can be observed along the keyhole central with the velocity around 0.8~1.4 m/s, which induces on the lower part of the molten pool and then turns upward along the sidewalls, forming closed recirculation flow pattern in both the steel and iron sides. Local fluctuations and the vortices near

the keyhole wall cause small oscillations of the keyhole interface, these oscillations on the contrary influence the local temperature distribution and give rise to slight forming and collapse motions of the keyhole, but the overall depth and width remain nearly constant during this period.

Although the interior flow is controlled mainly by recoil pressure, the liquid motion near the top surface is still dominated by Marangoni convection. The temperature gradient from the keyhole boundary toward the lower temperature region produces a surface-tension gradient that drives molten metal radially outward along the pool surface. This outward flow is clearly reflected by the vectors near the free surface, and it is responsible for the accumulation of molten metal toward the pool. As a result, the upper part of the molten pool exhibits a larger lateral extent than the lower part, leading to a characteristic “top-widened” shape. The slight difference in flow intensity and vortex size between the steel and cast-iron sides originates from their different thermal conductivity and viscosity: heat is transported more efficiently in the steel side, so the surface flow there is somewhat more extended, whereas the higher viscosity on the cast-iron side suppresses the lateral spreading. Overall, the flow pattern in 0.20~0.25 s indicates that, once the keyhole has reached a statistically steady state, the molten pool is governed by a dynamic equilibrium among recoil pressure, Marangoni convection, buoyancy, and material-property mismatch, in which the surface-driven outward flow explains the larger volume of the upper molten pool compared with its lower part.

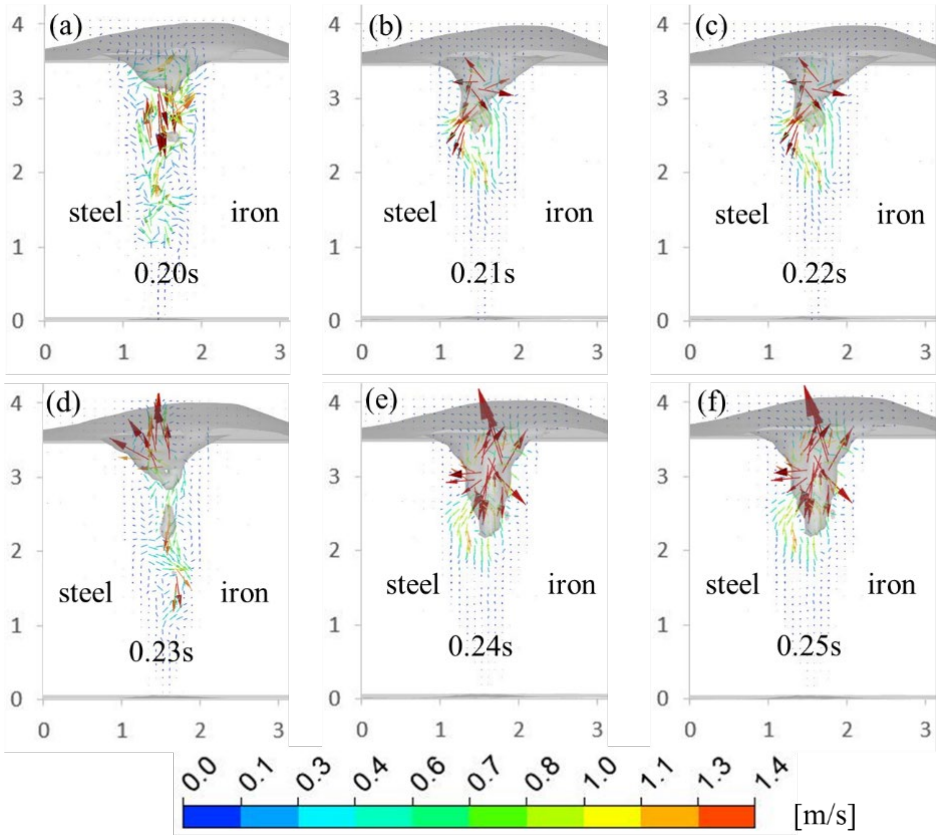


Fig. 2.12. Velocity distribution on transverse cross-section at keyhole location.

Fig. 2.13 provides a longitudinal-section view of the molten pool and keyhole region between 0.20 and 0.25 s. The semi-transparent gray region outlines the molten pool boundary, while the dashed blue contour marks the keyhole boundary. In this section, the melt flow distribution clearly reveals how the vertical and longitudinal momentum pathways evolve under stable high-energy laser irradiation.

Near the keyhole, the recoil-pressure-driven jet generates strong vertical momentum, leading to pronounced upward and downward flow bifurcation. This results in highly localized velocity peak immediately beneath the keyhole, where instantaneous acceleration induces the formation of small vortices, as seen in Fig. 2.13 (a) to (c). These features indicate a strong vertical shear layer that is unique to the longitudinal flow pattern.

Along the rear wall of the molten pool, the longitudinal flow becomes more directional and coherent. Molten metal is advected downward from the keyhole and subsequently guided rearward along the pool boundary. This produces a persistent material-transport pathway extending toward the tail of the molten pool. The longitudinal section clearly reveals the accumulation of molten metal in the pool's trailing region, where the molten pool becomes thicker and more elongated compared with the frontal portion. This rearward thickening is a characteristic signature of keyhole-mode welding and represents a long-range redistribution process only visible in the longitudinal perspective.

Another feature unique to this longitudinal viewpoint is the interplay between vertical convection and the oscillatory motion of the keyhole front. The periodic perturbation of the keyhole wall induced by vaporization pressure and surface-tension variation, causes alternating expansion and contraction of the keyhole outline. These oscillations directly modulate the vertical jet strength, thereby influencing the downstream longitudinal transport. Between 0.23 and 0.25 s as shown in Fig. 2.13 (d) to (f), this coupling leads to brief intensification of downward flow followed by lateral divergence, illustrating the dynamic feedback between keyhole stability and molten pool elongation.

Overall, the longitudinal-section analysis provides essential insight into the through-thickness flow structure and the front–rear redistribution mechanisms that govern molten-pool formation in keyhole laser welding. Unlike transverse views that highlight radial circulation, this perspective clarifies how vertical jetting, rear-wall advection, and keyhole oscillations collectively determine the pool's lengthwise evolution and tail-region metal accumulation.

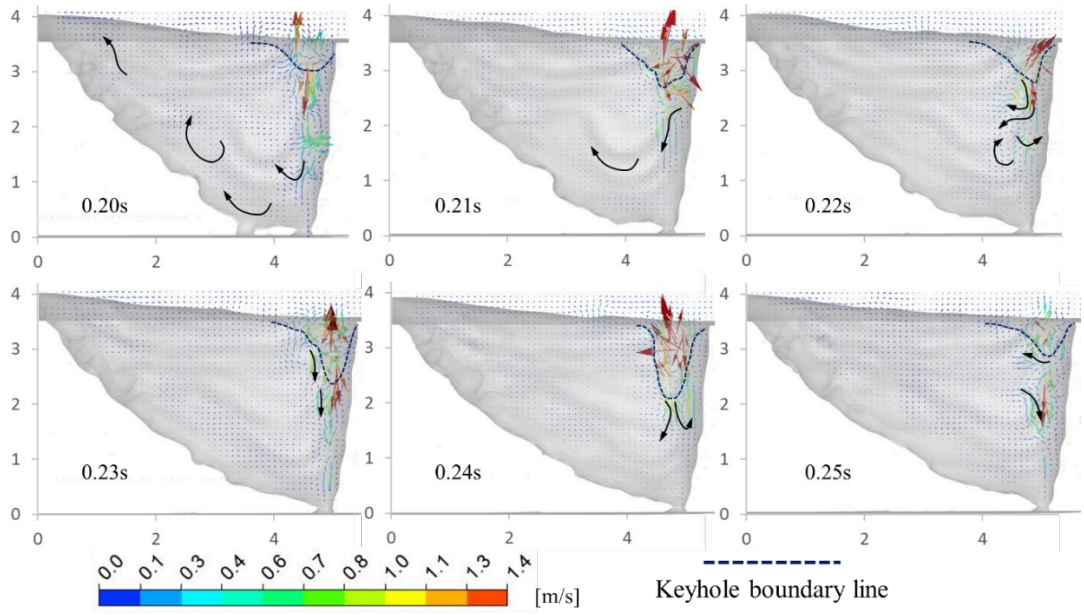


Fig. 2.13. Velocity distribution on the longitudinal cross-section.

2.4.5. Materials volume fraction

Fig. 2.14 illustrates the temporal evolution of material mixing at the transverse section directly beneath the laser beam. Because this observation plane intersects the keyhole throughout the entire welding process, the interface morphology seen here is fundamentally different from the classical diffusion-controlled intermixing that occurs in solid–liquid interactions. In this configuration, the molten region is continually refreshed by the advancing laser beam and by the oscillatory dynamics of the keyhole, meaning that the interface visible in this plane does not represent a time-accumulated diffusion layer. Instead, its geometry should be interpreted as an instantaneous of the convective interaction between the two molten phases at the keyhole boundary. As a result, the mixed-layer thickness remains nearly constant, and its fluctuations are dominated by transient flow patterns rather than long-term diffusive transport.

The transition zone defined by intermediate phase-ID (VOF) values between steel and cast-iron are persistently confined to a width of approximately 0.25~0.40 mm.

This narrow range remains consistent across all time frames. Furthermore, the temporal variation of the interface width is limited to within ±0.05 mm, indicating that no systematic broadening occurs as welding proceeds. This stability confirms that interfacial mixing immediately beneath the laser beam is dominated by transient entrainment, arising from local fluctuations in keyhole shape and melted flow intensity, rather than by cumulative growth mechanisms such as molecular diffusion, long-range convection, or repeated thermal cycling.

The physical mechanisms governing this behavior can be attributed to the highly dynamic of keyhole laser welding. The keyhole experiences continuous oscillations driven by recoil pressure fluctuations, keyhole wall evaporation, and surface tension perturbations. These oscillations generate alternating suction and ejection events along the keyhole wall. During the suction phase, melting originating from one side (steel) is momentarily drawn toward the keyhole centerline, locally penetrating the opposite molten material (cast-iron). Conversely, during the ejection phase, melt is expelled outward, partially restoring the material separation. These cyclic motions generate tongue-like protrusions, wavy interfacial patterns, and fragmented patches visible in the figure.

Because this region is located directly beneath the laser beam, any molten material drawn toward the interaction zone is rapidly replaced by fresh, unmixed steel and cast-iron from the surrounding solid layers. This continuous replenishment prevents the formation of a progressively thickening intermixing band. Even though convective intensification occurs near the keyhole due to recoil-pressure–driven jets and Marangoni-induced shear flows, the molten residence time at this specific plane is extremely short. Therefore, the degree of mixing represents only the instantaneous balance between inflow and replenishment, rather than a cumulative mixing process.

This behavior contrasts sharply with regions downstream of the keyhole, where the molten pool is no longer constantly renewed by direct laser impingement. In those downstream areas, the interface may broaden because of sustained convection, thermal diffusion, and partial mixing during solidification. Thus, the mixing

mechanism at the keyhole plane is oscillation-dominated, whereas the mixing mechanism in the molten trailing pool is convection-dominated and partially solidification-controlled.

The results clearly demonstrate that at the laser interaction zone, the dissimilar material interface, is governed by instantaneous keyhole dynamics, showing a nearly time-invariant thickness with superimposed high-frequency morphological fluctuations. The mixed-layer width remains consistently narrow due to continuous material replenishment and intense local flow oscillations. This is fundamentally different from the behavior observed in downstream weld regions, where mixing can accumulate over time. These findings highlight the necessity of distinguishing between local instantaneous mixing at the keyhole and global cumulative mixing in the molten pool when analyzing dissimilar-metal laser welding processes.

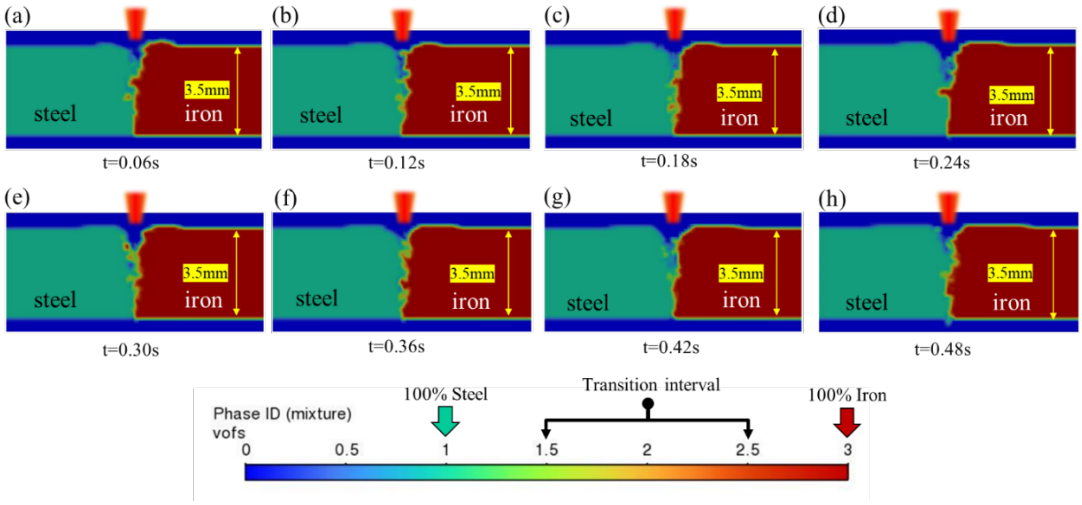


Fig. 2.14. Cross-sectional distribution of steel and cast iron at the keyhole location at various welding times.

Fig. 2.15 summarizes the solidified material distribution at multiple transverse sections along the 16 mm weld length. Based on the Phase-ID field, the width and penetration of the mixed region between carbon steel and cast-iron are quantitatively evaluated. Across all sampled positions, the mixed behavior is consistently concentrated in the upper portion of the molten pool, whereas the lower region retains

a comparatively sharp and well-defined steel–iron interface. This indicates that the dominant mixing mechanisms keyhole-driven convection and surface-tension–induced shear primarily affect the upper melt domain.

Quantitative measurements show that the thickness of the mixed zone in the upper molten region ranges from 0.30 to 0.55 mm, representing the most active portion of the transition layer. In contrast, the corresponding mixed-layer thickness in the lower region remains to 0.10~0.15 mm, showing that interfacial transport is strongly localized near the top part of the keyhole-dominated convection zone and declines rapidly with increasing depth. This vertical gradient in mixing intensity is consistent with the previously analyzed melt flow fields, where strong recirculating motion and keyhole oscillations are shown to diminish near the molten pool bottom.

The early-stage sections at x = −6 mm and x = −4 mm exhibit markedly larger interfacial disturbances than the lower part of molten pool and quasi-steady sections. At these upstream locations, the effective mixed-layer thickness increases to 0.50~0.55 mm, approximately 15% greater than the values measured near the quasi-steady state section (x = 0~2 mm). Moreover, the deviation of the steel–iron boundary position increases from approximately 0.08 mm in the lower region to 0.12~0.14 mm in the upper region of the molten pool. This enhanced boundary fluctuation quantitatively demonstrates that the early transient phase of molten-pool development is accompanied by intensified interfacial instability and more vigorous mixing behavior.

Beyond the layer thickness, the entrainment depth defined as the maximum penetration distance of one material tongue into the neighboring side provides additional insight into convection strength. At upper molten region (x = −6 mm and x = −4 mm), steel entrainment into the cast-iron side reaches 0.45–0.60 mm, whereas only 0.20~0.30 mm of penetration is observed in the lower molten region. This difference corroborates the flow-field analysis presented in earlier sections, where high-frequency recoil-pressure fluctuations and strong shear stresses around the

keyhole are shown to generate transient suction and ejection cycles that enhance material entrainment during the early stage of welding.

Overall, the quantitative evidence including mixed-layer thickness, boundary fluctuation amplitude, and entrainment depth demonstrates that dissimilar-material mixing at the laser interaction zone is governed primarily by transient, convection-driven mechanisms rather than diffusion or long-term accumulation. The mixed-layer thickness remains essentially bounded, but its morphology exhibits high-frequency oscillations driven by keyhole dynamics. This behavior contrasts sharply with the downstream weld region, where the molten pool becomes more stabilized and the interface correspondingly smoother and less disturbed. These findings highlight the inherently dynamic and spatially localized nature of dissimilar-metal mixing in keyhole laser welding.

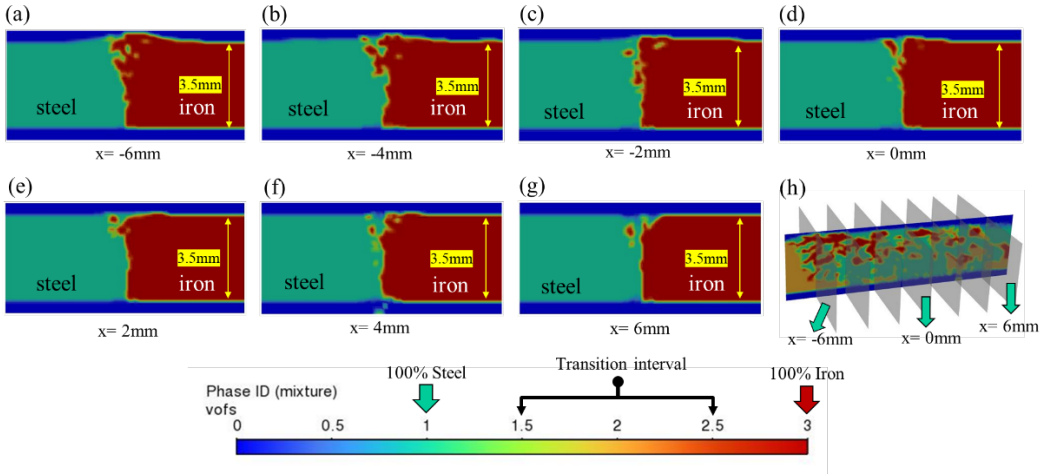


Fig. 2.15. Cross-sectional distribution of steel and cast iron at the keyhole location at different locations after solidification.

Fig. 2.16 presents the three-dimensional distribution of the transition zone between carbon steel and cast-iron by extracting the interfacial plane from the solidified weld. The semi-transparent middle section corresponds to the original joining interface before welding, regarding as a geometric reference for evaluating intermixing. To visualize the intermixing more clearly, the two subfigures are displayed in a mirrored

configuration: Fig. 2.16 (a) shows steel intrusions into the cast-iron side, and Fig. 2.16 (b) shows cast-iron intrusions into the steel side.

The colored iso-surfaces, representing intermediate Phase-ID values between 1.5~2.5, highlight the regions where significant intermixing occurs. The lines of identical color and shape across the two views correspond to the same physical locations in the simulation domain, allowing direct comparison of the penetration morphology from each material's perspective.

Unlike the transverse cross-sections analyzed in the previous section—which emphasized the interface thickness at discrete locations, this figure provides a global, longitudinally continuous visualization of how the interface develops along the entire weld length. The transition region is not uniform: instead, it displays an island-shaped distribution of intrusion regions. This patch-like morphology directly reflects the spatiotemporal fluctuations of melted flow around the keyhole during welding.

A key feature revealed by this figure is the asymmetric mixing behavior between the two materials. Steel shows a relatively deeper and more elongated penetration pattern into the cast-iron side, while cast-iron tends to intrude into the steel side in shorter, more fragmented clusters. This asymmetry arises from intrinsic differences in thermophysical properties: carbon steel shows lower viscosity and higher thermal conductivity, enabling its melt to be more readily entrained by keyhole-driven convection. In contrast, the cast-iron melt, being more viscous and having a sharper liquidus–solidus interval, forms more localized intrusions characterized by smaller coherent structures.

The figure also illustrates that the mixing does not occur uniformly along the weld length. Regions near the start position of the welding show more steel-to-iron intrusion, whereas the iron-to-step penetration is slightly more evident toward the trailing region. This spatial variation reflects the evolution of flow intensity inside the molten pool: At the beginning of welding procession, the upper region of molten pool shows a strong recirculation enhances cast-iron entrainment into the carbon steel side. At the lower region of molten pool, as the melt cools and flow attenuate, the carbon

steel side exhibits residual back-flow–induced intrusions into the cast-iron side. Importantly, this distribution pattern indicates that material intermixing is governed by localized flow events, consistent with the conclusions of the previous section. However, Fig. 2.16 uniquely demonstrates that these events are organized into a longitudinal chain of mixing clusters instead of forming a smooth, uniformly thick interface.

Overall, the extracted mid-plane visualization highlights the inherently three-dimensional and discontinuous nature of material mixing in dissimilar keyhole laser welding, revealing complex spatial organization that cannot be captured by single cross-sectional observations alone.

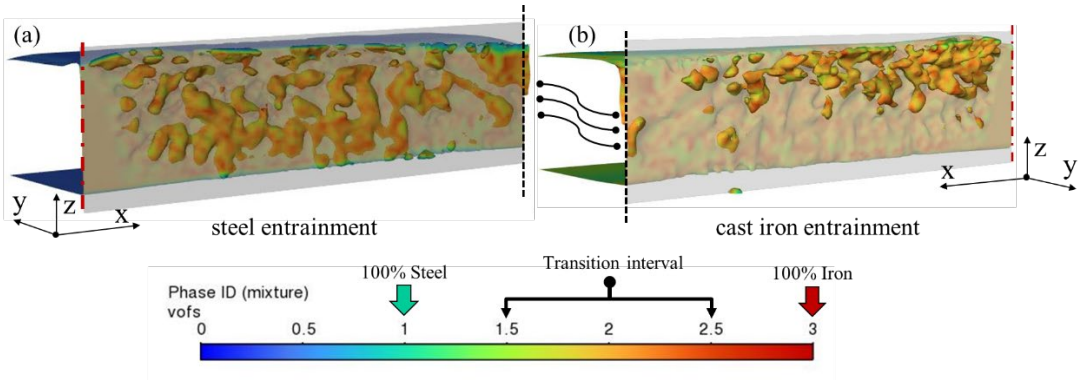


Fig. 2.16. Three-dimensional visualization of dissimilar-metal mixing along the welding interface.

2.5. **Summary**

A three-dimensional CFD simulation was carried out to analyze the thermal–fluid behavior of keyhole laser welding between carbon steel and cast-iron. The model reproduced the transient keyhole evolution, molten-pool development, temperature field, flow patterns, and mixing behavior of dissimilar base metal. The conclusions are summarized below:

(1) The simulated results successfully reproduced the practical welding zone shape, confirming the validity of the equivalent heat source model. Although the predicted temperatures are 200–400 K higher than the experimental values, which

mainly due to the absence of shield gas cooling and filler wire energy absorption in the simulation, the cooling rate and relative temperature differences are well captured.

(2) The keyhole periodic expansion, contraction and localized necking governed by the recoil pressure, and surface-tension forces, which are reproduced consistently, highlighting the unstable of keyhole welding. These transient oscillations strongly influenced interface deformation and the evolution of the molten pool boundary.

(3) The molten pool flow field was dominated by asymmetric circulation and recoil pressure induced downward flow. Due to differences in thermal conductivity, viscosity, and surface-tension gradients between carbon steel and cast-iron, the flow intensity and directionality are unbalanced, which strongly induced asymmetric flow in the molten pool.

(4) Material mixing occurred primarily in the upper region of molten pool, where keyhole-induced convection was strongest. The transition zone remained thin (0.30–0.55 mm) and exhibited discontinuous, island-like penetration clusters along the welding direction, reflecting localized flow disturbance. In contrast, the lower molten region retained a sharp steel–iron boundary due to limited convection.

Chapter 3. Numerical Modelling of Laser Welding Pool Thermal-Dynamics and three Dissimilar Material Mixing with Nickel Alloy Filler Wire

3.1. Introduction

In this study, an EV automobile differential unit is manufactured by laser welding carbon steel to cast-iron with nickel-alloy welding wire to replace conventional bolting for improving the joint strength and reducing weight. However, if the unsuitable laser welding conditions were employed, the crack occurred in the welding metal shown on Fig. 3.1. Concerning the welding crack occurrence, we found that the distribution of the nickel-alloy in the welding metal is one of the vital factors for crack prevention.

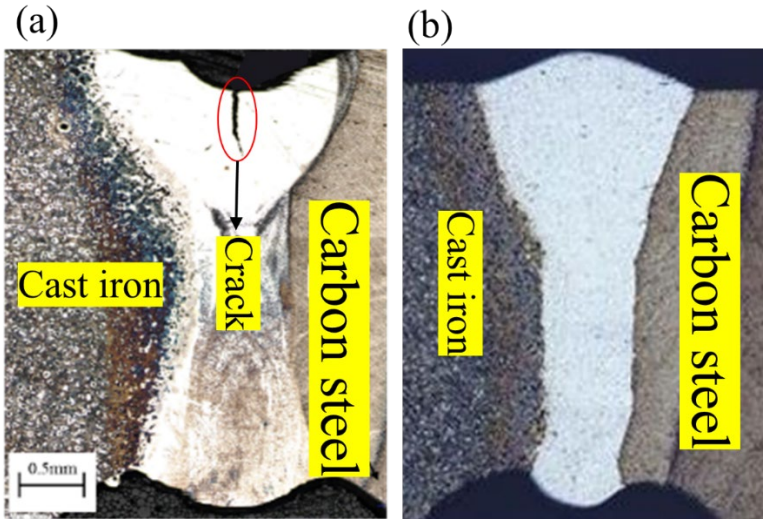


Fig. 3. 1. Cross-sectional macrostructures of dissimilar welding between carbon steel and cast-iron (a) No filler wire, (b) With nickel-alloy filler wire.

To understand the prevention mechanism of weld cracks induced in laser welding dissimilar materials, carbon steel and cast-iron with a nickel-alloy filler wire, it is necessary to investigate the melting pool thermal dynamics, keyhole mechanism and

dissimilar materials mixing. In this study, a novel three-dimensional computational fluid dynamics (CFD) modelling on transient tracking of keyholes, transfer of molten wire droplets, mixing of filler and base metals, welding groove, coupled with conventional model of heat transfer, surface tension and recoil pressure, was developed. The simulated molten pool geometry and temperature field were compared with the experimental results, which confirmed the accuracy of the developed numerical model. The numerical results revealed that the keyhole underwent periodic oscillation and partial collapse, during which entrapped vapor formed transient bubbles that later escaped through buoyancy. The molten wire droplets significantly affected the flow field and local temperature, temporarily weakening Marangoni convection and altering keyhole stability. The nickel-alloy material concentrated primarily on the surface, then flowed into welding pool. After solidification, a large amount (65~75%) of the nickel-alloy material kept in the upper half of the weld metal and a small amount distributed in the lower half zone. These distribution characteristics supplied a graded transition layer between the two dissimilar base metals benefiting to weld crack prevention. This research provided quantitative evaluation in visualizing the in-situ dynamic phenomena of dissimilar materials for laser welding process optimization.

3.2. Welding configuration with filler wire

Building upon the configuration of chapter 2, this chapter introduced laser welding procession using a filler wire. In this case, the same differential unit composed of the ring gear (carbon steel, Cr–Mn steel) and differential case (cast-iron FCD600 equivalent) was joined by laser welding using a nickel-alloy filler wire (MG82, containing at least 72.12% Nickel). The detailed chemical compositions are listed in Table 3.1. The welding configuration remains unchanged, consisting of a circular path with a radius of 56 mm and a 0.4 mm groove width at the upper region of the 3.5 mm–thick base metals. The same YAG laser oscillator is used, providing a perpendicular laser beam with an output power of 2510 W and a 0.4 mm focal spot

diameter, with the focal position located at the bottom of the base metal. The welding is performed along the circular path at a speed of 1.5 m/min.

In the filler-wire welding condition, the MG82 wire is fed at a speed of 2.6 m/min. The wire feeding position could be slightly shifted toward either the carbon steel or the cast-iron side, as illustrated in Fig. 3.2. A centered configuration, shown in Fig. 3.2 (a), corresponded to the wire aligned with the groove center. Since the offset of the wire was not the focus of this study, the case with the wire place at the joint center was selected for analysis in the present work.

Table 3.1. Chemical composition of Chrome-Manganese steel, FCD600 equivalent and MG82

Chrome-Manganese steel		FCD600 equivalent		MG82	
C	0.27	C	3.7	C	0.036
Mn	1.27	Mn	0.51	Mn	2.95
Ni	0.07	Ni	-	Ni	72.12~
Cr	1.27	Cr	-	Cr	19.89
Cu	0.12	Cu	0.56	Cu	<0.005
Si	0.27	Si	2.36	Si	0.10
S	0.03	S	~0.02	S	<0.0005
P	0.015	P	~0.05	P	0.002
Ti	<0.01	Sn	~0.05	Ti	0.36
Al	<0.03	Mo	-	Nb	2.37
				Fe	1.32

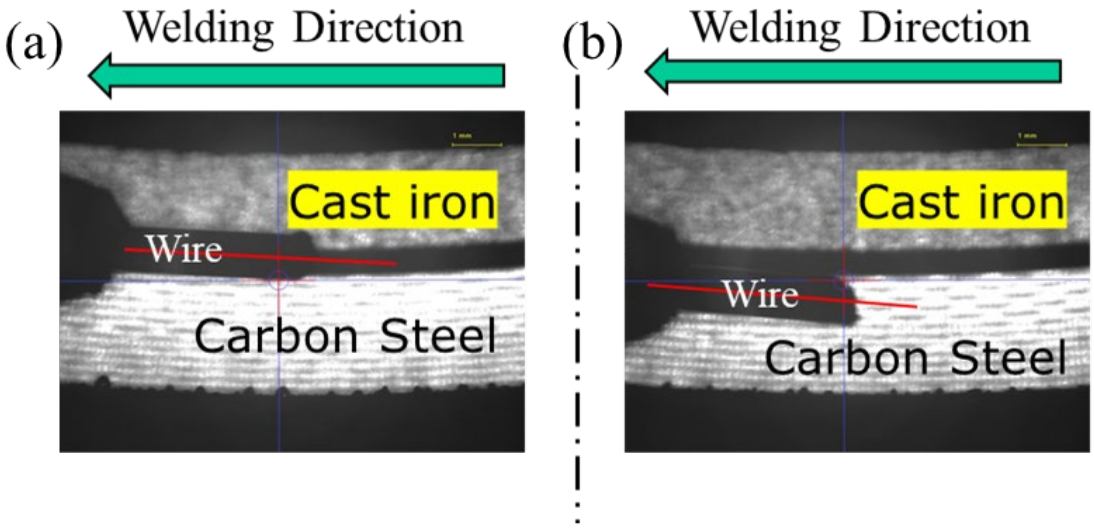


Fig. 3.2. Actual welding experiment procession (a) Wire position at groove center, (b)Wire position at carbon steel.

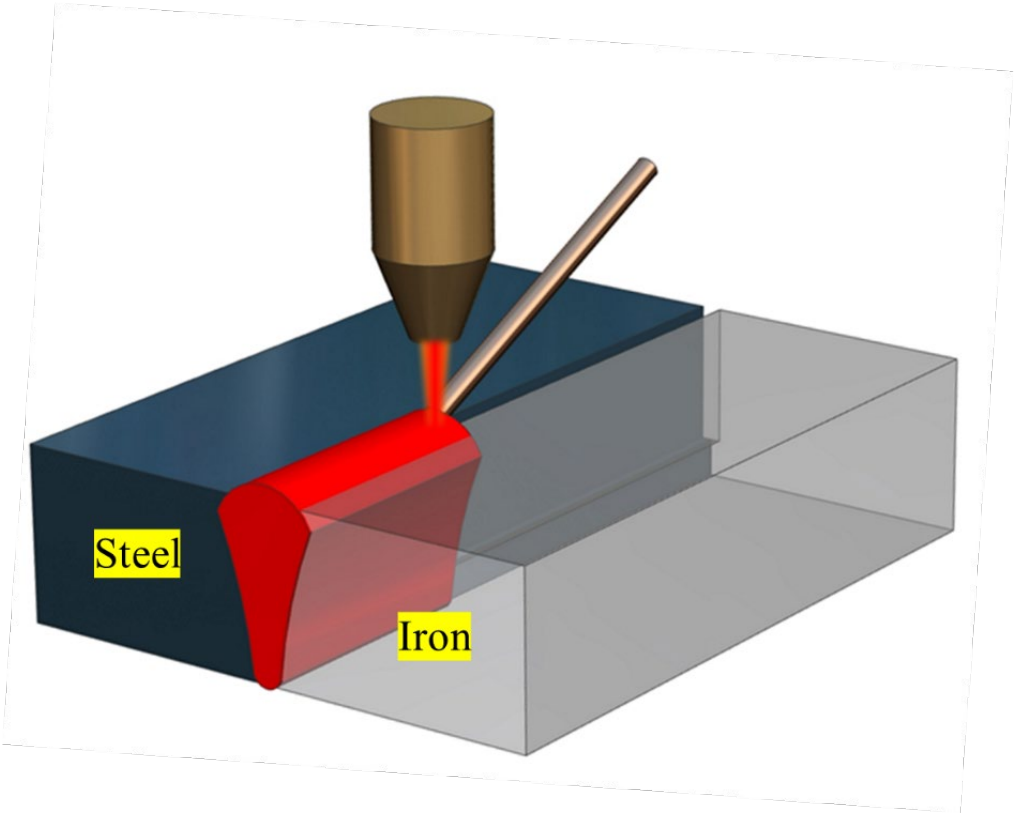


Fig. 3.3. The instruction schematic of welding procession.

3.3. Numerical modeling

3.3.1. Molten droplets model

In the experiment, the filler wire was placed on the front side of the laser beam and fed into the center of the groove. In the numerical simulation, the wire feeding was represented by periodic molten droplet dripping above the molten pool. The volume of each molten droplet was determined based on the actual wire feeding rate and wire diameter, ensuring consistency between the experimental and numerical conditions shown in Fig. 3.4. In this way, the discrete molten droplet model kept numerically stable and physically realistic.

The molten droplet dripping is controlled by a trigonometric function to mimic its periodic dripping behavior. The radius of the molten droplets and moving velocity was controlled by the equation:

$$r_d = \sqrt{(x - v_0 t)^2 + y^2} \quad \text{Eq.3.1}$$

where r_d is the molten droplet radius.

The molten droplet dripping condition is then governed by a sinusoidal function:

$$DC = \sin(2\pi \cdot D_n \cdot t) \quad \text{Eq.3.2}$$

where D_n represents the dripping number which is set as 100 droplets per second. A droplet is considered to enter the molten pool only when two criteria were simultaneously satisfied: the radial distance $r_d \leq 1\ mm$, and the sinusoidal function exceeded a threshold ($DC \geq 0.8$). Under these conditions, the dripping velocity is set to 0.143 m/s, otherwise, no molten droplet entry is allowed. The temperature of molten droplet is set as the melting point temperature of wire material (nickel-alloy) 1650 K.

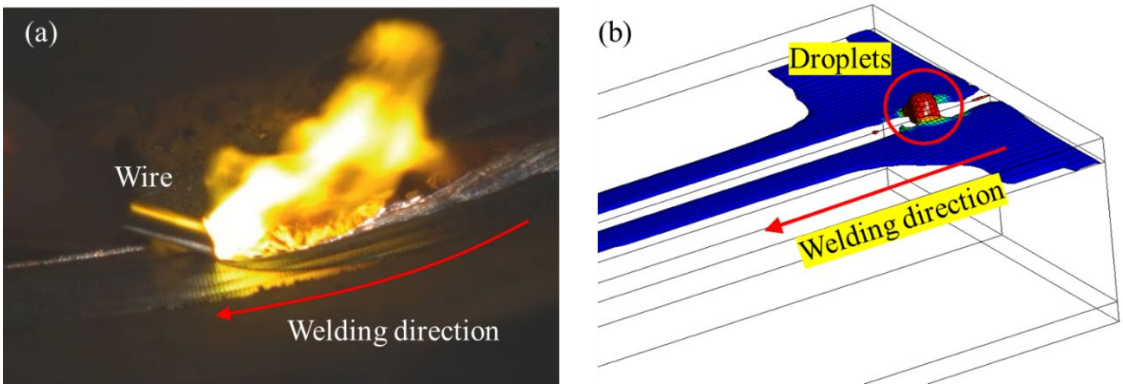


Fig. 3.4. Illustration of welding wire feeding (a) Wire feeding in the experiment, (b) Molten droplet dripping model in the simulation.

3.3.2. Initial conditions

In the numerical setup, the initial regions of the metals and groove were defined through initialization. The width of the groove was 0.35 mm at a depth of 2.5 mm. Blow this 2.5 mm height; the two base metals were assumed to be in direct contact without a gap. The geometric instruction was as Fig. 3.5.

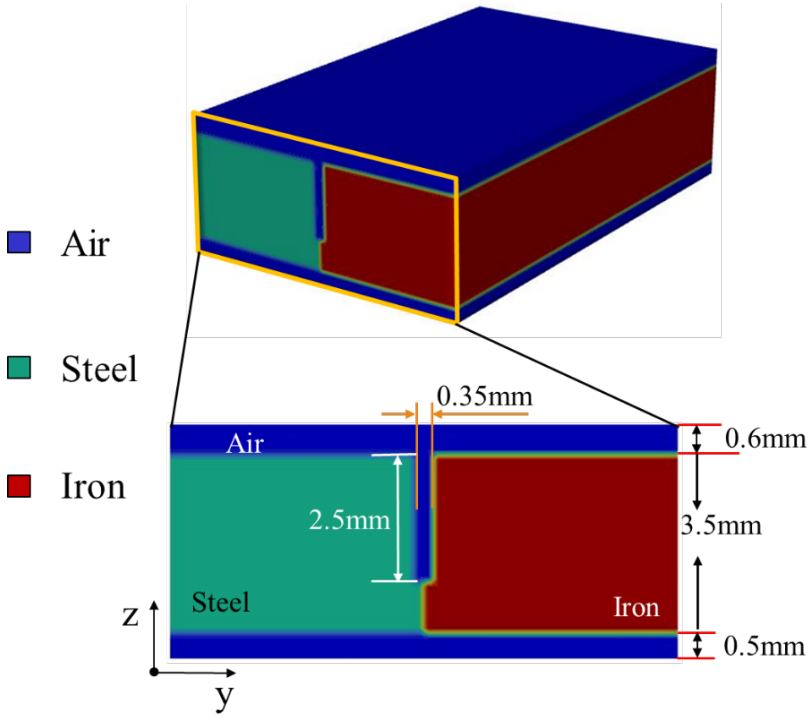


Fig. 3.5. Initial configuration of the base metal domain.

The initial temperature equals 300 K, which is the same as environmental temperature. Because the groove width is smaller than the laser spot diameter, the incident laser energy is primarily distributed within the groove. In the model, the laser beam is therefore interacted only with outer surfaces of the base metals, the groove sidewalls and the base metal blow the groove. This allows the equivalent Gaussian volumetric heat source to be applied only to the base metal, not the air inside of the groove, as illustrated in Fig. 3.6. The calculated welding time is still 0.5 s, which is also 12.5 mm in length. After the welding calculation, a 0.2 s period naturally cooling procedure was also calculated.

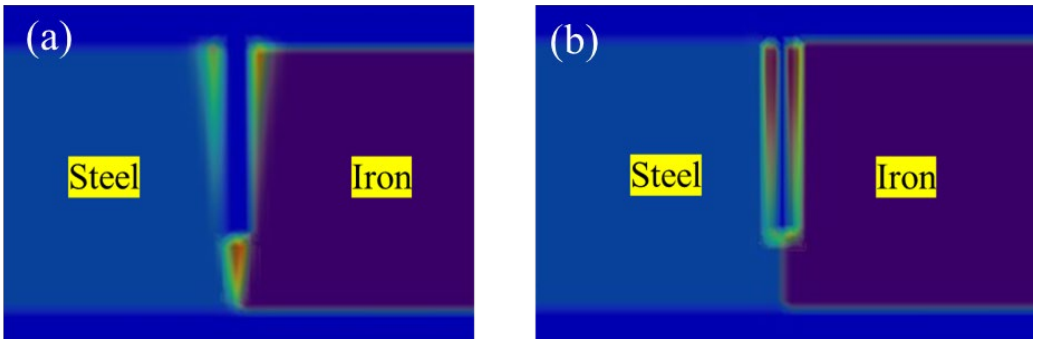


Fig. 3.6. Schematic of the initial heat source configuration (a) The heat source acted inside the metal (b), Heat source acted on the metal surface.

3.3.3. Temperature-dependent material properties

To improve the accuracy of the numerical calculations, the key thermophysical properties of the three metals density, viscosity, and surface tension were experimentally measured. These properties were obtained over a range of temperatures relevant to the welding process and were used as temperature-dependent inputs for the CFD model. Accurate determination of these parameters was essential for capturing the molten pool flow behavior and surface deformation under Marangoni and recoil pressure effects. The experimentally measured temperature-dependent curves of density and viscosity for the three metals are presented in Fig. 3.7 (a) and (b), respectively. The density decreased approximately linearly with temperature, whereas viscosity exhibits a nonlinear decline, indicating enhanced

fluidity at elevated temperatures. The other relevant parameters used in the simulation are summarized in Table 3.2.

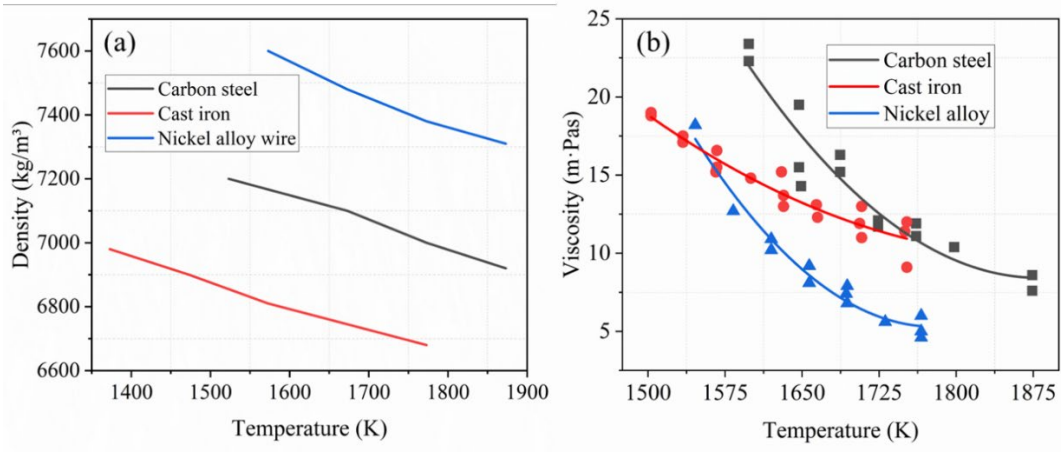


Fig. 3.7. Temperature-dependent thermophysical properties of carbon steel, cast-iron, and nickel-alloy (a) Density, (b) Dynamic viscosity.

Table 3.2. Temperature dependent material properties for base metals and filler wire

Property	Chrome-Manganese steel	FCD600 equivalent	MG82	Units
Specific heat	455~1100	500~950	500~750	$J \cdot kg^{-1} \cdot K^{-1}$
Thermal conductivity	30~40	18~45	17~25	$W \cdot m^{-1} \cdot K^{-1}$
Solidus temperature	1580	1434	1540	K
Liquidus temperature	1623	1473	1600	K
Latent heat of melting	272000	240000	280000	$J \cdot kg^{-1}$
Surface tension	1.74~1.8	1.42~1.6	1.72~1.8	$N \cdot m^{-1}$

3.4. Results and discussions

3.4.1. Molten shape and validation with experiment

Fig. 3.8 presented a comparison between the experimentally observed cross-section and the numerically simulated molten pool profile. The experimental result shows a

deeply, fully penetrated fusion zone extending into the groove and an asymmetric solidification boundary between the steel and cast-iron sides. The corresponding numerical result reproduced the overall pool shape, and the height and width of the molten pool are consistent with the experimental observation. The width of the upper surface of molten pool is 2.01mm, while the simulation result shows a 1.92 mm width at upper surface, which indicated that the applied equivalent heat source accurately represents the laser energy distribution and absorption behavior during welding procession. This consistency demonstrates the applicability and reliability of the developed heat source model for predicting molten pool formation and thermal behavior in current study.

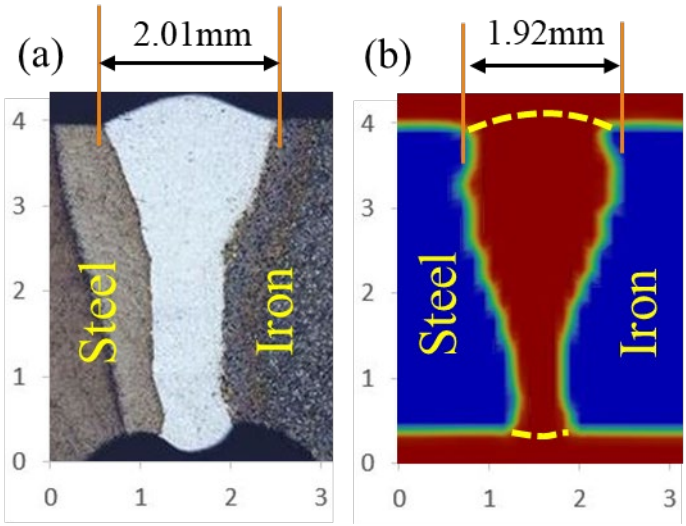


Fig. 3.8. Comparison of molten zone morphology between experiment and simulation (a) Experimental result, (b) Simulated result.

3.4.2. Temperature distribution and validation with experiment

The temperature distribution along the welding direction at the molten pool surface was measured using an infrared thermal imaging camera, which is shown in Fig. 3.9 (a). Three equally spaced points (A, B, and C) are selected for quantitative evaluation, where the time t=0.0 s corresponds to the moment when the laser beam just passed directly over each point. In the numerical simulation shown in Fig. 3.9 (b), three points are selected according to the same spatial criteria as in the experiment to

enable a direct comparison of temperature histories. Fig. 3.9 (c) compares the experimental temperature measurements with the simulated results at the same locations. In the figure, “Exp” refers to the experimentally measured points, while “Sim” denotes the corresponding simulation results. The experimentally measured peak temperatures near the laser beam are found to be between 1500 K and 1700 K, decreasing gradually to about 1000 K approximately 0.5 s after the laser moved away from the observation point. The peak temperatures obtained from the simulation ranged between 1600 K and 1750 K, which is in close agreement with the experimental results. After approximately 0.5 s, the simulated temperatures decreased around 1100 K. Both the experimental and simulated results exhibited similar cooling rate trends. The simulated surface temperature is approximately 200 K higher than the experimental measurement. This discrepancy can be attributed primarily to the influence of the shielding gas flow during the experiments, which continuously removes heat from the molten pool surface. In the present simulation, however, the inflow and outflow of the shielding gas were neglected to simplify the computational model and improve efficiency. Overall, the calculated temperature evolution during the cooling process showed good agreement with the experimental observations, also confirming the reliability of the equivalent heat source model.

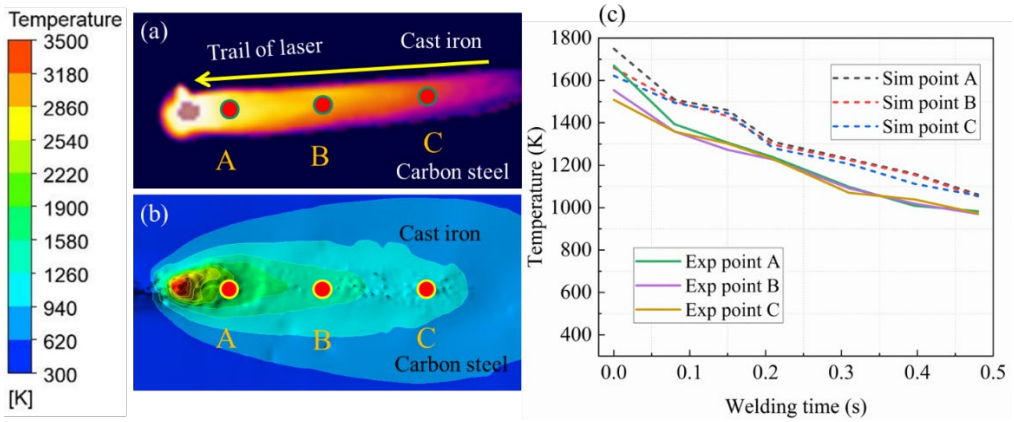


Fig. 3.9. Experimental and simulated curves comparing surface heat dissipation (a) Temperature field map in experiment, (b) Temperature field map in simulation, (c) Comparation of cooling temperature curve

3.4.3. Dynamic keyhole behaviors

The dynamic behavior of the keyhole played an important role in determining molten pool stability, penetration depth, and defect formation such as porosity. In this section, the transient evolution of the keyhole during laser welding is analyzed. Fig. 3.10 illustrates the transient evolution of the keyhole and molten pool geometry, showing both longitudinal section view and top-side view distributions of temperature and flow velocity vector. In the longitudinal view, the velocity vectors are displayed on the keyhole free surface and on a central plane extracted through the middle of the groove, representing the characteristic flow distribution within the molten pool. At the initial stage shown in Fig. 3.10 (a), the laser irradiation rapidly melted the groove bottom, producing a shallow cavity due to recoil pressure. The molten metal is driven upward along the front wall and outward along the free surface, forming an unstable open keyhole. As the laser continued to irradiate shown in Fig. 3.10 (b), the depth and width of keyhole extended along the welding direction, accompanied by a strong upward vapor flow and an opposing downward melt flow that established a closed circulation loop inside the molten pool. The velocity vectors at the keyhole surface are oriented nearly perpendicular to the keyhole wall, indicating an outward expansion trend of the molten metal. The top-view flow vectors revealed a Marangoni-driven circulation from the steel side toward the cast-iron side, producing asymmetric convection patterns consistent with the difference in thermophysical properties between the two materials.

In the subsequent stage shown in Fig. 3.10 (c), the molten pool reached a quasi-steady state where the recoil pressure, surface tension, and hydrostatic forces reach a dynamic balance. Small-scale vortices are observed near the keyhole surface wall, suggesting periodic oscillation and “breathing” of the keyhole. Under this quasi-steady state of the keyhole, the metal fluid in the lower region of the pool flowed backward and upward along the rear wall, forming a recirculating flow pattern beneath the keyhole. This flow behavior resulted from the combination effects of recoil pressure acting on the keyhole bottom and Marangoni convection along the

temperature gradient. The metal near the front wall is pushed downward by vapor recoil, while the fluid near the rear wall rose due to buoyancy and surface tension gradients, establishing a closed-loop circulation within the molten pool. This circulation not only stabilized the keyhole shape but also enhanced heat and material transfer inside the pool.

In Fig. 3.10 (d) to (f), the molten pool gradually expanded toward the cast-iron side. The upward flow near the front wall became weaker, while the rear-wall vortex dominated the internal circulation, leading to slight fluctuation in the keyhole depth and shape. The top-surface temperature distribution evolved into an elongated elliptical profile aligned with the welding direction, and the asymmetric Marangoni flow continued to promote lateral transport of molten metal and alloying elements. During the oscillation of the keyhole, its periodic opening and collapse caused part of the vapor to be trapped beneath the keyhole bottom. As the keyhole closes, these entrapped gases remained within the molten pool, resulting in the formation of voids, as illustrated in Fig. 3.10 (e) and (f).

Overall, the simulated results captured the complete formation, stabilization, and oscillation process of the keyhole. The dynamic interaction between recoil pressure and Marangoni convection iss demonstrated to be the main mechanism governing keyhole morphology and molten-pool stability in dissimilar laser welding of carbon steel and cast-iron.

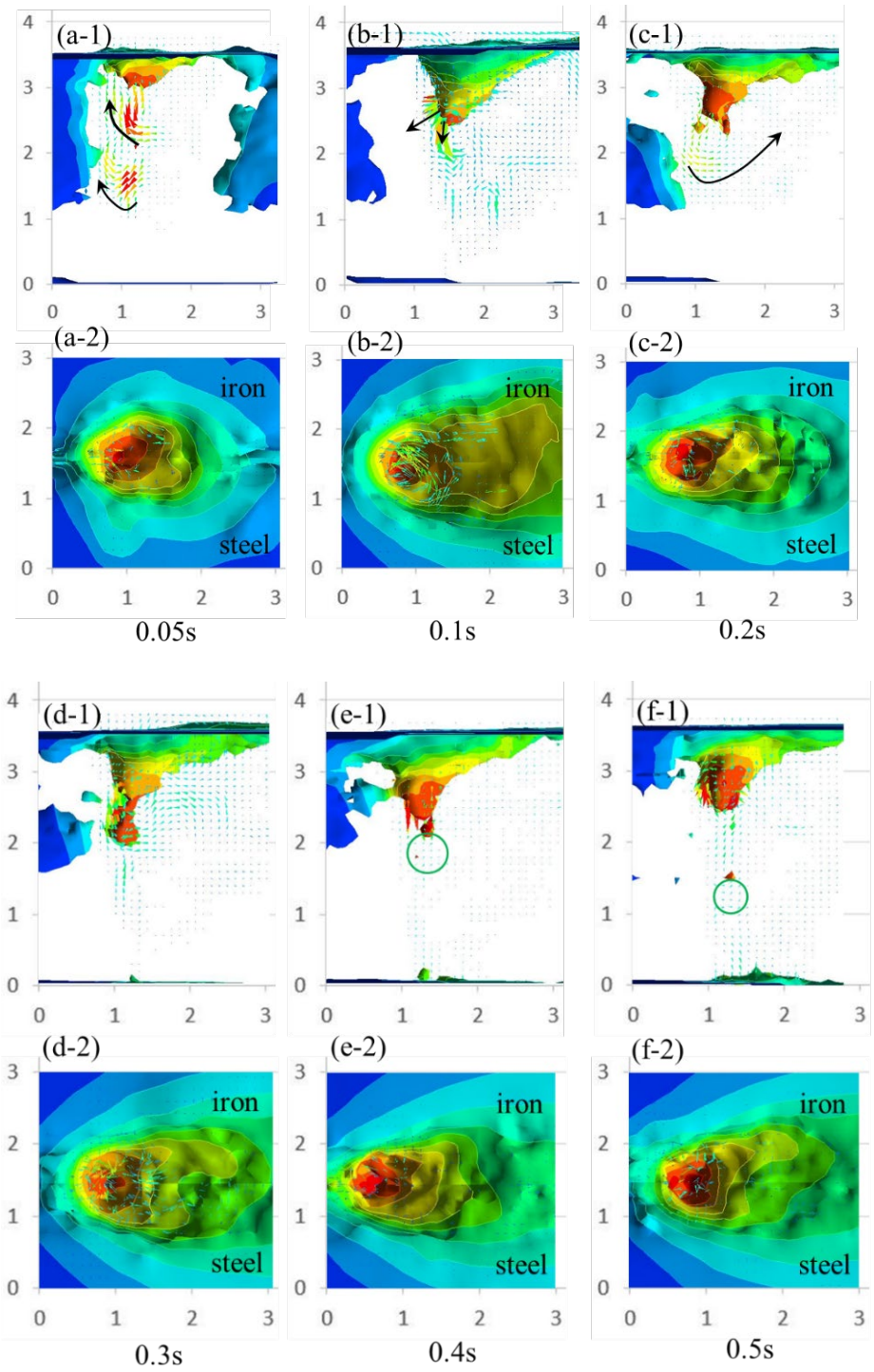


Fig. 3.10. Transient evolution of keyhole dynamics and molten pool flow (a-1) to (f-1) Longitudinal section view, (a-2) to (f-2) Top view.

3.4.4. Molten droplet transfer and mixing behavior

Fig. 3.11 presented the transient behavior of the first molten filler droplet dripping into the groove, showing both the cross-sectional and longitudinal views of the molten pool evolution. The blue region represented the interface between the air and the metallic surface, which visualized the groove morphology during the initial stage of welding, as shown in the cross-sectional views above. In the longitudinal section below, the side close to the observation plane corresponded to the carbon steel. As the groove bottom absorbed the laser energy the base metal melted into liquid, the original groove geometry gradually disappeared. The molten metal filled the region that is initially occupied by air at the bottom of the groove. Consequently, the air–metal interface vanished in this area, appearing as a white cavity in the longitudinal view. It should be noted that this white region did not represent an actual void or pore, rather, it indicated the zone where the molten metal has completely replaced the air because of local melting and flow. This phenomenon marked the transition of the base metal from the solid to the liquid state during the early welding stage, creating favorable conditions for subsequent droplet transfer and mixing within the groove. As the molten droplet approached the groove showed in Fig. 3.11 (b), a portion of the groove wall and the metal at the groove bottom have been melted due to the intense laser irradiation.

When the molten droplet first contacted the molten pool in Fig. 3.11 (c), its thermal energy is rapidly transferred to the base metal, causing an instantaneous expansion of the molten pool and the local temperature near the impact region increased, a strong downward flow developed beneath the droplet, as shown in the longitudinal section. This impact also generated a pressure wave that propagated through the molten pool and slightly enlarged the molten pool.

With continued spreading, the molten droplet metal is entrained into the groove, promoting further melting of the near-edge region and gradual reshaping of the groove profile shown in Fig. 3.11 (d) to (e). The flow is mainly governed by inertia of molten droplet and then by Marangoni shear along the strong surface temperature

gradient. Because a stable vapor channel has not developed at the very beginning of welding procedure, the recoil pressure is negligible, and no gas entrapment is observed at this stage. Instead, in the longitudinal view below, the nickel-alloy volume fraction highlights where the molten droplet first mixed with the molten base metal, discrete Ni-alloy-rich patches appear at the center position of groove. These observations clarified that the first molten droplet primarily conditions groove geometry changing because of the molten droplet dripping phenomenon.

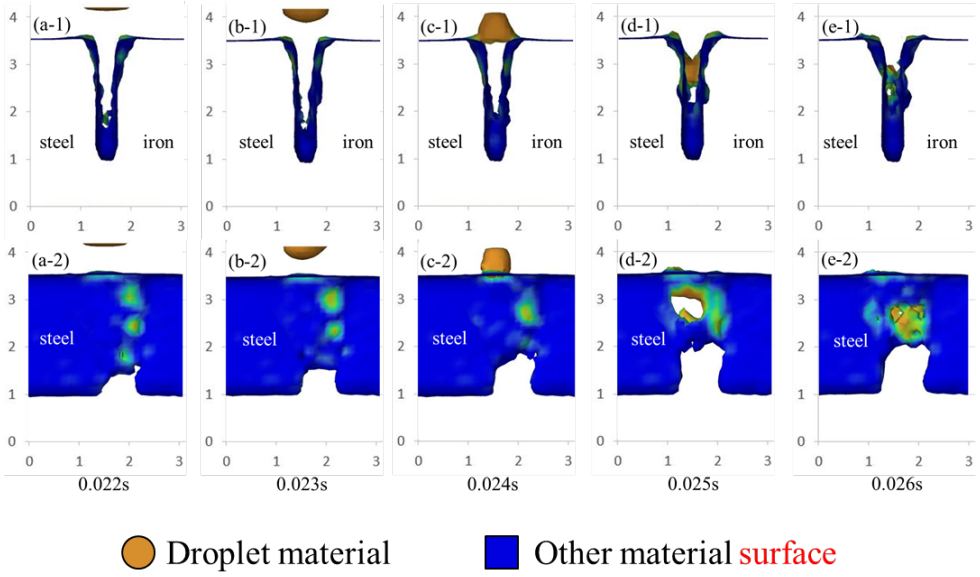


Fig. 3.11. The first molten droplet transfer progress in groove (a-1) to (e-1) Transverse section view, (a-2) to (e-2) Longitudinal section view.

Fig. 3.12 illustrated the transient evolution of the molten pool and keyhole during the transfer of a molten droplet at keyhole formation procedure. When the molten droplet entered the molten pool and contacted the keyhole wall surface, its relatively lower temperature led to a temporary cooling effect in the keyhole region. As a result, the local vapor induced recoil pressure at the keyhole bottom decreased, breaking the balance that sustained the keyhole cavity. Consequently, the keyhole became unstable and partially collapsed from the middle position, trapping a portion of vapor inside the molten pool and forming a transient gas cavity, as shown in Fig. 3.12 (c) and (d). Subsequently, the entrapped gas bubble rose upward and merged with the upper

keyhole driven by buoyancy, releasing the trapped vapor. During this period, the keyhole depth decreased while the opening diameter becomes larger, reflecting a transition from a slender to a shallow–wide morphology shown in Fig. 3.12 (e) and (f). As laser irradiation continued, the molten pool temperature increased again, enhancing evaporation at the keyhole bottom. recoil pressure recovered and dominated the key role leading to the reformation of a deeper, elongated keyhole structure shown in Fig. 3.12 (g) and (h).

In the longitudinal section, the distribution of the nickel-alloy component revealed clear asymmetry caused by surface tension gradient. The Marangoni flow drove the molten nickel-alloy from the front wall toward the rear wall of the molten pool. Consequently, a higher nickel-alloy concentration appeared along the rear surface, while the front side remained relatively less. This directional flow not only promoted the mixing between the filler and base metals but also reflected the strong coupling among surface tension, temperature gradient, and pool convection during dissimilar laser keyhole welding.

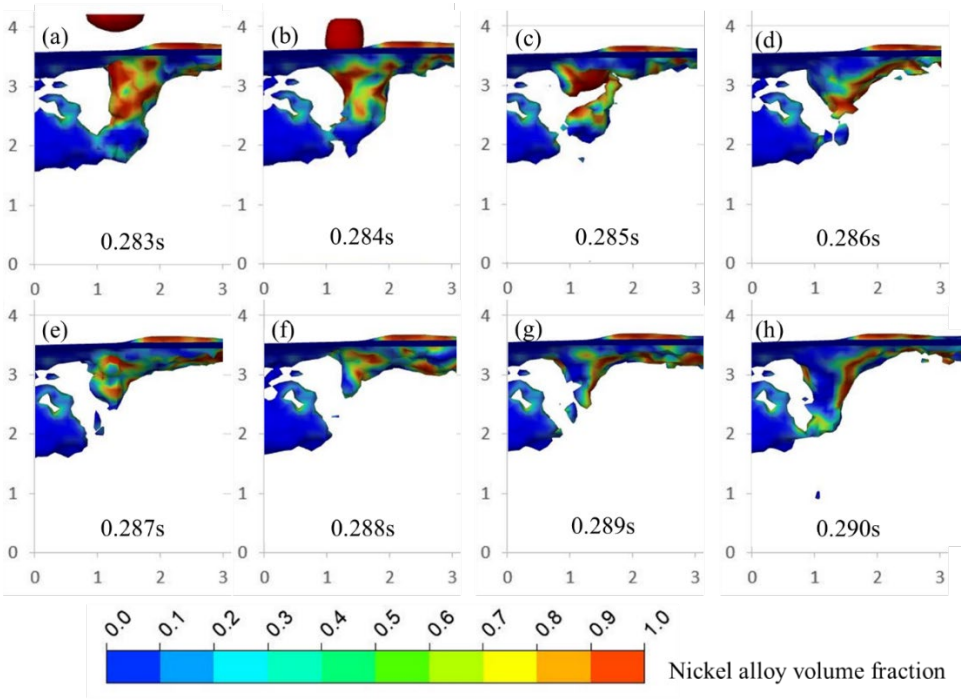


Fig. 3.12. Transient process of molten droplet transfer and material mixing.

3.4.5. Velocity field in molten pool

Fig. 3.13 (a) to (h) showed the velocity field on a transverse cross-section that is located just behind the keyhole, illustrating the evolution of molten metal flow during molten droplet transfer. Before the molten droplet entered the molten pool, the flow inside the molten pool is primarily governed by surface tension and recoil pressure shown in Fig. 3.13 (a), (b). Due to the temperature gradient along the free surface, the Marangoni flow drove the metal fluid toward the cast-iron side, producing an asymmetric circulation. The velocity vectors showed a strong vortex flow pattern, with the maximum velocity reaching approximately 0.5 m/s, which promoted the outward expansion of the upper molten pool and the widening of the keyhole opening.

After the molten droplet dripped into the molten pool shown in Fig. 3.13 (c) and (d), the previous flow equilibrium is disrupted. The molten droplet metal (nickel-alloy) mixed rapidly with the pool metal, altering the temperature distribution. As a result, the temperature gradient between the two sides of the pool is temporarily reduced, weakening the Marangoni effect. The flow velocity decreased to about 0.25~0.3 m/s, and the vortices on both sides become more symmetric around the pool centerline.

With continued mixing and heat transfer shown in Fig. 3.13 (f) to (h), the molten droplet material became fully mixed into the molten pool. The temperature field gradually recovered its original nonuniform distribution. Consequently, the Marangoni-driven convection made its asymmetrical, and the molten metal flow pattern returned to a state like that in Fig. 3.13 (a), characterized by stronger flow toward the cast-iron side and an asymmetric vortex structure.

This cyclic evolution of the flow is from asymmetric to symmetric and back to asymmetric reflects the strong coupling between thermal gradients, surface tension forces, and transient mixing induced by molten droplet transfer. The results highlighted that the instantaneous thermal and flow field disturbances introduced by the molten droplet play a crucial role in determining keyhole stability and the distribution of nickel-alloy in dissimilar metal welding.

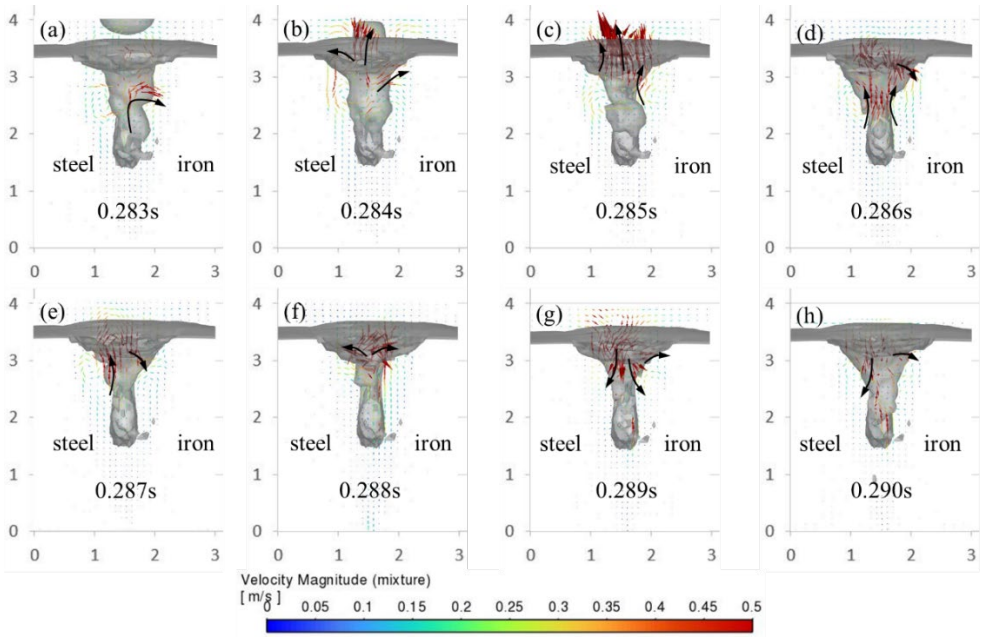


Fig. 3.13. Velocity distribution at keyhole position at transverse cross-section.

3.4.6. Materials volume fraction

Fig. 3.14 showed the evolution of the three-metal distribution near the keyhole from 0.06 s to 0.48 s during laser welding. Since this section remained at the keyhole position, the welding time corresponded only to different spatial locations along the weld path, rather than real-time changes at a single point. Therefore, the following analysis reflected spatial variations in steady-state welding conditions.

At the early stage, melting occurred mainly along the interface between carbon steel and cast-iron, forming a narrow molten layer at the bottom of groove. As laser moved forward, the molten pool expanded and keyhole formed, the interfacial mixing between the two base metals became stronger under strong Marangoni convection. Throughout the process, only a small portion of the nickel-alloy filler participates in mixing and remains concentrated near the upper pool region, indicating limited diffusion compared with the Fe-based metals at keyhole position.

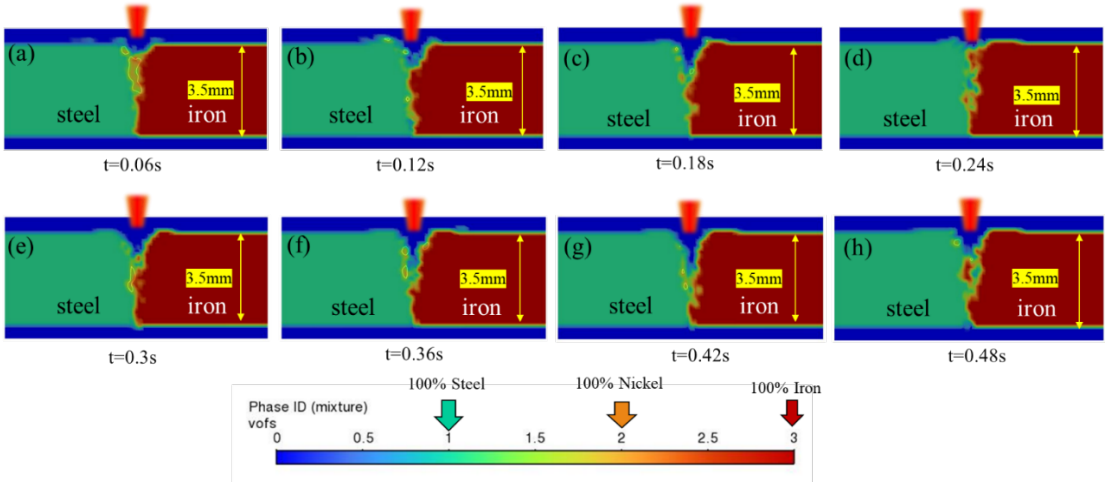


Fig. 3.14. Evolution of keyhole shape and material distribution at the laser position.

Fig. 3.15 illustrated the longitudinal distribution of the nickel-alloy at different concentration levels. The region before the yellow dashed line corresponded to the solidified zone, where the molten metal has completely solidified and no further flow occurred, as confirmed by the final solid–liquid interface shown in Fig. 3.15 (h). The results indicated that the nickel-alloy is primarily concentrated in the upper half of the molten pool, where the flow intensity is strong and the influence of the keyhole and surface convection is most referred.

Quantitatively, more than 70% of the total nickel-alloy volume fraction distributed within the upper 2.5 mm of the molten pool, while less than 10% remained below the mid-depth region. The local volume fraction of nickel-alloy in the upper molten zone reached approximately 0.35~0.45, compared with only 0.05~0.15 near the pool bottom. This gradient demonstrated the strong upward transport of nickel-alloy driven by Marangoni convection and recoil-pressure-induced circulation near the keyhole. As the molten pool began to solidify, these flow paths gradually blocked, and the nickel-alloy distribution became fixed. No continuous region with 100% nickel-alloy composition is observed, confirming that the filler material has been thoroughly mixed with the base metals. The resulting interfacial zone showed a smooth transition in composition rather than sharp phase separation. This mixed layer, with an average nickel-alloy content of about 20~25%, served as a metallurgical bridge between

carbon steel and cast-iron, improving interfacial bonding while minimizing compositional segregation in the final joint. Overall, the nickel-alloy exhibited a gradient distribution along the vertical direction, with higher concentrations in the upper molten region and lower concentrations toward the bottom. This pattern results from the combined effects of surface-driven flow, keyhole dynamics, and progressive solidification. The final composition field suggested that the nickel-alloy effectively enhances the metallurgical bonding between carbon steel and cast-iron by forming a uniformly mixed interfacial zone.

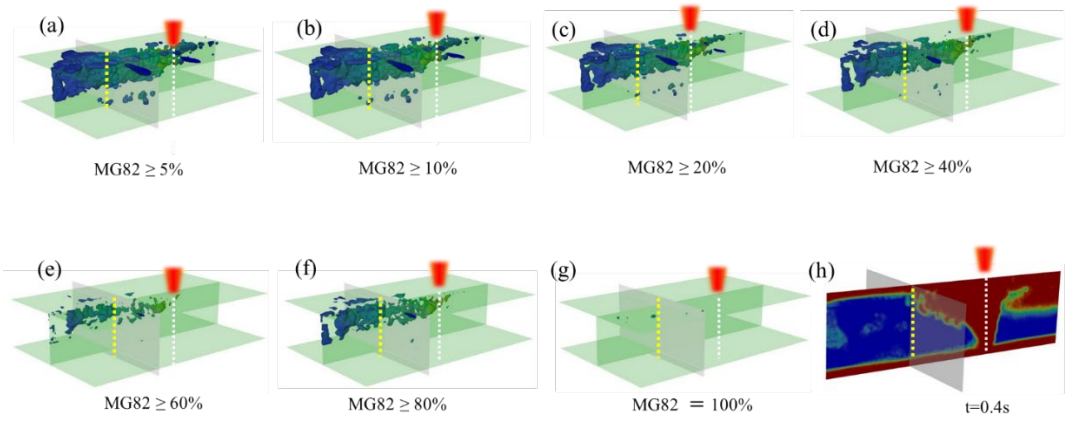


Fig. 3.15. Longitudinal distribution of the nickel-alloy at different concentration levels from 5%~100%.

Fig. 3.16 showed the simulated prediction in the distributions of nickel-alloy within transverse cross-section of the molten pool. The results exhibited a similar pattern, with nickel-alloy predominantly concentrated in the upper half of the fusion zone and a gradual decrease in concentration toward the bottom.

The simulation results indicated that approximately 65~75% of the total nickel-alloy volume fraction distributed within the upper 60% of the molten pool height, while less is found below mid-depth. This distribution is due to the combined effects of Marangoni convection, recoil-pressure-driven upward flow near the keyhole front, and the solidification sequence that causes nickel-alloy to remain in the last-solidifying regions near the surface.

At higher laser power and shallower focus positions, simulation results showed a wider spread of nickel-alloy across the pool surface, whereas deeper focus or lower power results in more localized Ni enrichment. These findings suggested that the molten pool flow pattern and keyhole depth directly influence the extent of nickel-alloy dispersion, and optimizing laser power and focal position can improve the homogeneity of filler metal distribution.

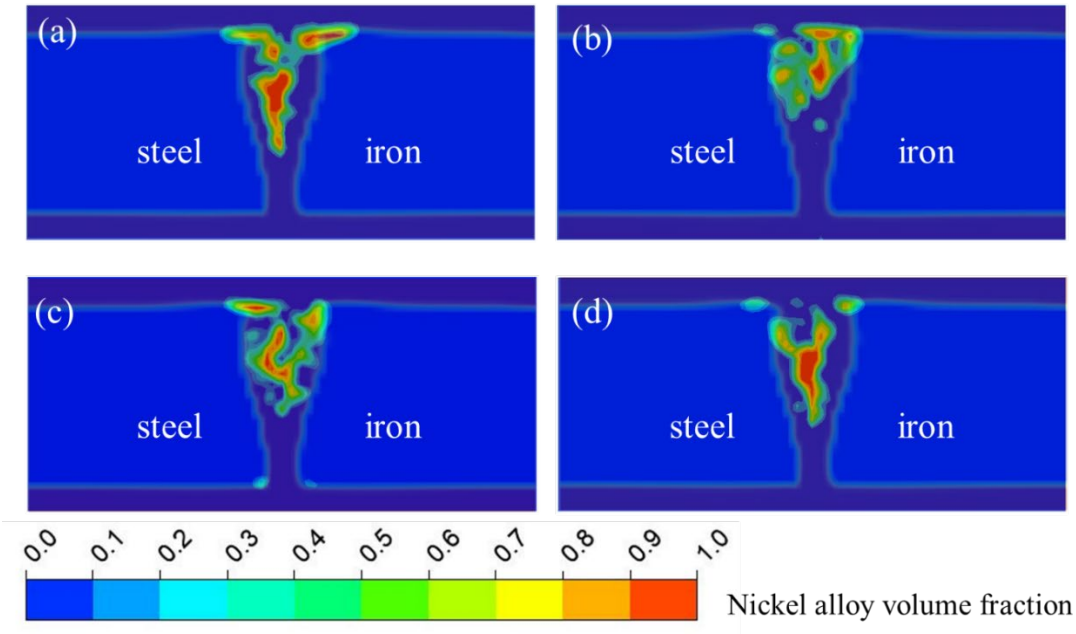


Fig. 3.16. Similar distribution of nickel-alloy at different transverse cross sections.

3.5. Summary

A three-dimensional CFD model was developed to simulate dissimilar keyhole laser welding of carbon steel and cast-iron with a nickel-alloy filler wire. The model successfully captured the main physical phenomena including molten droplet transfer, molten pool morphology, temperature field and nickel-alloy distribution in the molten pool. The conclusions are summarized as follows:

(1) The keyhole exhibited periodic opening and collapse behavior due to the dynamic balance between recoil pressure and surface tension. During collapse,

transient gas bubbles are generated but subsequently released through buoyancy-driven motion.

(2) The asymmetric flow pattern in molten pool due to laser welding dissimilar materials is dominant. When molten wire droplets transferred into molten pool with keyholes, the flow pattern and local temperature field changed significantly. It temporarily reduced the temperature gradient and Marangoni-driven asymmetric flow. With the progress of the mixing of molten wire droplets with two dissimilar base metals, the asymmetric flow pattern reappeared.

(3) The nickel-alloy is primarily distributed in the upper half region of the molten pool, and its volume fraction is around 65%~75%. The nickel-alloy filler metal is well mixed with the base metals of cast-iron and carbon steel, forming a graded transition layer with 20~25% nickel-alloy content that enhanced metallurgical bonding and compositional uniformity in the welded metal.

Chapter 4. Finite Element Modelling for Asymmetric Molten Shape in Laser Welding Dissimilar Materials

4.1. Introduction

Molten pool morphology in dissimilar metals welding is different from that in same metal and influenced by the position of the welding wire, which concerns the welding crack occurrence. In this study, a newly designed ring gear and differential case of electric vehicles whose materials are carbon steel and cast-iron, respectively, was welded by laser beam. The nickel-based alloy was used as welding wire. The location of welding wire in transverse direction can result in an asymmetric shape of the molten zone defined by the wire offset position “e” and form a “golf club-like” molten pool, which is clearly observed in experiments. A novel hybrid heat source model consists of a Cylinder heat source model, and a Goldak heat source model is developed in numerical calculation. The value “es” defined the offset distance between the center of heat source and seam of base metal as eccentricity to simulate heat flux that changed with the welding wire position. The results predicted a well asymmetric molten pool shape which is consistent with the experiment when “e” changed from -0.4mm to 0.2mm. And the predicted cooling rate in the metal surface is about 1200 ℃/s, which consistent with the experimentally measured value. This study can be guidance for understanding the morphology of molten zone and temperature field at different welding wire positions.

4.2. Materials and offset positions of filler wire

The investigation continues to focus on the same dissimilar-material differential unit used throughout this study, consisting of carbon steel, Cr–Mn steel, and FCD600-equivalent cast-iron joined with MG82 filler wire. Although the material system remains identical to the previous chapter, the emphasis of the present section

shifts toward examining how the lateral positioning of the filler wire influences molten-pool formation during laser welding.

Fig. 4.1 illustrates the experimental configuration of the Yb:YAG laser welding system and the geometric definition of the wire-offset parameter e. During welding, the laser beam is incident vertically while the filler wire is fed obliquely toward the beam interaction point, as shown in Fig. 1(a). The relative position between the wire and the laser beam is expressed by the transverse eccentricity “e”, defined in Fig. 1(b). When e = 0, the wire is aligned exactly along the joint centerline between the two base metals. A negative offset (e < 0) indicates movement toward the carbon steel side, whereas a positive offset (e > 0) shifts the feeding position toward the cast-iron side. In the experimental program, “e” was varied systematically within ±0.2 mm, enabling a controlled investigation of how wire placement affects the heat distribution and initial molten-pool geometry.

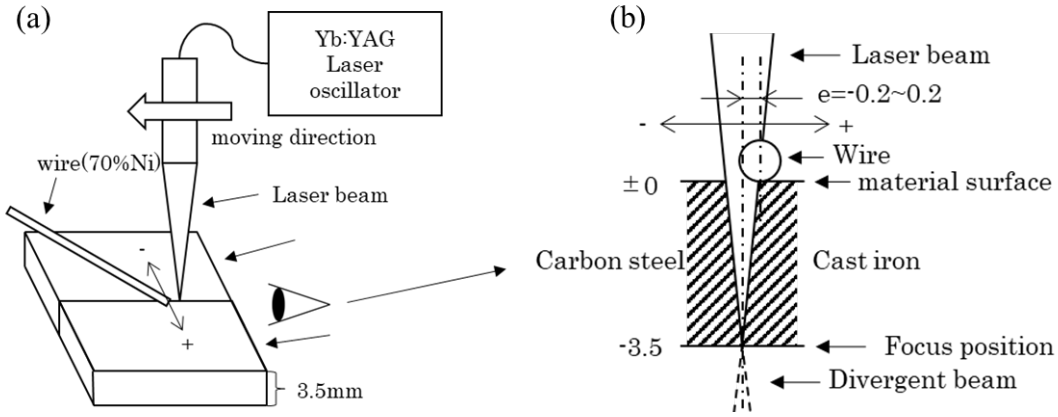


Fig. 4.1. Experiment setup and local geometry of welding groove (a) experiment setup arrangement, (b) cross-section view of laser and wire position.

4.3.Efficient numerical modeling

4.3.1 Geometry and meshing

The thermal process simulation for laser welding was performed by the in-house research software JWRIAN [118,119]. To improve calculation efficiency, a half circular construction was built as a geometry model, and meshing model is shown in

Fig. 4.2. The geometry model absolutely complied with the actual size of the production. The model was meshed with an 8-noded fully integrated hexahedral solid element. To balance both computational accuracy and efficiency, different grid sizes are used for different regions of the model. The finest meshing size on the transverse section was 0.1 mm in the melting zone. For heat affected zone, the meshing size was between 0.1 mm and 0.2 mm. It was enlarged to 0.5 mm out of heat affected zone. At circumferential direction and the diameter of laser heat source, the meshing size was assigned as 1 mm considered the laser moving velocity. There are 293,401 nodes and 277,920 elements contained in the meshing model.

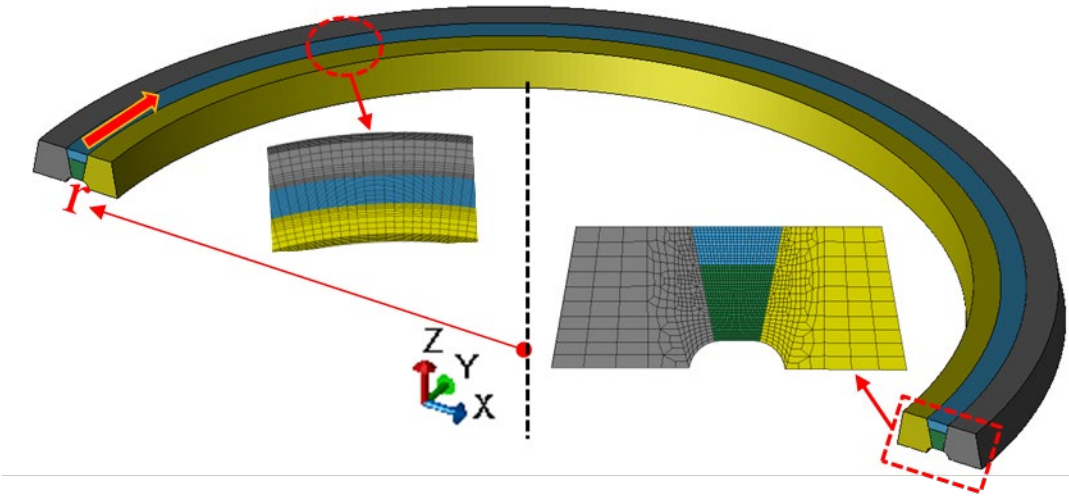


Fig. 4.2. Geometry and meshing of calculation model.

4.3.2 Equivalent laser heat source model

In the experiment, a portion of the laser irradiated onto the welding wire, causing part of the laser energy to be absorbed by the welding wire, thereby melting the wire. This will result in a change in the heat distribution within the molten zone area. The hybrid heat source model is regarded as intact that all the power is produced by laser beam, however, for actual condition, the wire blocks part of the laser beam, only the rest of the laser beam will irradiate onto the base metal directly, so the hybrid heat source is composed of the heat generated by the rest of the laser beam and wire

droplets. A cylindrical heat source with Gaussian heat distribution in radius direction shown in Fig. 4.3 (a), corresponded with the Goldak heat source with Gaussian heat distribution in radius and thickness directions shown in Fig. 4.3 (b) expressed equivalent heat source of laser beam under the influence of wire droplets, which can be described by the following formular respectively:

$$q_c = \eta P \frac{6\sqrt{3}}{\pi\sqrt{\pi} r^2 d} \exp\left[-\left(\frac{3x^2+3y^2}{r^2}\right)\right] \quad \text{Eq.4.1}$$

$$q_f = \eta P \frac{6\sqrt{3}F_f}{\pi\sqrt{\pi} a_f bc} \exp\left[-\left(\frac{3x^2}{{a_f}^2} + \frac{3y^2}{b^2} + \frac{3z^2}{d^2}\right)\right] \quad \text{Eq.4.2}$$

$$q_r = \eta P \frac{6\sqrt{3}F_r}{\pi\sqrt{\pi} a_r bd} \exp\left[-\left(\frac{3x^2}{{a_r}^2} + \frac{3y^2}{b^2} + \frac{3z^2}{d^2}\right)\right] \quad \text{Eq.4.3}$$

where q_c, q_f, q_r denotes the power density distributions of cylinder heat source, the front and rear ellipsoids in Goldak heat source respectively, q_e is composed by q_f and q_r in Fig. 4.3 (b). η indicates the heat efficiency, *P* represents the laser power, "r" and "c" express the radius and depth of the heat source respectively for cylindrical heat source model, in Goldak heat source model a_f, a_r and b represent the length of the front quarter ellipsoid, the length of the rear quarter ellipsoid and the maximum width of the total ellipsoid. F_f and F_r denotes the fraction of heat deposited at front and rear ellipsoid, respectively. The x, y and z coordinates are those in the welding coordinate system in which the origin is moving with the welding laser beam. The position of the welding wire will also affect the location where the laser is directly irradiated onto the base metal. The location of the effective laser irradiation onto the base metal is described by the effective laser center. In this calculation, the power P generated by laser beam was 2510 W, the effective heat source radius of droplets r was 0.4 mm. For Goldak heat source model a_f equals to b was 1.1 mm, a_r was 3 mm and the depth d for heat source was 1.4 mm.

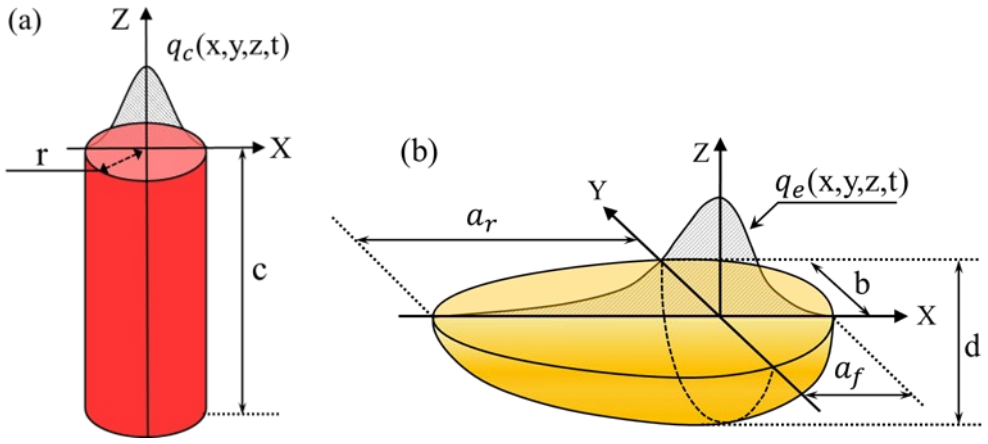
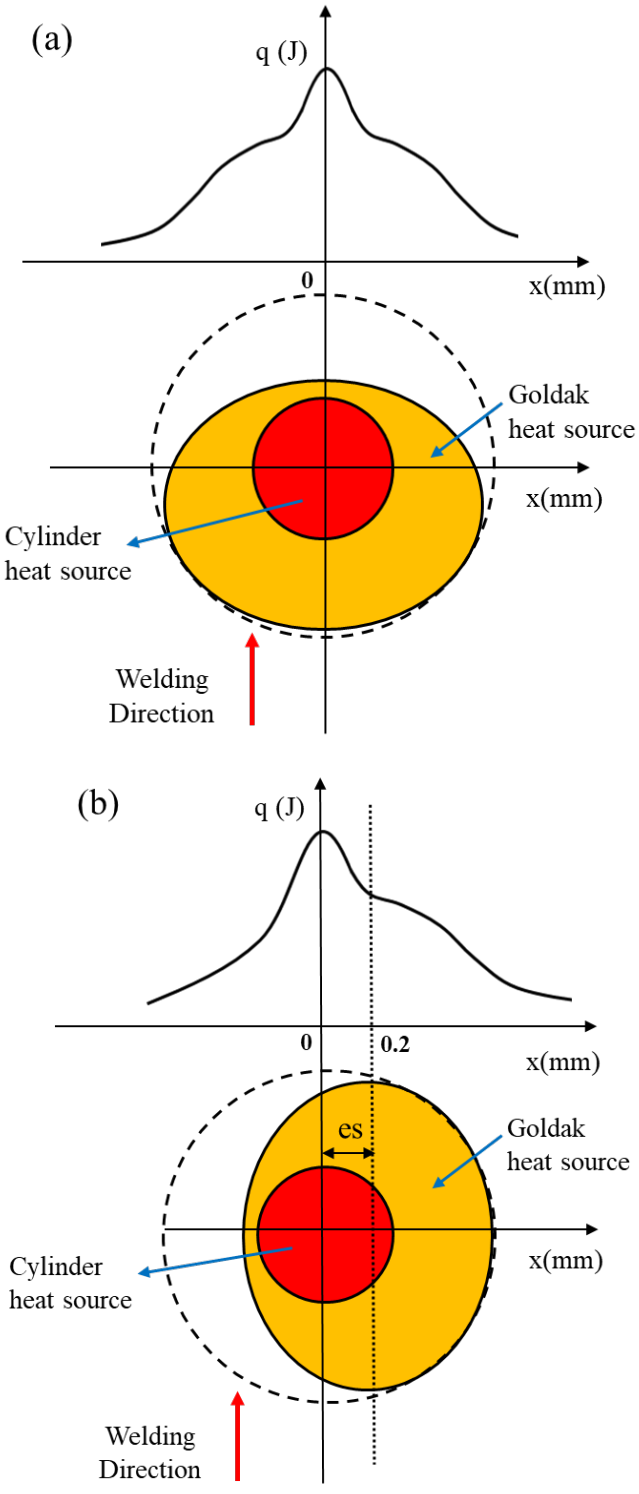


Fig. 4.3. The equivalent heat source model (a) Cylinder heat source model, (b) Goldak heat source model.

The relative position of the laser beam and wire feeding position shown in Fig.5. In the figure, q stands for heat generated by the laser beam. The distance between the laser center and the seam of two base metal described as “es” which distinguished with wire deviated value e. When the welding wire was just right in front of the laser beam, the laser beam was not blocked by the wire, under this condition the heat distribution at transverse direction complied with standard Gaussian distribution, the heat magnitude reached to the peak value at the center of the laser beam position Fig. 4.4 (a). When the welding wire position deviated towards the cast-iron side, at transvers direction, the welding wire blocked part of laser beam at cast-iron side, causing it to melt into molten droplets. The heat used to melt the welding wire, carried by molten droplets, brought into the molten zone. Thus, the heat distribution at transverse direction also has deviation, the peak heat value position translational move to carbon steel side, which irradiated by laser beam directly as shown in Fig. 4.4 (b). When the welding wire position deviated to the carbon steel, the phenomenon was completely opposite as shown in Fig. 4.4 (c).


(a)
q (J)
0
x(mm)
Goldak
heat source
x(mm)
Cylinder
heat source
Welding
Direction
(b)
q (J)
0
0.2
x(mm)
es
Goldak
heat source
x(mm)
Cylinder
heat source
Welding
Direction

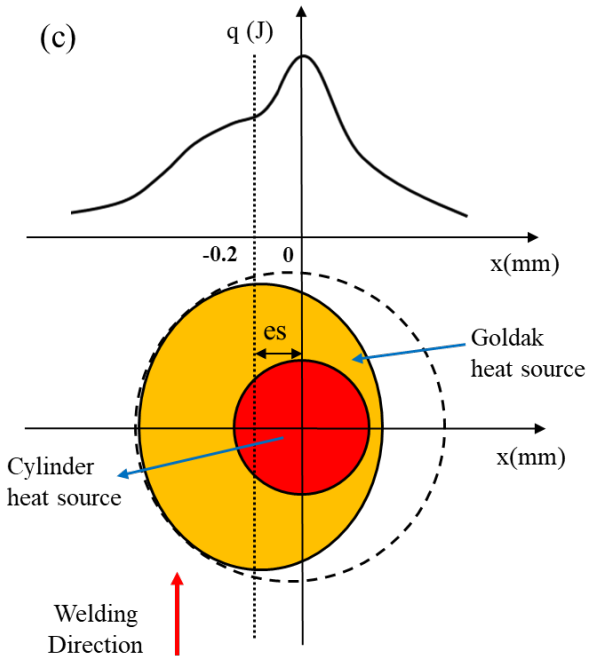
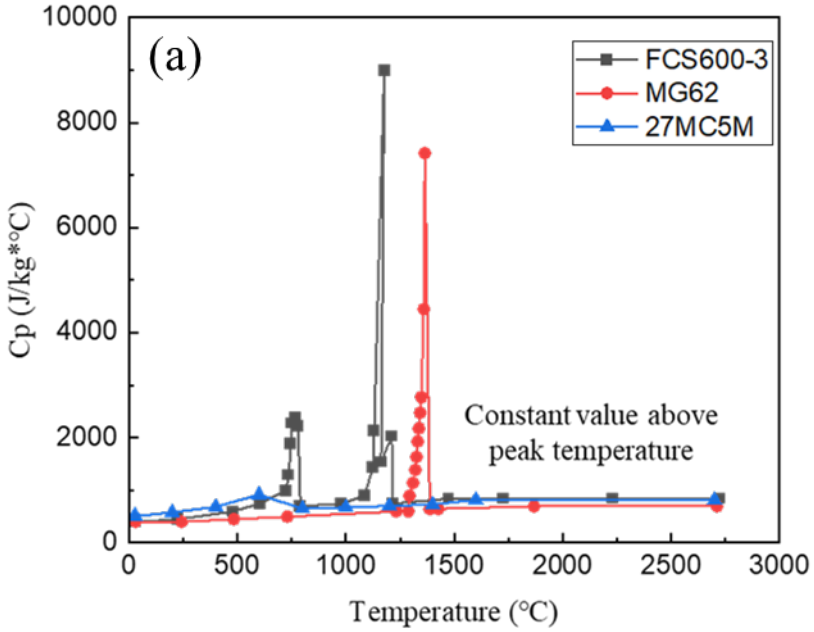
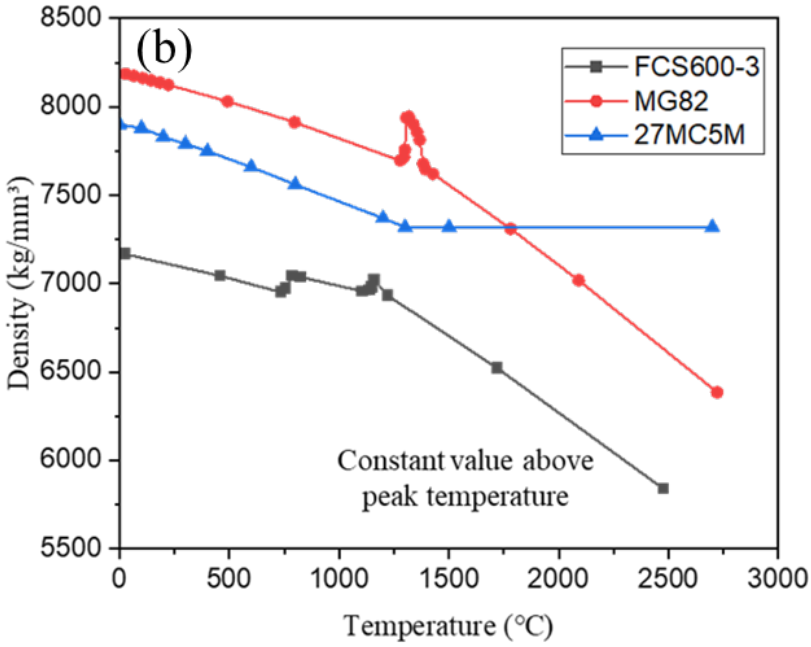


Fig. 4.4. The description of eccentric heat source composition (a) Wire position with no deviation ($es = 0mm$), (b) Wire position deviates to carbon steel ($es = 0.2mm$), (c) Wire position deviates to cast-iron ($es = -0.2mm$).

4.3.3 Modelling for thermal boundaries

To obtain high accuracy simulation on the molten zone and temperature field, the material thermal properties of the three types of metals were measured. The specific heat, density and thermal conductivity measured at different temperatures are shown in Fig. 4.5. Since the thermophysical properties of the three metals are not in a great difference, and the molten pool will be filled with the welding wire metal, it is assumed in the calculations that the thermophysical properties of the metal in the molten pool region are equivalent to those of the welding wire metal. Based on actual experimental conditions, the heat exchange area is divided into two parts, top surface and side surfaces cooled with and without shield gas, respectively. Therefore, the equivalent heat transfer coefficient used in the thermal analysis is larger on the top surface and smaller on the side surfaces, as shown in Fig. 4.6.


(a)
FCS600-3
MG62
27MC5M
Constant value above
peak temperature
Cp (J/kg*°C)
Temperature (°C)
0
2000
4000
6000
8000
10000
0
500
1000
1500
2000
2500
3000


(b)
FCS600-3
MG82
27MC5M
Constant value above
peak temperature
Density (kg/mm³)
Temperature (°C)
5500
6000
6500
7000
7500
8000
8500
0
500
1000
1500
2000
2500
3000

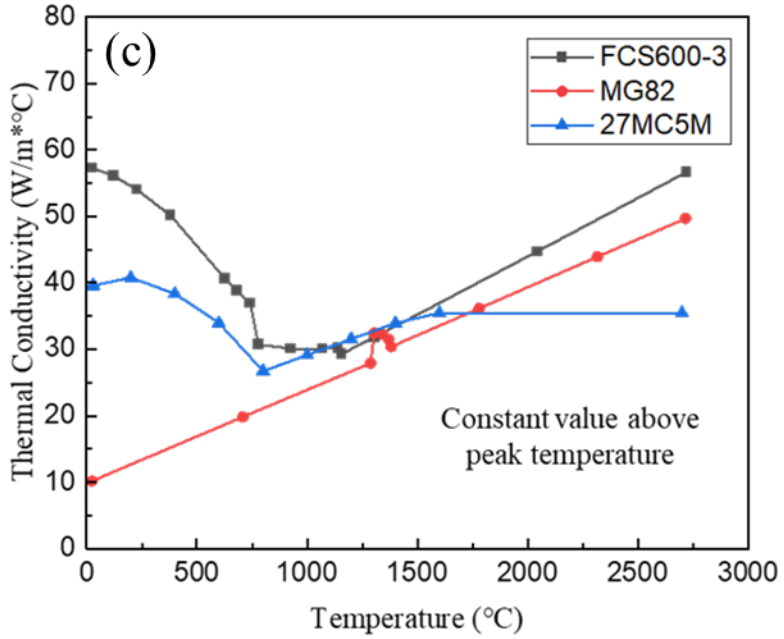


Fig. 4.5. Material properties of three materials (a) Specific heats of three materials, (b) Density of three materials, (c) Thermal conductivity of three materials.

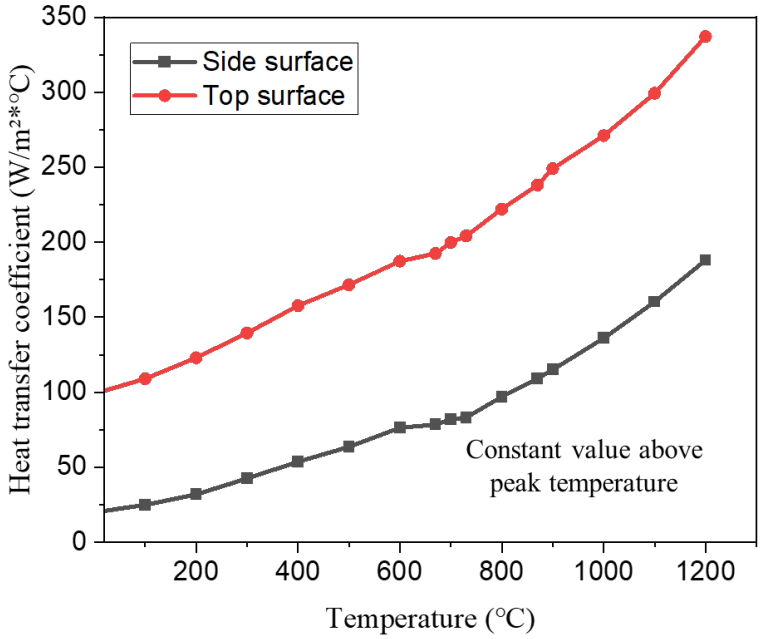


Fig. 4.6. Convection heat transfer coefficient at different surfaces.

4.4.Results and discussions

4.4.1 Temperature history and validation with experiment

In the experiment, the total welding time was about 14 seconds for welding angles of 180°. In the evaluation of the molten zone and temperature field, the stable zone in the welding direction was focused. The measured temperature distribution along the welding trail direction of the molten zone by thermal graph is shown in Fig .4.7. A total of 3 equidistant points is selected for quantitively evaluation and the time 0.0 is defined to correspond to laser beam position, the distance from point A, B and C corresponded the welding time about 0.5 seconds.

Fig. 4.7 (b) shows the comparation curve between experiment value and simulation result. The points same as the experiment are also selected for comparison. Exp point represents the point selected from experiment and Sim point means the point obtained from simulation results. The measured peak temperature at the point near the laser beam are between 1200 ℃ and 1400 ℃. After about 0.5 seconds when the laser moved away from the evaluation point, the temperature decreased to 700 ℃ gradually.

The peak temperature of the points in simulation is also between 1200 ℃ and 1400 ℃, which is almost the same as experiment result. The temperatures after about 0.5 seconds are between 600 ℃ and 650 ℃, which are about 10% lower than the experiment result. The tendency of the cooling rate is the same in both experiment and calculation results. As a summary, the calculated temperature changes at cooling process agreed with the experimental results.

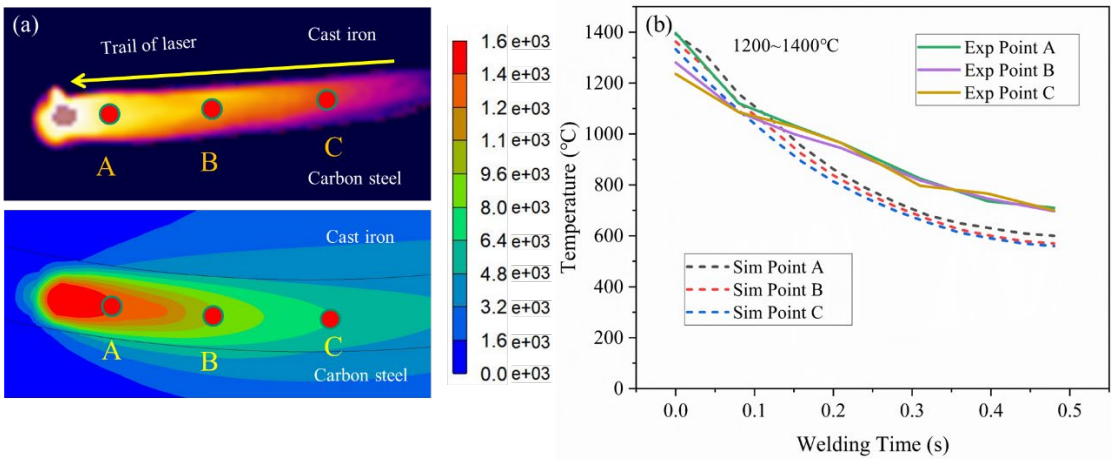


Fig. 4.7. Experimental and simulated curves comparing surface heat dissipation (a) Comparation of temperature field map, (b) Comparing temperature curves.

4.4.2 Temperature distribution of molten zone and heat affected zone

Fig. 4.8 shows the peak temperature distribution from the top view. The width of heat affected zone is almost constant from the section of the 20-degree in the welding direction. Thus, the section at the 90-degree is extracted and its peak temperature distribution is shown in Fig. 4.8 for evaluation. The blue line in Fig .4.9 (a) indicated the fusion line of cast-iron side and 4 points selected from the center line of molten zone based on the molten area with unique shape characters and passing through the whole molten area in depth direction. So, the position located at the upper, middle, and bottom positions are selected to show the temperature field at the molten shape sudden changing area which has greater cracking probability and the whole molten zone. Fig. 4.9 (b) shows the temperature history at the middle position of molten zone from node 1 to node 4. It can be observed from the plot, the temperature of the center of molten zone is between 1400 ℃ and 2200 ℃. The peak temperature is at the upper side of the molten zone which is shown by node 1. Most of the laser power is concentrated on the upper side and made the temperature rise rapidly. The cooling rate at first 0.5 second is fast until the temperature decreased to 500 ℃. When the temperature became lower than 200 ℃, all evaluation points had the same temperature and then cooled down to room temperature.

Fig. 4.9 (c) shows the temperature history of fusion line at iron side which is from node 5 to node 8. The plot shows the temperature of the fusion line is around 1200 ℃ and 1400 ℃. The peak temperature at the upper side is shown by node 1. The cooling rate is almost the same for each evaluation point, the temperature stabilized to about 180 ℃ after 6.6 s.

Based on the calculated temperature history of molten zone center and fusion line position, the cooling rate has little difference in the depth direction of molten zone, which is mainly influenced by thermal conductivity. When the laser heated the base metal, the temperature rapidly rises to the melting point, fully melting the base metal.

Because only heat conduction is fast within the molten zone, the cooling rate at different positions within the molten zone is essentially uniform. Due to the significant temperature difference between the molten zone and room temperature, the cooling of the molten zone is very fast at high temperature. When the temperature reached to the lower temperature range between 250 ℃ to 300 ℃, it followed the cooling rate at all positions of the fusion line is almost the same and then uniformly cooled down to the room temperature.

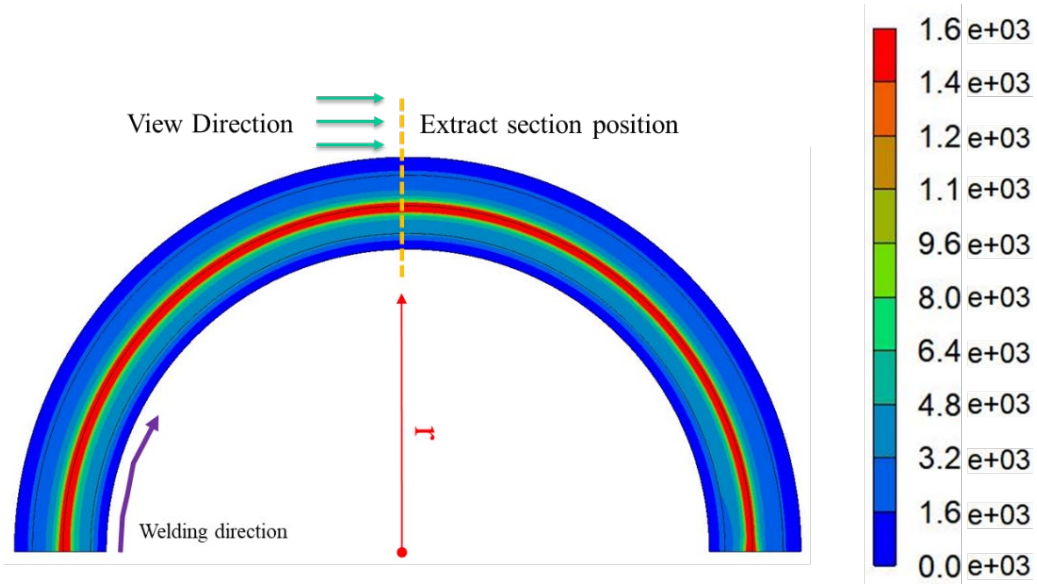
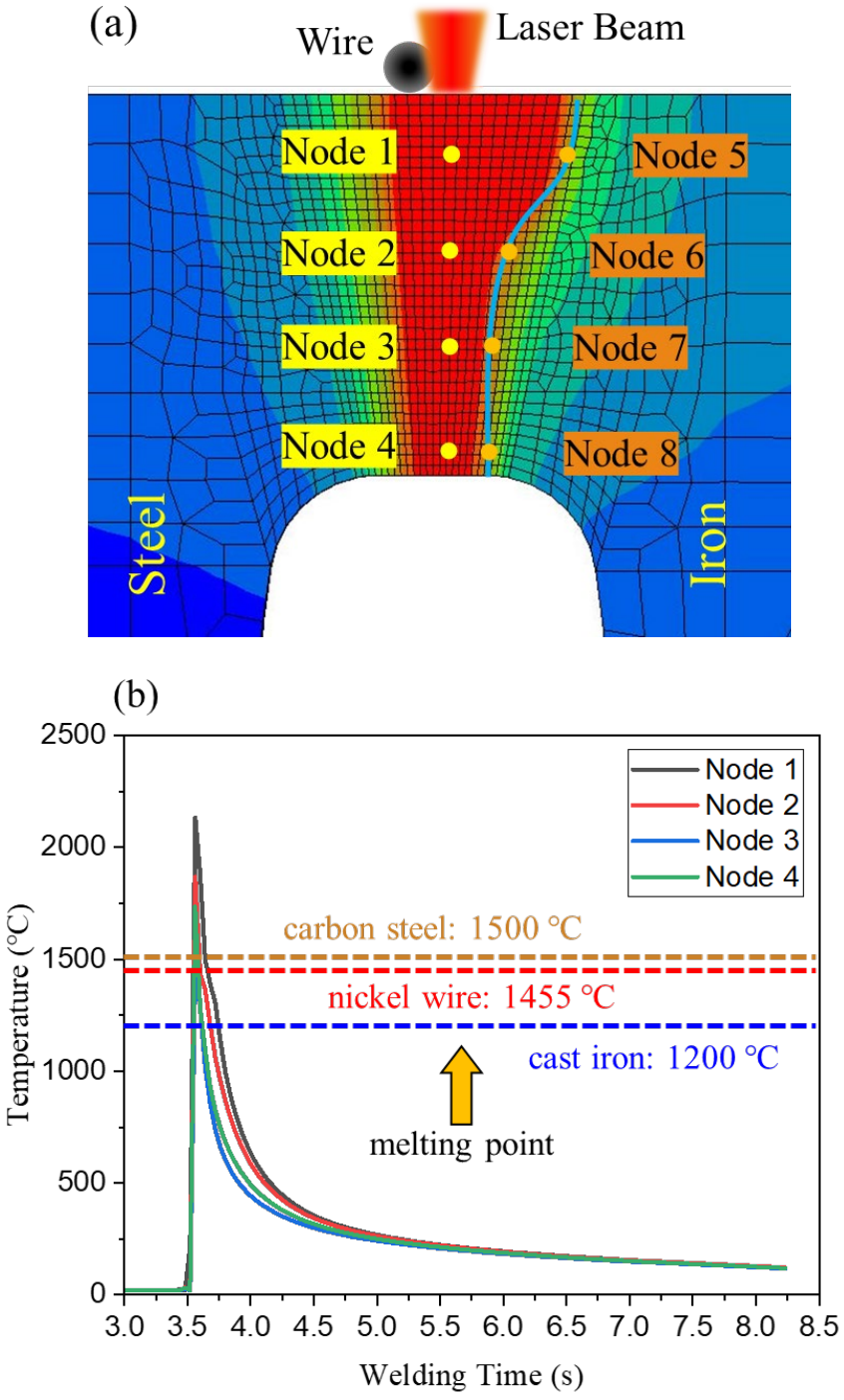


Fig. 4.8. Macroscopic overview of temperature distribution.


(a)
Wire
Laser Beam
Node 1
Node 2
Node 3
Node 4
Node 5
Node 6
Node 7
Node 8
Steel
Iron
(b)
Temperature (°C)
Welding Time (s)
Node 1
Node 2
Node 3
Node 4
carbon steel: 1500 °C
nickel wire: 1455 °C
cast iron: 1200 °C
melting point

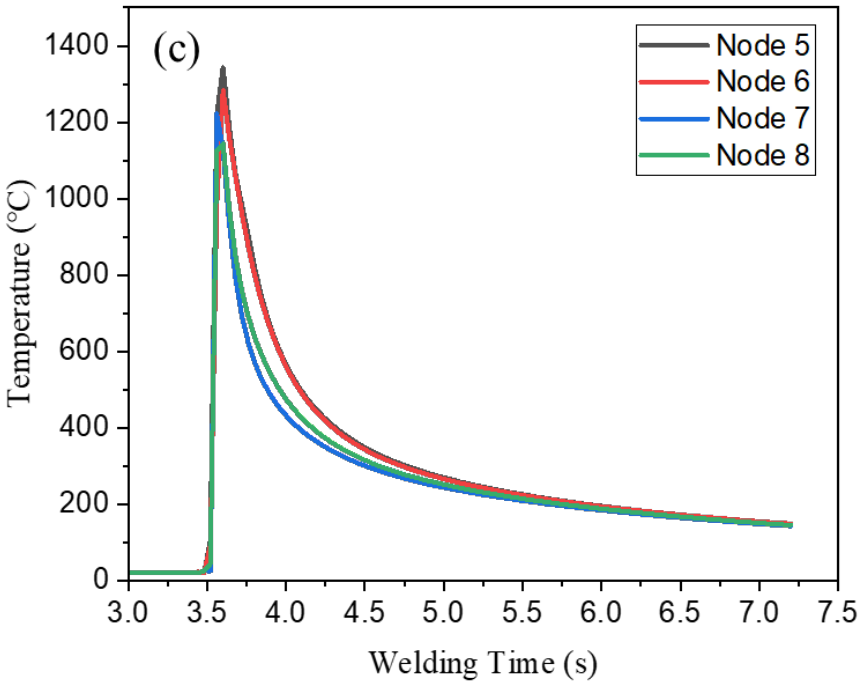


Fig. 4.9. Temperature history curve of molten zone (a) Instruction of evaluation point position, (b) Temperature history curve of molten zone center, (c) Temperature history curve of iron side heat affected zone.

Fig. 4.10 shows comparison between the experimental and simulated molten pool shape when the welding wire is on the cast-iron side, in the middle position and on the carbon steel side, respectively. From the figure, it can be observed that the molten zone has an asymmetric shape which looks like a “golf club.” Because the laser energy is absorbed by cold welding wire, the melt width on the welding wire feed side is significantly smaller than that on the opposite side. Based on the applied hybrid heat source, the molten zone shape of the three cases in the simulation results closely matches the actual melt shape observed in the experiment, which verified the feasibility of the hybrid heat source.

Figs. 4.10 (a), (b) and (c) also show the distribution of the peak temperature reached in the laser welding induced temperature history, when the welding wire feed position is located at the steel side, in the middle and iron side, respectively. All sides

of the base metal are melted, demonstrating an effective joining situation among three metals of high carbon steel, casting iron and Nickel welding wire.

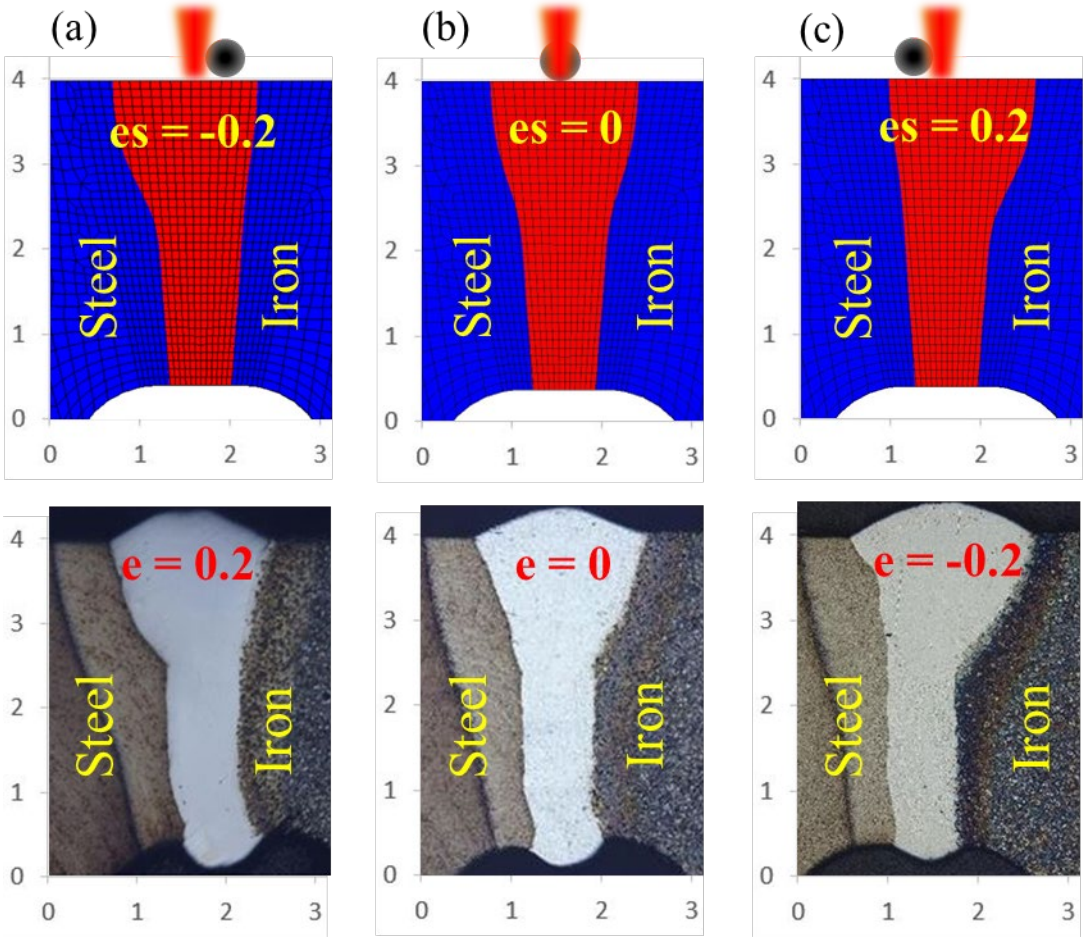


Fig. 4.10. Experimental and simulated comparison graph of molten zone shapes (a) Wire position deviates to cast-iron, (b) Wire position in the middle position (seam), (c) Wire position deviates to carbon steel.

Fig. 4.11 indicates the area dimension of the molten pool and heat affected zone. The green color in the figure expressed the heat affected zone in which the peak temperature is between 700 ℃ and 1200 ℃. It can be observed from Fig. 4.11 (a) that the width of the heat-affected zone on the cast-iron side is a little bit larger than that of carbon steel. When the welding wire feed position is located on the iron side, the width of heat affected zone on the steel side is slightly larger.

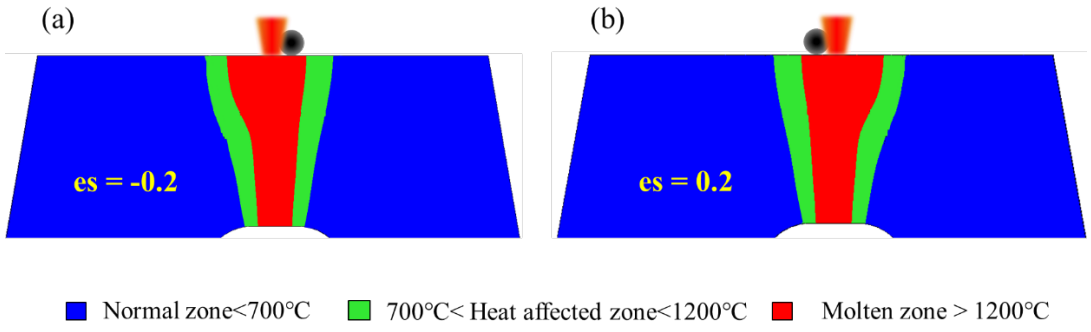


Fig. 4.11. Temperature field of heat affected zone and molten zone (a) Welding wire on steel side, (b) Welding wire on the iron side.

4.4.3 Molten zone shape and its size

Fig. 4.12 (a) shows the experimentally observed molten zone on the transverse section when the welding wire is at carbon steel side, and the width of the weld pool at the top position which is 2.02 mm as well as the depth of the welding pool which is 3.52 mm are measured. To verify the temperature distribution in the width direction of the welding zone and the specific size of the molten zone of simulation, temperature data are collected based on the molten zone shape with unique characteristics. So, in this model the top of the welding pool (Laser directly irradiation area), the location of the sudden change in cross-sectional area of the weld pool which has greater probability cracking, and the bottom of the weld pool (Area with minimum molten width in experiment) which is section 1, section 2, and section 3 respectively are selected, shown in Fig. 4.12 (b). The section contained the base metal area, heat affected zone and melting zone from carbon steel side to cast-iron side. The width from the seam of two base metals to fusion line are described as W1 (steel side) and W2 (iron side). The distance between the seam and the boundary line of heat affected zone are represented by WH1 (steel side) and WH2 (cast-iron side).

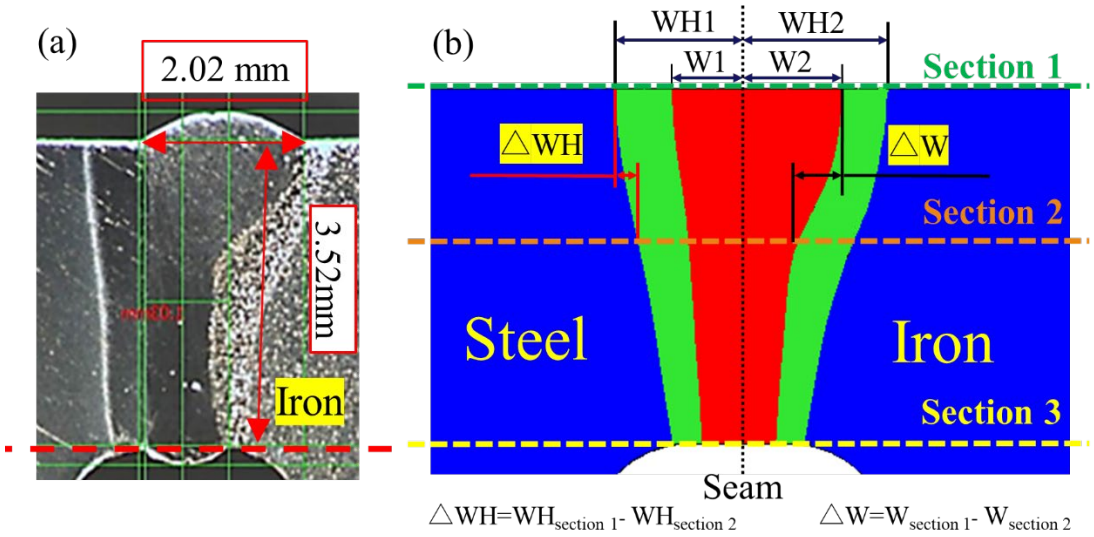
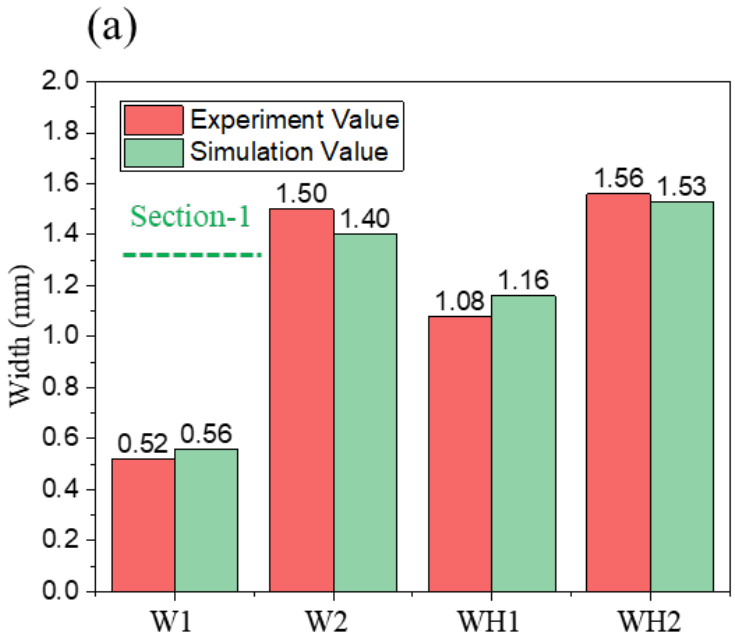
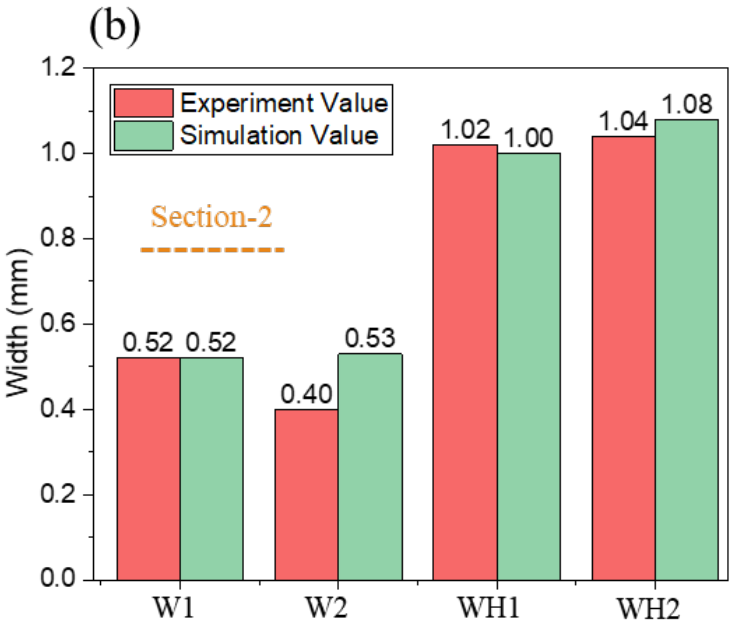


Fig. 4.12. Instructions for cross-sectional measurement position (a) Molten zone dimensions of experimental result, (b) Position instruction of simulation result.

When the temperature exceeds 1200 ℃ base metal begins to melt, and when the temperature exceeds 1400 ℃, the welding wire metal starts to melt into a liquid state. Based on the melting temperatures of the base metal and the welding wire, a temperature of 1200 degrees Celsius is chosen as the criterion for determining the size of the molten pool. The width dimensions of the weld pool are analyzed for the selected three cross-sections within molten temperature. Fig. 4.13 shows the comparation of the welding zone width between experiment value and simulation result at each selected section. Based on the lowest melting temperature of the three metals, the size of the welding zone at the top surface (section 1) is 0.96 mm (W1+W2) shown in Fig. 4.13 (a). Under the same criteria, the molten zone width of section 2 is 0.92 mm, and the width of section 3 is 0.88 mm shown in Fig. 4.13 (b) and (c) respectively. Fig. 4.13 (d) shows that the welding zone width difference of section 1 and 2 is greater at the iron side which is shown as W2 and WH2. The simulation data reveals that the size of the weld pool is essentially consistent with the experimental results, further confirming the effectiveness of this equivalent heat source model.


(a)
Experiment Value
Simulation Value
Section-1
Width (mm)
2.0
1.8
1.6
1.4
1.2
1.0
0.8
0.6
0.4
0.2
0.0
0.52
0.56
1.50
1.40
1.08
1.16
1.56
1.53
W1
W2
WH1
WH2


(b)
Experiment Value
Simulation Value
Section-2
Width (mm)
1.2
1.0
0.8
0.6
0.4
0.2
0.0
0.52
0.52
0.40
0.53
1.02
1.00
1.04
1.08
W1
W2
WH1
WH2

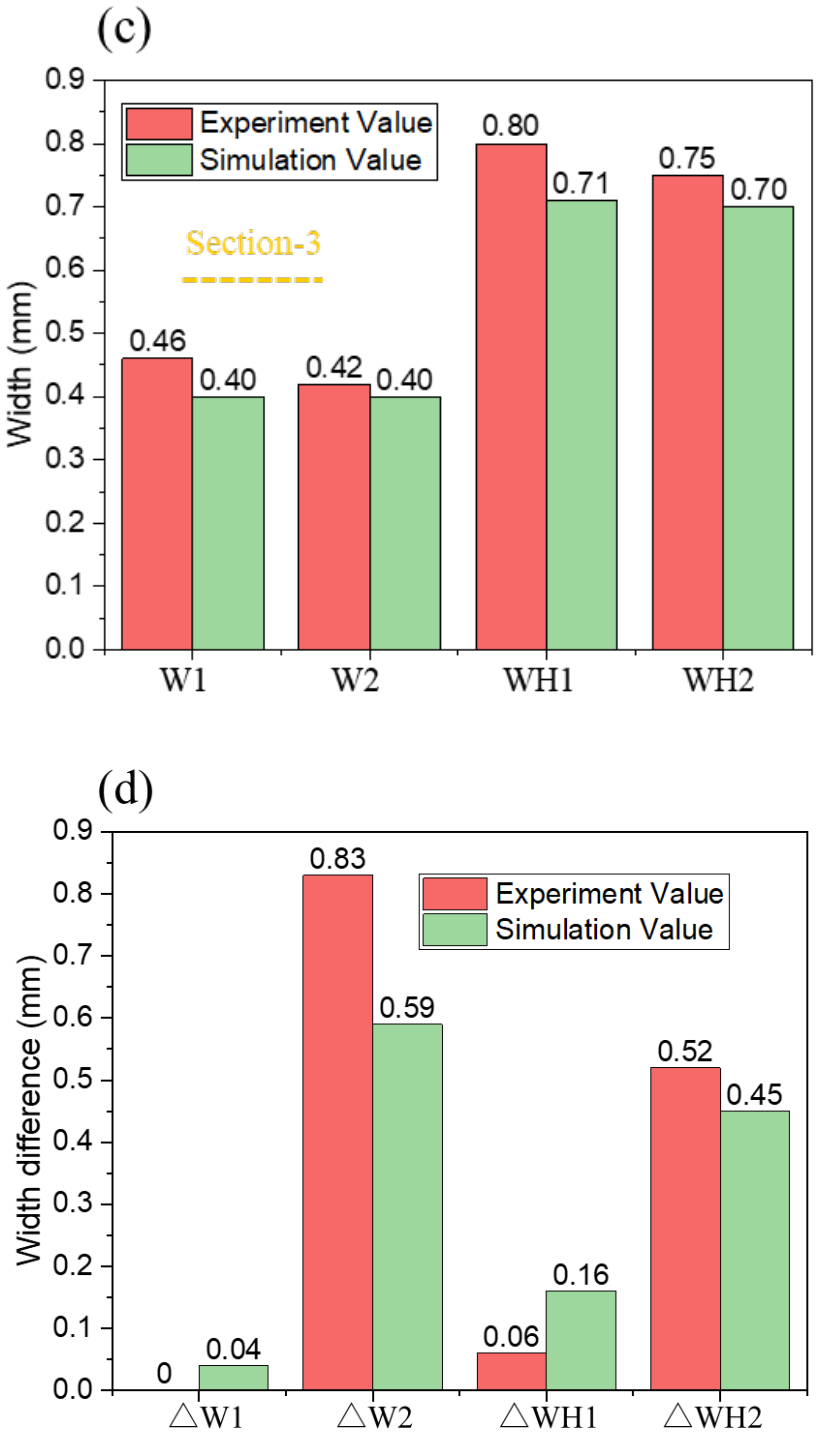


Fig. 4.13. Comparation of welding zone width size (a) Section 1, (b)Section 2, (c) Section 3, (d) Welding zone width difference of section 1 and section 2.

4.4.4 Influence of welding wire position on molten shape

It already demonstrated the consistency between the simulated results of the weld pool shape and the experimental results. To figure out the influence of the welding wire position on the shape of the molten zone under greater wire deviation value as well as the linear relationship of wire droplets center position and fusion line, the eccentricity parameter “es” for the equivalent heat source model is changed and several simulations are conducted. A total of nine cases of es varying from -0.8 mm to +0.8 mm are considered. Fig. 4.14 showed the temperature distribution and the molten zone shape on transverse cross section. The black lines in Fig. 4.14 are the meshing boundaries for different zones. When the value of es is between -0.2 mm to +0.2 mm, the simulated shape and size of molten zone are highly consistent with the experimental ones. The representative case that es equals to -0.2 mm, 0 mm, +0.2 mm was selected to investigate the relation shape between welding wire position and molten zone shape. When es equals -0.2 mm, the welding wire is at cast-iron side that absorbed part of the laser beam energy so that the laser directly irradiation area deviated to the carbon steel side, which made the molten zone on carbon steel side greater than that at cast-iron side. When the es equals +0.2 mm, the phenomenon is totally opposite. When the es equals to 0 mm, the welding wire is just ahead of laser beam along laser moving direction, thus, the laser beam is not blocked by the welding wire at transverse direction. At this condition, the molten zone presented almost symmetrical shape on both carbon steel side and cast-iron side. The welding wire position and molten zone shape, especially its asymmetricity, had a strong correlation when the es is between -0.4 mm to +0.4 mm. The sizes (W1, W2, WH1 and WH2) of the welding zone and heat affected zone of the nine simulation cases are comparably plotted in Fig.16. The figure summarizes the tendency of these sizes changing with different “e” values. When “e” value moves to positive position, the W1 and WH1 have an increasing tendency, oppositely, the W2 and WH2 show decreasing tendency. If looked at in detail, the size changing of molten zone and heat affected zone is

larger on the top surface and relatively smaller on section 2, as shown in Figs. 4.15 (a) and (b), respectively.

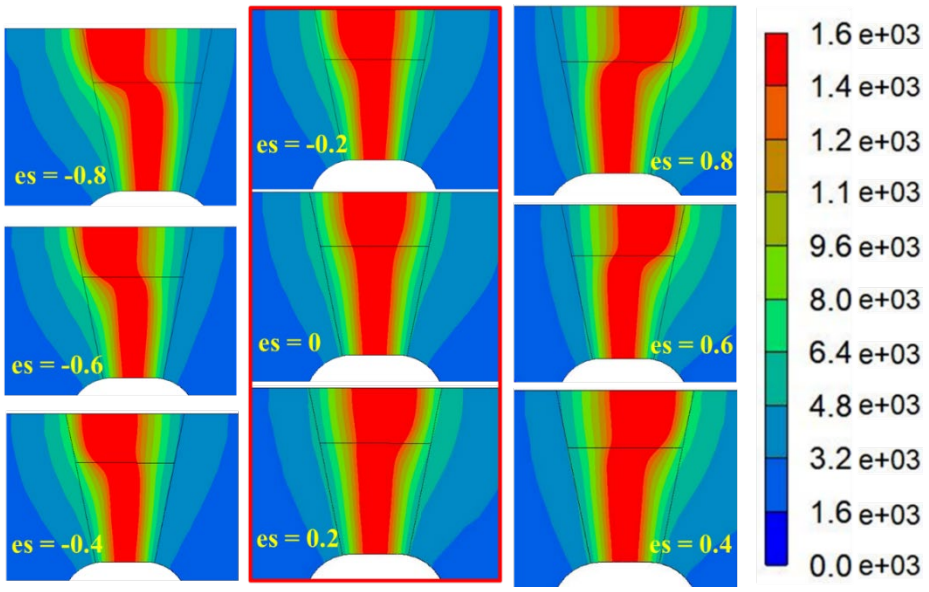
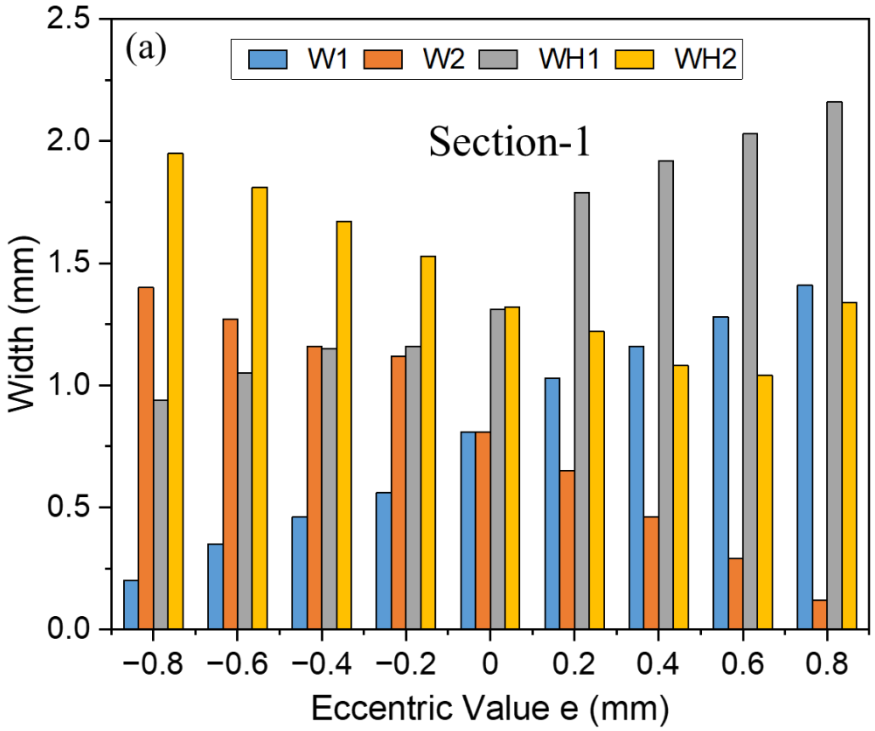


Fig. 4.14. Comparison of temperature distribution for different positions of welding wire.



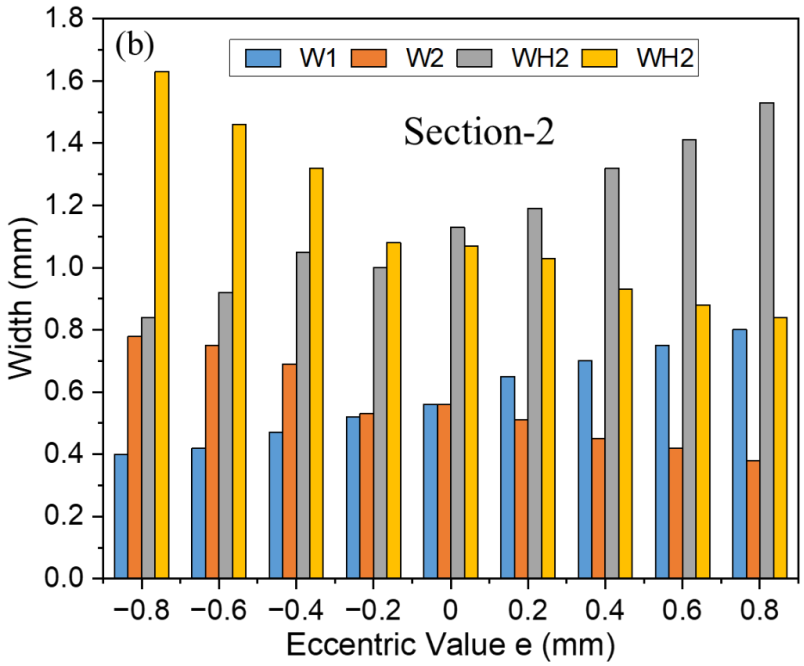


Fig. 4.15. Comparison of the width for the molten zone (a) The width of each part of welding zone W1,2 and WH1,2 of section 1, (b) The width of each part of welding zone W1,2 and WH1,2 of section 2.

As shown in Fig. 4.16, the corresponding relationship between welding wire position e and molten zone radius on iron side is evaluated and compared based on both experimental and simulated results. The red color zone in the figure represents the molten zone and the marked point by green color indicates the melting boundary on the cast-iron side at the top surface of the molten zone. Fig. 4.17 showed the fitting curve of the experimental radius Re and simulated radius Rs of molten zone at different e values of welding wire positions. When e equals to -0.2 mm, several experiment results showed the radius Re of molten zone is between about 55.3 mm to 55.4 mm, when the e value equals to 0 mm, the Re is around 55.1 mm and when the e equals to 0.2 mm, Re is between 54.5 mm and 54.6 mm. Based on the experiment result data, the relationship between Re and e is fit as a curve function:

$$Re = 1.234\, e + 55.106 \qquad \text{Eq.4.4}$$

Compared with the simulation result when e equals to -0.4 mm, -0.2 mm, 0 mm, and 0.2 mm, the values of Rs are within the range of Re. When the value of e exceeds

0.4 mm, there exists the deviation between Re and Rs. Based on the comparison, when the e value is between -0.4 mm and 0.2 mm, the simulation accuracy is remarkably high for practical prediction.

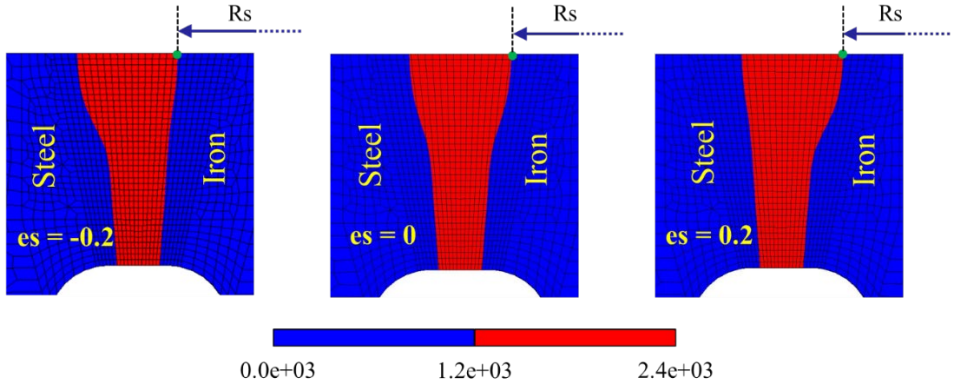


Fig. 4.16. Fusion line boundary of molten zone.

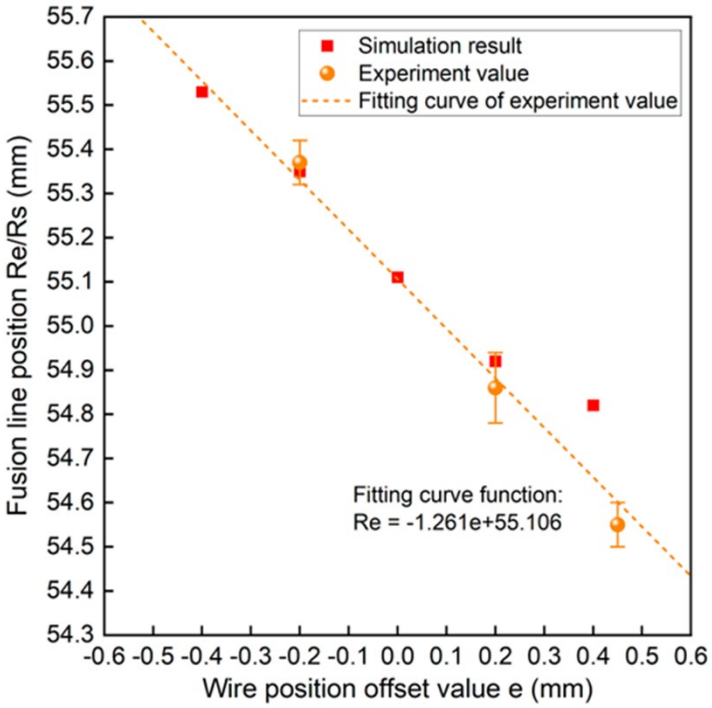


Fig. 4.17. Experimental and simulated comparison curves of the distance from the model's pivot center to the iron side welding line.

4.5. Summary

In this study, the carbon steel (Carbon content of 0.3%) and cast-iron (Carbon content of 3%) were welded by the nickel welding wire with laser beam. An equivalent hybrid heat source model was developed to predict the asymmetric molten zone shape and temperature distribution at different welding wire positions. The key conclusions are as follows:

(1) The developed hybrid heat source model predicted the thermal cycles, the asymmetric melting zone and its size changing with the weld wire offset positions.

(2) Both experiment and simulation results showed the width of melting zone becomes smaller at the side where the welding wire located, and molten zone presented a "golf club-like" shape.

(3) The heat transfer coefficient was defined as natural cooling and forced cooling at different surfaces. The top surface of based metal was assigned to forced cooling heat transfer coefficient because of the existence of shield gas. The calculated cooling rate at the top surface is about 1200℃/sec, which consisted with the experimentally measured value.

(4) The relationship between the welding wire position and the fusion line position is fitting well when e equals from -0.4mm to 0.2mm, which is quantified by the equation $y = -1.261x + 55.106$. The results can be guidance for understanding the shape formation of molten zone and temperature field at different offset positions of welding wire.

Chapter 5. Conclusions

This dissertation systematically investigated the thermal–fluid mechanisms, keyhole dynamics, and material mixing behaviors in keyhole-mode laser welding of carbon steel and cast iron, progressing from two-material interactions to a three-material system with Ni-based filler addition, and finally extending the numerical framework toward an engineering-oriented predictive model. The research first clarified fundamental molten-pool evolution and interfacial mixing between two dissimilar base metals; subsequently incorporated a nickel-alloy filler wire to reveal droplet–keyhole interaction, ternary mixing, and post-solidification distribution; and ultimately developed a fast and efficient hybrid heat-source model capable of predicting weld morphology under different wire-feed positions. Together, these components establish a comprehensive understanding of multi-material laser welding and provide modeling tools with both scientific and industrial value.

Chapter 2 focused on the baseline case of dissimilar welding without filler wire, aiming to uncover the intrinsic interaction mechanisms between carbon steel and cast iron under laser irradiation. A fully coupled 3D CFD model was established to capture transient keyhole oscillation, recoil-pressure-driven melt flow, asymmetric Marangoni convection, and the development of a dissimilar-material interface. The simulation accurately reproduced molten-pool shapes validated against experimental cross-sections, while thermal histories measured by infrared thermography confirmed the reliability of the equivalent heat-source model. The study revealed that the strong mismatch in thermophysical properties leads to inherently asymmetric molten-pool morphologies, localized vortices near the keyhole, and a mixed-layer geometry governed not by cumulative diffusion, but by instantaneous flow disturbances around the keyhole front.

Chapter 3 extended the analysis to a three-material system by incorporating nickel-alloy filler wire feeding. The CFD model was expanded to simulate droplet melting, detachment, impact, and subsequent dispersion inside the molten pool. The results

demonstrated that droplet impingement temporarily alters keyhole stability, suppresses asymmetric convection, and modifies local thermal gradients, thereby producing complex transient mixing patterns. Upon solidification, nickel is shown to accumulate predominantly in the upper molten-pool region, forming a graded transition layer containing approximately 20–25% nickel. Such a distribution provides metallurgical benefits by improving compositional homogeneity between steel and cast iron, offering mechanistic insight into why Ni-based fillers effectively mitigate cracking in industrial differential-unit welds. The findings also show that while ternary mixing fluctuates significantly during welding, its final distribution is governed by keyhole-driven convection rather than long-range diffusion.

Chapter 4 introduced a hybrid heat-source modeling framework aimed at bridging fundamental CFD insights with practical engineering needs. By combining cylindrical and Goldak heat-source components and introducing an eccentricity parameter to represent wire-feed offset, the model achieved accurate and computationally efficient prediction of molten-zone geometry. Parametric studies demonstrated that even small wire offsets (±0.2 mm) significantly influence molten-pool asymmetry and weld shape, results that are consistent with experimental observations from production-scale differential units. This chapter highlights the potential of reduced-order heat-source models, informed by CFD physics, to enable rapid optimization of wire positioning and welding conditions in industrial applications where full CFD computation is impractical.

Overall, this dissertation provides a unified, mechanistic picture of thermal behavior, molten-pool dynamics, and material mixing in multi-material keyhole laser welding. Through rigorous computational modeling validated by experiments, the research clarifies how keyhole oscillations, Marangoni stresses, and dissimilar-material properties collectively shape weld morphology and interfacial structure. The developed frameworks—from high-fidelity CFD to fast predictive heat-source models—present a scalable pathway from scientific understanding toward industrial implementation. Future research should incorporate metal-vapor dynamics, shielding-

gas effects, microstructural evolution, and residual-stress formation, ultimately establishing an integrated multi-physics digital twin for dissimilar-material welding. This work thus lays a solid foundation for advancing both the science and engineering of laser-based joining in next-generation automotive and multi-material manufacturing systems.

References

[1] Rawicz AH. Theodore Harold Maiman and the invention of laser. Photonics, Devices, and Systems IV, vol. 7138, SPIE; 2008, p. 713802. https://doi.org/10.1117/12.817966.

[2] Wiench R, Fiegler-Rudol J, Zięba N, Misiołek M. The efficacy of carbon dioxide laser applications in tonsillectomy: systematic review. Lasers Med Sci 2025;40. https://doi.org/10.1007/s10103-025-04723-1.

[3] Dubey AK, Yadava V. Experimental study of Nd:YAG laser beam machining-An overview. Journal of Materials Processing Technology 2008;195:15–26. https://doi.org/10.1016/j.jmatprotec.2007.05.041.

[4] Syahida Mohd Nasir N, Khairul Azhar Abdul Razab M, Mamat S, Iqbal Ahmad M, Kelantan M. REVIEW ON WELDING RESIDUAL STRESS. vol. 11. 2016.

[5] Jauregui-Cervantez RE, Flores-Preciado JC, García-Gallegos JC, Soto-Tapiz MI. Bioengineering: An Alternative Technological Innovation for the Use of Dental Laser. EAS Journal of Dentistry and Oral Medicine 2023;5:180–4. https://doi.org/10.36349/easjdom.2023.v05i06.006.

[6] M. M. Quazi, M. Ishak, M. A. Fazal, A. Arslan, Saeed Rubaiee, M. H. Aiman, et al. A comprehensive assessment of laser welding of biomedical devices and implant materials: recent research, development and applications. Critical Reviews in Solid State and Materials Sciences 2020;46:109–51.

[7] Khan MS. Recent advances in mitigating fusion zone softening during laser welding of Al-Si coated 22MnB5 press-hardened steels. Materials Research Express 2023;10. https://doi.org/10.1088/2053-1591/acead5.

[8] Ceglarek D, Colledani M, Váncza J, Kim DY, Marine C, Kogel-Hollacher M, et al. Rapid deployment of remote laser welding processes in automotive

assembly systems. CIRP Annals - Manufacturing Technology 2015;64:389–94. https://doi.org/10.1016/j.cirp.2015.04.119.

[9] Hong KM, Shin YC. Prospects of laser welding technology in the automotive industry: A review. Journal of Materials Processing Technology 2017;245:46–69. https://doi.org/10.1016/j.jmatprotec.2017.02.008.

[10] Fourkas JT, Sugioka K, Lu Y. Editorial: Frontiers in lasers and applications. Frontiers in Nanotechnology 2024;6. https://doi.org/10.3389/fnano.2024.1371102.

[11] Sun T, Roy MJ, Strong D, Withers PJ, Prangnell PB. Comparison of residual stress distributions in conventional and stationary shoulder high-strength aluminum alloy friction stir welds. Journal of Materials Processing Technology 2017;242:92–100. https://doi.org/10.1016/j.jmatprotec.2016.11.015.

[12] Wang B, Zhu P, Cao Y, Zhou L, Xue P, Wu L. Effects of different friction stir welding processes on residual stress and deformation of Ti62A alloy joints. Journal of Materials Research and Technology 2023;26:6096–107. https://doi.org/10.1016/j.jmrt.2023.08.308.

[13] Geng P, Morimura M, Ma N, Huang W, Li W, Narasaki K, et al. Measurement and simulation of thermal-induced residual stresses within friction stir lapped Al/steel plate. Journal of Materials Processing Technology 2022;310. https://doi.org/10.1016/j.jmatprotec.2022.117760.

[14] Richter-Trummer V, Suzano E, Beltrão M, Roos A, dos Santos JF, de Castro PMST. Influence of the FSW clamping force on the final distortion and residual stress field. Materials Science and Engineering: A 2012;538:81–8. https://doi.org/10.1016/j.msea.2012.01.016.

[15] Shi QY, Silvanus J, Liu Y, Yan DY, Li HK. Experimental study on distortion of Al-6013 plate after friction stir welding. Science and Technology of Welding and Joining 2008;13:472–8. https://doi.org/10.1179/174329308X341924.

[16] Deepak JR, Anirudh RP, Saran Sundar S. Applications of lasers in industries and laser welding: A review. Materials Today: Proceedings 2023. https://doi.org/10.1016/j.matpr.2023.02.102.

[17] Ma B, Gao X, Huang Y, Gao PP, Zhang Y. A review of laser welding for aluminum and copper dissimilar metals. Optics and Laser Technology 2023;167. https://doi.org/10.1016/j.optlastec.2023.109721.

[18] Khan MS, Soleimani M, Midawi ARH, Aderibigbe I, Zhou YN, Biro E. A review on heat affected zone softening of dual-phase steels during laser welding. Journal of Manufacturing Processes 2023;102:663–84. https://doi.org/10.1016/j.jmapro.2023.07.059.

[19] Khan MS. Improving the multiscale morphological and mechanical properties of laser welded Al-Si coated 22MnB5 press-hardened steels. 2023.

[20] Xia H, Tao W, Li L, Tan C, Zhang K, Ma N. Effect of laser beam models on laser welding–brazing Al to steel. Optics and Laser Technology 2020;122. https://doi.org/10.1016/j.optlastec.2019.105845.

[21] Wu D, Li Y, Sun T, He G, Huo Q, Ma N, et al. High-speed synchrotron x-ray imaging and multi-physics modeling of molten pool and gas dynamics in laser additive manufacturing of a medium-entropy alloy. Welding in the World 2024;68:1417–25. https://doi.org/10.1007/s40194-023-01673-6.

[22] Khan MS, Ali S, Westerbaan D, Duley W, Biro E, Zhou YN. The effect of laser impingement angle on the optimization of melt pool geometry to improve process stability during high-speed laser welding of thin-gauge automotive

steels. Journal of Manufacturing Processes 2022;78:242–53. https://doi.org/10.1016/j.jmapro.2022.04.022.

[23] Li L, Xia H, Ma N, Pan B, Huang Y, Chang S. Comparison of the welding deformation of mismatch and normal butt joints produced by laser-arc hybrid welding. Journal of Manufacturing Processes 2018;34:678–87. https://doi.org/10.1016/j.jmapro.2018.07.015.

[24] Li L, Xia H, Tan C, Ma N. Effect of groove shape on laser welding-brazing Al to steel. Journal of Materials Processing Technology 2018;252:573–81. https://doi.org/10.1016/j.jmatprotec.2017.10.025.

[25] Ge Y, Yang A, Chang Z, Ma N, Wang Q. Enhancing reliability in laser powder bed fusion through substrate modification: microstructure, mechanical properties and residual stress. Optics and Laser Technology 2025;181. https://doi.org/10.1016/j.optlastec.2024.111612.

[26] Ge Y, Yang A, Chang Z, Ma N, Wang Q. Effect of substrate shape on residual stress in laser powder bed fusion forming parts. Materials Characterization 2025;221. https://doi.org/10.1016/j.matchar.2025.114765.

[27] Huang H, Wang J, Li L, Ma N. Prediction of laser welding induced deformation in thin sheets by efficient numerical modeling. Journal of Materials Processing Technology 2016;227:117–28. https://doi.org/10.1016/j.jmatprotec.2015.08.002.

[28] Li Y, Zhang X, Shi L, Wu C, Li S, Gao S. Double side friction stir Z shape butt lap welding of dissimilar titanium aluminum alloys. International Journal of Mechanical Sciences 2024;271. https://doi.org/10.1016/j.ijmecsci.2024.109135.

[29] Li Y, Xiao Y, Shi L, Chen L, Wu C, Mironov S, et al. Interfacial bonding mechanism in Al/Ti dissimilar friction stir welding. International Journal of Mechanical Sciences 2025;286. https://doi.org/10.1016/j.ijmecsci.2024.109903.

[30] Saludes Rodil S, Arnanz Gómez R, Bernárdez JM, Rodríguez F, Miguel LJ, Perán JR. Laser welding defects detection in automotive industry based on radiation and spectroscopical measurements. International Journal of Advanced Manufacturing Technology 2010;49:133–45. https://doi.org/10.1007/s00170-009-2395-y.

[31] Hong KM, Shin YC. Prospects of laser welding technology in the automotive industry: A review. Journal of Materials Processing Technology 2017;245:46–69. https://doi.org/10.1016/j.jmatprotec.2017.02.008.

[32] Fernandes FAO, Oliveira DF, Pereira AB. Optimal parameters for laser welding of advanced high-strength steels used in the automotive industry. Procedia Manufacturing, vol. 13, Elsevier B.V.; 2017, p. 219–26. https://doi.org/10.1016/j.promfg.2017.09.052.

[33] Huang S, Wang Y, Fan M, Huo X, Ma N, Lu F. The heterogeneous microstructure of laser welded joint and its effect on mechanical properties for dissimilar 9Cr steel and alloy 617. Journal of Materials Research and Technology 2023;26:1094–106. https://doi.org/10.1016/j.jmrt.2023.07.281.

[34] Sánchez-Amaya JM, Delgado T, González-Rovira L, Botana FJ. Laser welding of aluminum alloys 5083 and 6082 under conduction regime. Applied Surface Science 2009;255:9512–21. https://doi.org/10.1016/j.apsusc.2009.07.081.

[35] Cieslak M J, Fuerschbach P W. On the weldability, composition, and hardness of pulsed and continuous Nd: YAG laser welds in aluminum alloys 6061, 5456, and 5086. Metallurgical Transactions B, 1988, 19(2): 319-329.

[36] Wang Q, Ge Y, Chen J, Suzuki T, Sagisaka Y, Ma N. Unraveling Residual Stress Distribution Characteristics of 6061-T6 Aluminum Alloy Induced by Laser Shock Peening. Materials 2024;17. https://doi.org/10.3390/ma17143484.

[37] Zafar MQ, Wang J, Zhang Z, Wu C, Zhao H, Hussain G, et al. Thermomechanical Process Simulation and Experimental Verification for Laser Additive Manufacturing of Inconel®718. Materials 2023;16. https://doi.org/10.3390/ma16072595.

[38] Wang C, Xu N, Zhang G, Xu G, Xing F. Effect of heat treatment on microstructures and properties of vacuum laser welding Ti–6Al–4V titanium alloy. Journal of Materials Research and Technology 2024;30:6309–20. https://doi.org/10.1016/j.jmrt.2024.04.265.

[39] Akman E, Demir A, Canel T, Sinmazçelik T. Laser welding of Ti6Al4V titanium alloys. Journal of Materials Research and Technology 2009;209:3705–13. https://doi.org/10.1016/j.jmatprotec.2008.08.026.

[40] Paranthaman V, Dhinakaran V, Sai MS, Devaraju A. A systematic review of fatigue behavior of laser welding titanium alloys. Materials Today: Proceedings, vol. 39, Elsevier Ltd; 2020, p. 520–3. https://doi.org/10.1016/j.matpr.2020.08.249.

[41] Li Z, Gobbi S L. Laser welding for lightweight structures. Journal of Materials Processing Technology, 1997, 70(1-3): 137-144.

[42] Clayton A, Ribeiro N, Rafael &, Mota De Siqueira H, Milton &, Fernandes De Lima S, et al. Improvement weldability of dissimilar joints (Ti6Al4V/Al6013) for aerospace industry by laser beam welding n.d. https://doi.org/10.1007/s00170-021-07506-4/Published.

[43] Chen HC, Pinkerton AJ, Li L. Fiber laser welding of dissimilar alloys of Ti-6Al-4V and Inconel 718 for aerospace applications. International Journal of Advanced Manufacturing Technology 2011;52:977–87. https://doi.org/10.1007/s00170-010-2791-3.

[44] Liu Z, Li X, Pan L, Gao J, Zhang K. Effects of weld penetration modes on laser welding characteristics of a novel ultra-high strength steel for aerospace application. Journal of Manufacturing Processes 2023;90:111–24. https://doi.org/10.1016/j.jmapro.2023.02.003.

[45] Sun Z, Ion J C. Laser welding of dissimilar metal combinations. Journal of Materials Science, 1995, 30(17): 4205-4214.

[46] Yapp D, Blackman S A. Recent developments in high productivity pipeline welding. Journal of the Brazilian Society of Mechanical Sciences and Engineering, 2004, 26: 89-97.

[47] Masatomo T, Kenji S, Motomichi Y, et al. Hot-wire laser welding process using laser diode for large-diameter pipe with narrow gap joint. 溶接学会論文集, 2015, 33(2): 107s-110s.

[48] Feng J, Zhang P, Yan H, Shi H, Lu Q, Liu Z, et al. Application of Laser Welding in Electric Vehicle Battery Manufacturing: A Review. Coatings 2023;13. https://doi.org/10.3390/coatings13081313.

[49] Jung SH, Kim HJ. Application of laser welding to STS301L side structure of railway vehicles(I) - vertical incidence welding conditions for laser beam based on multiple regression analysis. Journal of Mechanical Science and Technology 2023;37:3087–94. https://doi.org/10.1007/s12206-023-0532-4.

[50] Farhadipour P, Omidi N, Barka N, Nadeau F, Idriss M, Ouafi A El. Systematic approach to improve overlap laser welding of AA5052-H32 with dissimilar thickness by evaluation of mechanical performance, undercut, and welding penetration. International Journal of Advanced Manufacturing Technology 2024;130:3387–99. https://doi.org/10.1007/s00170-023-12872-2.

[51] Wang P, Chen X, Pan Q, Madigan B, Long J. Laser welding dissimilar materials of aluminum to steel: an overview. International Journal of Advanced

Manufacturing Technology 2016;87:3081–90. https://doi.org/10.1007/s00170-016-8725-y.

[52] Rossini M, Spena PR, Cortese L, Matteis P, Firrao D. Investigation on dissimilar laser welding of advanced high strength steel sheets for the automotive industry. Materials Science and Engineering: A 2015;628:288–96. https://doi.org/10.1016/j.msea.2015.01.037.

[53] Yan S, Li Z, Song L, Zhang Y, Wei S. Research and development status of laser micro-welding of aluminum-copper dissimilar metals: A review. Optics and Lasers in Engineering 2023;161. https://doi.org/10.1016/j.optlaseng.2022.107312.

[54] Sadeghian A, Iqbal N. Blue laser welding of low thickness Ni-coated copper and mild steel for electric vehicle (EV) battery manufacturing. Optics and Laser Technology 2022;155. https://doi.org/10.1016/j.optlastec.2022.108415.

[55] Feng J, Zhang P, Yan H, Shi H, Lu Q, Liu Z, et al. Application of Laser Welding in Electric Vehicle Battery Manufacturing: A Review. Coatings 2023;13. https://doi.org/10.3390/coatings13081313.

[56] Ali S, Shin J. In-Depth Characterization of Laser-Welded Aluminum-and-Copper Dissimilar Joint for Electric Vehicle Battery Connections. Materials 2022;15. https://doi.org/10.3390/ma15217463.

[57] Saariluoma H, Piiroinen A, Unt A, Hakanen J, Rautava T, Salminen A. Overview of optical digital measuring challenges and technologies in laser welded components in EV battery module design and manufacturing. Batteries 2020;6:1–15. https://doi.org/10.3390/batteries6030047.

[58] Ghosh PS, Sen A, Chattopadhyaya S, Sharma S, Singh J, Li C, et al. Progressive developments and challenges in dissimilar laser welding of steel to

various other light alloys (Al/Ti/Mg): A comprehensive review. Heliyon 2022;8. https://doi.org/10.1016/j.heliyon.2022.e11710.

[59] Nielsen SE. High Power Laser Hybrid Welding - Challenges and Perspectives. Physics Procedia, vol. 78, Elsevier B.V.; 2015, p. 24–34. https://doi.org/10.1016/j.phpro.2015.11.014.

[60] Wang S, Wang W, Xu Y, Zhang X, Chen C, Geng P, et al. Effect of nanosecond pulsed laser parameters on texturing formation of metallic surface: Experiment and modelling. Journal of Materials Research and Technology 2023;26:7775–88. https://doi.org/10.1016/j.jmrt.2023.09.118.

[61] Hou X, Du D, Chang B, Ma N. Influence of scanning speed on microstructure and properties of laser cladded Fe-based amorphous coatings. Materials 2019;12. https://doi.org/10.3390/ma12081279.

[62] Xia H, Li L, Ma N, Tan C, Gong J. Influence of energy ratio on dual–spot laser welded–brazed Al/steel butt joint. Journal of Materials Processing Technology 2020;281. https://doi.org/10.1016/j.jmatprotec.2020.116624.

[63] Le-Quang T, Shevchik SA, Meylan B, Vakili-Farahani F, Olbinado MP, Rack A, et al. Why is in situ quality control of laser keyhole welding a real challenge? Procedia CIRP, vol. 74, Elsevier B.V.; 2018, p. 649–53. https://doi.org/10.1016/j.procir.2018.08.055.

[64] Huang YW, Gao XD, Gao PP, Ma B, Zhang YX. Laser welding monitoring techniques based on optical diagnosis and artificial intelligence: a review. Advances in Manufacturing 2025;13:337–61. https://doi.org/10.1007/s40436-024-00493-1.

[65] Fan X, Gao X, Liu G, et al. Research and prospect of welding monitoring technology based on machine vision. The International Journal of Advanced Manufacturing Technology, 2021, 115(11): 3365-3391.

[66] Hsu L-W, Salminen A. Laser welding monitoring with multisensory data fusion: A brief review. IOP Conference Series: Materials Science and Engineering 2023;1296:012014. https://doi.org/10.1088/1757-899x/1296/1/012014.

[67] Cai W, Wang JZ, Jiang P, Cao LC, Mi GY, Zhou Q. Application of sensing techniques and artificial intelligence-based methods to laser welding real-time monitoring: A critical review of recent literature. Journal of Manufacturing Systems 2020;57:1–18. https://doi.org/10.1016/j.jmsy.2020.07.021.

[68] Huang Y, Xu S, Yang L, Zhao S, liu Y, Shi Y. Defect detection during laser welding using electrical signals and high-speed photography. Journal of Materials Processing Technology 2019;271:394–403. https://doi.org/10.1016/j.jmatprotec.2019.04.022.

[69] Lei Z, Shen J, Wang Q, Chen Y. Real-time weld geometry prediction based on multi-information using neural network optimized by PCA and GA during thin-plate laser welding. Journal of Manufacturing Processes 2019;43:207–17. https://doi.org/10.1016/j.jmapro.2019.05.013.

[70] Zhang Y, You D, Gao X, Wang C, Li Y, Gao PP. Real-time monitoring of high-power disk laser welding statuses based on deep learning framework. Journal of Intelligent Manufacturing 2020;31:799–814. https://doi.org/10.1007/s10845-019-01477-w.

[71] Wang Z, Gao M. Numerical simulations of oscillating laser welding: A review. Journal of Manufacturing Processes 2024;119:744–57. https://doi.org/10.1016/j.jmapro.2024.04.001.

[72] Vázquez RG, Koch HM, Otto A. Multi-physical simulation of laser welding. Physics Procedia, vol. 56, Elsevier B.V.; 2014, p. 1334–42. https://doi.org/10.1016/j.phpro.2014.08.059.

[73] Perka AK, John M, Kuruveri UB, Menezes PL. Advanced High-Strength Steels for Automotive Applications: Arc and Laser Welding Process, Properties, and Challenges. Metals (Basel) 2022;12. https://doi.org/10.3390/met12061051.

[74] Svenungsson J, Choquet I, Kaplan AFH. Laser Welding Process - A Review of Keyhole Welding Modelling. Physics Procedia, vol. 78, Elsevier B.V.; 2015, p. 182–91. https://doi.org/10.1016/j.phpro.2015.11.042.

[75] Zhang R, Nishimoto D, Ma N, Narasaki K, Wang Q, Suga T, et al. Asymmetric molten zone and hybrid heat source modeling in laser welding carbon steel and cast iron with nickel alloy wires. Journal of Manufacturing Processes 2025;142:177–90. https://doi.org/10.1016/j.jmapro.2025.03.074.

[76] Baqer YM, Ramesh S, Yusof F, Manladan SM. Challenges and advances in laser welding of dissimilar light alloys: Al/Mg, Al/Ti, and Mg/Ti alloys. International Journal of Advanced Manufacturing Technology 2018;95:4353–69. https://doi.org/10.1007/s00170-017-1565-6.

[77] Kaushik P, Dwivedi DK. Al-steel dissimilar joining: Challenges and opportunities. Mater Today Proc, vol. 62, Elsevier Ltd; 2022, p. 6884–99. https://doi.org/10.1016/j.matpr.2022.05.211.

[78] Ma N, Li L, Huang H, Chang S, Murakawa H. Residual stresses in laser-arc hybrid welded butt-joint with different energy ratios. Journal of Materials Processing Technology 2015;220:36–45. https://doi.org/10.1016/j.jmatprotec.2014.09.024.

[79] Duan Y, Zhao Y, Yan K, Ma S, Song S. Study on the Droplet Transition Models in Laser Welding with Filler Wire. Transactions of the Indian Institute of Metals 2020;73:1043–51. https://doi.org/10.1007/s12666-020-01930-y.

[80] Satyanarayana G, Narayana KL, Nageswara Rao B. Incorporation of Taguchi approach with CFD simulations on laser welding of spacer grid fuel rod

assembly. Materials Science and Engineering: B 2021;269. https://doi.org/10.1016/j.mseb.2021.115182.

[81] Chianese G, Hayat Q, Jabar S, Franciosa P, Ceglarek D, Patalano S. A multi-physics CFD study to investigate the impact of laser beam shaping on metal mixing and molten pool dynamics during laser welding of copper to steel for battery terminal-to-casing connections. Journal of Materials Processing Technology 2023;322. https://doi.org/10.1016/j.jmatprotec.2023.118202.

[82] Haran F M, Hand D P, Peters C, et al. Real-time focus control in laser welding. Measurement Science and Technology, 1996, 7(8): 1095.

[83] Masinelli G, Le-Quang T, Zanoli S, Wasmer K, Shevchik SA. Adaptive Laser Welding Control: A Reinforcement Learning Approach. IEEE Access 2020;8:103803–14. https://doi.org/10.1109/ACCESS.2020.2998052.

[84] Huang W, Kovacevic R. Development of a real-time laser-based machine vision system to monitor and control welding processes. International Journal of Advanced Manufacturing Technology 2012;63:235–48. https://doi.org/10.1007/s00170-012-3902-0.

[85] Liu W, Ma J, Liu S, Kovacevic R. Experimental and numerical investigation of laser hot wire welding. International Journal of Advanced Manufacturing Technology 2015;78:1485–99. https://doi.org/10.1007/s00170-014-6756-9.

[86] Jiménez-Xamán M, Hernández-Hernández M, Tariq R, Landa-Damas S, Rodríguez-Vázquez M, Aranda-Arizmendi A, et al. Numerical simulations and mathematical models in laser welding: a review based on physics and heat source models. Frontiers in Mechanical Engineering 2024;10. https://doi.org/10.3389/fmech.2024.1325623.

[87] Hu S, Li F, Zuo P. Numerical Simulation of Laser Transmission Welding—A Review on Temperature Field, Stress Field, Melt Flow Field, and Thermal

Degradation. Polymers (Basel) 2023;15. https://doi.org/10.3390/polym15092125.

[88] Dal M, Fabbro R. [INVITED] An overview of the state of art in laser welding simulation. Optics and Laser Technology 2016;78:2–14. https://doi.org/10.1016/j.optlastec.2015.09.015.

[89] Tsirkas SA. Numerical simulation of the laser welding process for the prediction of temperature distribution on welded aluminum aircraft components. Optics and Laser Technology 2018;100:45–56. https://doi.org/10.1016/j.optlastec.2017.09.046.

[90] Chandelkar V, Pradhan SK. Numerical simulation of temperature distribution and experimentation in laser beam welding of SS317L alloy. Mater Today Proc, vol. 27, Elsevier Ltd; 2019, p. 2758–62. https://doi.org/10.1016/j.matpr.2019.11.331.

[91] GuoMing H, Jian Z, JianQang L. Dynamic simulation of the temperature field of stainless steel laser welding. Materials and Design 2007;28:240–5. https://doi.org/10.1016/j.matdes.2005.06.006.

[92] Ninshu Ma, Dean Deng, Naoki Osawa, Sherif Rashed, Hidekazu Murakawa, Yukio Ueda,“Welding Deformation and Residual Stress Prevention”, Butterworth-Heinemann, Elsevier, 2nd Edition, July 1, 2022, eBook ISBN: 978-0-323-886-505, Paperback ISBN : 978-0-323-88665-9. https://www.elsevier.com/books/welding-deformation-and-residual-stress-prevention/ma/978-0-323-88665-9

[93] He X. Finite element analysis of laser welding: A state of art review. Materials and Manufacturing Processes 2012;27:1354–65. https://doi.org/10.1080/10426914.2012.709345.

[94] Casalino G, Mortello M, Peyre P. FEM Analysis of Fiber Laser Welding of Titanium and Aluminum. Procedia CIRP, vol. 41, Elsevier B.V.; 2016, p. 992–7. https://doi.org/10.1016/j.procir.2016.01.030.

[95] Anca A, Cardona A, Risso J, Fachinotti VD. Finite element modeling of welding processes. Applied Mathematical Modelling 2011;35:688–707. https://doi.org/10.1016/j.apm.2010.07.026.

[96] Behúlová M, Babalová E. Heat source models for numerical simulation of laser welding processes - A short review. Journal of Physics: Conference Series, vol. 2712, Institute of Physics; 2024. https://doi.org/10.1088/1742-6596/2712/1/012018.

[97] Jiménez-Xamán M, Hernández-Hernández M, Tariq R, Landa-Damas S, Rodríguez-Vázquez M, Aranda-Arizmendi A, et al. Numerical simulations and mathematical models in laser welding: a review based on physics and heat source models. Frontiers in Mechanical Engineering 2024;10. https://doi.org/10.3389/fmech.2024.1325623.

[98] Chang WS, Na SJ. A study on the prediction of the laser weld shape with varying heat source equations and the thermal distortion of a small structure in micro-joining. Journal of Materials Processing Technology 2002;120, Issues 1-3:208–14. https://doi.org/https://doi.org/10.1016/S0924-0136(01)00716-6.

[99] Liang G, Qin G, Cao P, Wang H. Evolutions of temperature field and stress field in narrow gap oscillating laser welding process based on equivalent heat source. Journal of Materials Research and Technology 2024;28:154–67. https://doi.org/10.1016/j.jmrt.2023.11.262.

[100] Paul A, Debroy T. Free surface flow and heat transfer in conduction mode laser welding. Metallurgical Transactions B, 1988, 19(6): 851-858.

[101] Sahoo P, Debroy T, McNallan M J. Surface tension of binary metal—surface active solute systems under conditions relevant to welding metallurgy. Metallurgical transactions B, 1988, 19(3): 483-491.

[102] Zhou X, Zhang H, Wang G, Bai X. Three-dimensional numerical simulation of arc and metal transport in arc welding based additive manufacturing. International Journal of Heat and Mass Transfer 2016;103:521–37. https://doi.org/10.1016/j.ijheatmasstransfer.2016.06.084.

[103] Cho M H, Lim Y C, Farson D F. Simulation of weld pool dynamics in the stationary pulsed gas metal arc welding process and final weld shape. Welding Journal-New York-, 2006, 85(12): 271.

[104] Kazemi K, Goldak JA. Numerical simulation of laser full penetration welding. Computational Materials Science 2009;44:841–9. https://doi.org/10.1016/j.commatsci.2008.01.002.

[105] Lin R, Wang H ping, Lu F, Solomon J, Carlson BE. Numerical study of keyhole dynamics and keyhole-induced porosity formation in remote laser welding of Al alloys. International Journal of Heat and Mass Transfer 2017;108:244–56. https://doi.org/10.1016/j.ijheatmasstransfer.2016.12.019.

[106] Huang S, Xu L, Lou M, Chen H, Zhang K, Li Y. Keyhole-induced pore formation mechanism in laser-MIG hybrid welding of aluminum alloy based on experiment and multiphase numerical model. Journal of Materials Processing Technology 2023;314. https://doi.org/10.1016/j.jmatprotec.2023.117903.

[107] Eriksson I, Gren P, Powell J, Kaplan AF. New high-speed photography technique for observation of fluid flow in laser welding. Optical Engineering 2010;49:1. https://doi.org/10.1117/1.3502567.

[108] Li P, Fan Y, Zhang C, Zhu Z, Tian W, Liu A. Research on Heat Source Model and Weld Profile for Fiber Laser Welding of A304 Stainless Steel Thin Sheet. Advances in Materials Science and Engineering 2018;2018. https://doi.org/10.1155/2018/5895027.

[109] Huang W, Wang H, Rinker T, Tan W. Investigation of metal mixing in laser keyhole welding of dissimilar metals. Materials and Design 2020;195. https://doi.org/10.1016/j.matdes.2020.109056.

[110] Ai Y, Dong G, Yuan P, Liu X, Yan Y. The influence of keyhole dynamic behaviors on the asymmetry characteristics of weld during dissimilar materials laser keyhole welding by experimental and numerical simulation methods. International Journal of Thermal Sciences 2023;190. https://doi.org/10.1016/j.ijthermalsci.2023.108289.

[111] Shehryar Khan M, Shahabad SI, Yavuz M, Duley WW, Biro E, Zhou Y. Numerical modelling and experimental validation of the effect of laser beam defocusing on process optimization during fiber laser welding of automotive press-hardened steels. Journal of Manufacturing Processes 2021;67:535–44. https://doi.org/10.1016/j.jmapro.2021.05.006.

[112] Wu D, Ishida K, Tashiro S, Nomura K, Hua X, Ma N, et al. Dynamic keyhole behaviors and element mixing in paraxial hybrid plasma-MIG welding with a gap. International Journal of Heat and Mass Transfer 2023;200. https://doi.org/10.1016/j.ijheatmasstransfer.2022.123551.

[113] Ke W, Bu X, Oliveira JP, Xu WG, Wang Z, Zeng Z. Modeling and numerical study of keyhole-induced porosity formation in laser beam oscillating welding of 5A06 aluminum alloy. Optics and Laser Technology 2021;133. https://doi.org/10.1016/j.optlastec.2020.106540.

[114] Brown O L I. The clausius-clapeyron equation. Journal of Chemical Education, 1951, 28(8): 428.

[115] Tong LG, Gu JC, Yin SW, Wang L, Bai SW. Impacts of torch moving on phase change and fluid flow in weld pool of SMAW. International Journal of Heat and Mass Transfer 2016;100:949–57. https://doi.org/10.1016/j.ijheatmasstransfer.2016.04.032.

[116] Tong LG, Gu JC, Wang L, Yin SW. Influences of deposited metal material parameters on weld pool geometry during shield metal arc welding. International Journal of Heat and Mass Transfer 2015;90:968–78. https://doi.org/10.1016/j.ijheatmasstransfer.2015.06.051.

[117] Fan H G, Tsai H L, Na S J. Heat transfer and fluid flow in a partially or fully penetrated weld pool in gas tungsten arc welding. International Journal of Heat and Mass Transfer, 2001, 44(2): 417-428.

[118] Ma N. An accelerated explicit method with GPU parallel computing for thermal stress and welding deformation of large structure models. International Journal of Advanced Manufacturing Technology 2016;87:2195–211. https://doi.org/10.1007/s00170-016-8542-3.

[119] Feng Z, Ma N, Li W, Narasaki K, Lu F. Efficient analysis of welding thermal conduction using the Newton–Raphson method, implicit method, and their combination. International Journal of Advanced Manufacturing Technology 2020;111:1929–40. https://doi.org/10.1007/s00170-020-06233-6.

Achievements

Publications related to doctor thesis

[1] **Renzhi Zhang**, Daichi Nishimoto, Ninshu Ma, Kunio Narasaki, Qian Wang, Tetsuo Suga, Shota Tsuda, Takayuki Tabuchi, Syuichi Shimada, Asymmetric molten zone and hybrid heat source modeling in laser welding carbon steel and cast iron with nickel alloy wires, Journal of Manufacturing Processes, Volume 142, 2025, Pages 177-190, ISSN 1526-6125, https://doi.org/10.1016/j.jmapro.2025.03.074.

[2] **Renzhi Zhang**, Daichi Nishimoto, Ninshu Ma, Fenggui Lu, Tetsuo Suga, Takayuki Tabuchi, Syuichi Shimada, Numerical modelling of laser welding pool thermal-dynamics and dissimilar materials mixing of cast iron, carbon-steel and nickel-alloy wire for weld crack prevention, Journal of Manufacturing Processes, Volume 156, Part B, 2025, Pages 398-410, ISSN 1526-6125, https://doi.org/10.1016/j.jmapro.2025.11.054.

[3] **張人之**, 王倩, 楢崎邦男, 菅哲男, 麻寧緒, 西本大地, 津田翔太, 田淵隆行, 島田秀一, 鈴木健史. (2023). Ni 合金ワイヤを用いた炭素鋼と鋳鉄のレーザ溶接温度場解析モデリング. In *溶接学会全国大会講演概要 2023 年度秋季全国大会* (pp. 58-59). 一般社団法人 溶接学会.

Other publications

[1] Ruwei Geng, Ninshu Ma, Daichi Nishimoto, **Renzhi Zhang**, Fenggui Lu, Zhongwu Li, Microstructure, element distribution and interfacial properties of laser welded iron–nickel–steel dissimilar joints, Journal of Materials Research and Technology, Volume 37, 2025, Pages 2463-2473, ISSN 2238-7854, https://doi.org/10.1016/j.jmrt.2025.06.152.

[2] 西本大地, 津田翔太, 田淵隆行, 島田秀一, 鈴木健史, **張人之**, 王 倩, 楢崎邦男, 麻寧緒, 菅哲男. (2023). Ni 合金ワイヤを用いた鋳鉄と炭素鋼のレーザ溶接部における Ni 分布状況の調査. In *溶接学会全国大会講演概要 2023 年度秋季全国大会* (pp. 60-61). 一般社団法人 溶接学会. https://doi.org/10.14920/jwstaikai.2023f.0_60

[3] 西本大地, **張人之**, 石川毅彦, 麻寧緒, & 島田秀一. (2025). 融体の鋳鉄・鋼材・Ni 合金における密度・表面張力・粘性係数の高精度測定. In *溶接学会全国大会講演概要 2025 年度春季全国大会* (pp. 70-71). 一般社団法人 溶接学会. https://doi.org/10.14920/jwstaikai.2025s.0_70

Acknowledgements

First and foremost, I would like to express my deepest appreciation to my supervisor, Prof. Ninshu Ma. I am sincerely grateful for his guidance during the early stage of my research and for his continuous support throughout my doctoral studies. His instruction and mentoring helped me establish a clear research direction and make steady progress, while his insightful advice guided me through each critical stage and research challenge. Beyond academic development, his mentorship also strengthened my resilience and perseverance in facing difficulties.

I would also like to express my sincere gratitude to Professor Qian Wang for her guidance and support during my first experience of academic paper writing. Her constructive advice and patient instruction helped me build a clear framework for academic writing, which laid an important foundation for my subsequent studies.

My sincere thanks also to all the staffs at the Joining and Welding Research Institute (JWRI) of the University of Osaka for their support in my research activities. Particularly, I am grateful to the secretaries of Ma Lab: Mrs. Kikuchi, Mrs. Akaji, Mrs. Nakahara, and Mrs. Hirose for their kind assistance and support throughout my study and daily life in Ma Lab.

I am also thankful to researchers in Ma Lab: Dr. Kunio Narasaki, Prof. Sendong Ren, Prof. Peihao Geng, Prof. Ruwei Geng, Dr. Song Wu, Dr. Fujun Cao, Prof. Yaqiong Ge, Prof. Jingjing Li, Dr. Weihao Li, Dr. Wenjia Huang, Dr. Yifan Gao, Dr. Mingzhe Fan, Dr. Suyu Wang, Dr. Mohan He, Dr. Tianxing Chang, Dr. Liangyu Fei, Dr. Kai Song, Mr. Yang Li, Mr. Jingjia Chen, Ms. Yuzhao Jiang, Ms. Feifei Xie, Mr. Congcong Ren, Ms. Jiamin Wang, Mr. Tianxing Chang, Mr. Di Yang, Mr. Chaimano, and Mr. Nour, whose companionship and support made my time in the laboratory both productive and enjoyable.

I would like to thank JATCO Ltd. for their trust and providing the opportunity for collaborative research that supported this doctoral study. I am particularly grateful to Mr. Takayuki Tabuchi, Mr. Syuichi Shimada, Mr. Daichi Nishimoto, and other

engineers for their continuous support throughout the collaboration. I am also thankful to Prof. Tetsuo Suga for his assistance in facilitating this collaboration.

Finally, I would like to express my heartfelt gratitude to my family. I am deeply thankful to my parents, Mr. Zhong Zhang and Mrs. Jing Liu, for their lifelong support and encouragement, which have always been my strongest foundation. I am especially grateful to my beloved wife Mrs. Yuheng Qiu for her constant care and dedication to our family. To my dear daughter, Xiyue Zhang, you have brought great joy to my life. I also warmly welcome our second child and wish you a healthy and happy future with our family.

I sincerely thank all mentioned above for their valuable support. Without their contributions and encouragement, this dissertation could not have been completed.

In addition, this work was partially supported by “Osaka University promotion program of cutting-edge multilateral international collaboration related to joining and materials science” and “JWRI International Joint Research Collaborators (JIJReC) program”.